Mathematical Analysis of Receptor-Mediated Immune Cell Death in Innate Antiviral Immunity

Von der Fakultät für Lebenswissenschaften

der Technische Universität Carolo-Wilhelmina zu Braunschweig

zur Erlangung des Grades eines

Doktor des Naturwissenschaften

(Dr. rer. nat.)

genehmigte

D i s s e r t a t i o n

von Jesus David Badillo Herrera
aus Mompos, Kolumbien

1. Referant: Prof. Dr. Michael Meyer-Hermann
2. Referant: Prof. Dr. Martin Korte
eingereicht am: 14.10.2020
mündliche Prüfung (Disputation) am: 25.01.2021

Druckjahr 2021

Vorveröffentlichungen der Dissertation

Teilergebnisse aus dieser Arbeit wurden mit Genehmigung der Fakultät für Lebenswissenschaften, vertreten durch den Mentor der Arbeit, in folgenden Beiträgen vorab veröffentlicht:

Tagungsbeiträge:

- **Badillo Herrera, J.D.**; (2019) Mathematical modeling of Cell death modulation upon immune response during IAV infection. (Talk) 10th Annual Retreat, HZI Graduate School, Haus der Wissenschaft, Braunschweig.

Posterbeiträge:

- **Badillo Herrera, J.D.**; (2018) Mathematical analysis of receptor-mediated immune cell death in antiviral immunity. (Poster) 11th International PhD Symposium, HZI Braunschweig.
- **Badillo Herrera, J.D.**; (2017) Mathematical Analysis of Receptor-Mediated Immune Cell Death in Antiviral Immunity. (Poster) 10th International PhD Symposium, HZI Braunschweig.

Abstract

Apoptosis is a series of complex biochemical processes of programmed cell death which occurs in multicellular organisms. This mechanism must be highly regulated and controlled; otherwise, harmful illness such as cancer and autoimmune diseases may occur. Apoptosis is a key mechanism during a typical viral immune response. In the course of an infection, this mechanism eliminates infected cells and by that, limits the resources for viral replication. Recently, regulation of the death receptor pathway by cFLIP, a key regulator of signaling complexes downstream of death receptors, was targeted experimentally to study the role of apoptosis in influenza A virus (IAV) infection. By increasing the expression level of cFLIP in transgenic mice, a higher accumulation of Natural Killer (NK) cells and a higher viral load in comparison to wild type(WT) mice were observed. However, the viral load was similar in both mice after 10 days. Infection and functional impairment of NK cells was assumed to be responsible for the observed results. In order to validate this hypothesis, a mathematical model was used to quantify the role of apoptosis mediated cell death in NK cells during the viral clearance. The model contains variables and parameters that represent population and interactions between healthy and infected epithelial cells, influenza A virions, healthy and infected NK cells. Several simplifications were made in order to better estimate the critical parameters of the model. Simulation results showed that infection of NK cells with a longer lifespan alone cannot explain the observed high viral load. However, by increasing the viral production of infected NK cells, the viral load data was fitted. The lack of caspase 3, due to the over-expression of cFLIP, may contribute to higher viral production in NK cells. Furthermore, a shorter lifespan of healthy NK cells was predicted, which may be related to biological exhaustion due to higher infection level. The posteriors and the correlation analysis of the parameters showed that parameters associated with lifespan and the viral production of infected NK cells are linearly correlated.

Zusammenfassung

Die Apoptose ist ein komplexer biochemischer Prozess des programmierten Zelltod, die in mehrzelligen Organismen auftritt. Dieser Mechanismus muss eng kontrolliert werden, sonst können schädliche Krankheiten auftreten, so wie z.B. Krebs und Autoimmunerkrankungen. Während einer typischen viralen Immunantwort, werden infizierte Zellen durch Apoptose eliminiert, so dass die Ressourcen für die Virusreplikation begrenzt werden. cFLIP ist ein Inhibitor der Todesrezeptor-gesteuerten Apoptose. Die Regulation des extrinsischen Signalwegs durch cFLIP wurde erforscht um die Rolle der Apoptose während Influenza A Infektionen zu untersuchen. Hierfür wurden transgene Mäuse, die cFLIP in allen hämatopowerten Zellen exprimieren, mit dem Influenza A-Virus infiziert. Diese transgenen Mäuse haben mehr natürliche Killerzellen (NK) und höhere Viruslast aufgewiesen. Die Viruslast nach 10 Tagen waren ähnlich bei transgenen und Wildtyp (WT) Mäusen. Tafrishi argumentierte, dass die infizierten NK-Zellen und ihre Funktionsstörung verantwortlich für die Ergebnissen sind. Hierin wurde ein mathematisches Modell verwendet, um diese Hypothese zu validieren und die Rolle der Apoptose in NK Zellen durch Influenza A-Infektionen zu quantifizieren. Die Modellvariablen und Parameter darstellen die Population und Wechselwirkungen beidem Influenza A-Virus, gesunden und infizierten Epithelzellen und gesunden und infizierten NK-Zellen. Die Simulationsergebnissen demonstrieren, dass infizierte NK-Zellen, die eine längere Lebensdauer haben, nicht der Grund für die erhöhte Viruslast sind. Stattdessen ist eine höhere Virusproduktion von der infizierten NK-Zellen notwendig, um die Viruslast Daten anzupassen. Deshalb kann das Fehlen von Caspase 3, aufgrund der Überexpressionvon cFLIP, zu einer höheren Virusproduktion in den NK-Zellen beitragen. Darüber hinaus hat die Datenanpassung eine kürzere Lebensdauer der gesunden NK-Zellen vorhergesagt, aufgrund der biologischen Erschöpfung. Korrelationsanalysen der Parameter zeigten, dass die Lebensdauer und die Virusproduktion der infizierten NK-Zellen linear korreliert sind.

Contents

List of Tables

List of Figures

1 Introduction

Apoptosis is a form of programmed cell death mainly characterized by cell size reduction and fragmentation of the cytoskeleton, forming vesicles –apoptotic bodies– which are phagocytosed afterwards [114]. Two different mechanisms can initiate the apoptotic process in a cell, the intrinsic or mitochondrial-initiated pathway, and the extrinsic or death receptor-mediated pathway [57]. In the intrinsic pathway, different stressors such as DNA damage, free radicals, toxins and UV radiation, send a signal to the cell to begin the process of apoptosis. On the other hand, the extrinsic pathway is activated by stimulus from death receptors on the cell surface, such as CD95 ligand [87, 107]. Regardless of the pathway, the signals lead to the activation of upstream initiator caspase (caspase 8 or 9), which in turn stimulates the effector caspase (caspase 3, 6 or 7). The latter cleaves the cell structure by degrading proteins [127].

During a typical immune response, apoptosis plays a critical role in controlling infections by limiting resources available for pathogen replication [66, 46]. In this case, apoptosis is mostly induced by immune cells via the extrinsic pathway. Moreover, the apoptosis mechanism is crucial to regulate immune responses during and after an infection, as it maintains the number of immune cells at reasonable levels, preventing autoimmune responses.

Apoptosis is deeply related to different aspects of influenza A virus (IAV) infection. Several researches have reported IAV usage of apoptosis resources to facilitate its replication. During the first stage of the infection, IAV inhibits apoptosis by up-regulating the anti-apoptotic protein PI3 K-AKT, in order to gain time to replicate. Afterwards, the virus induces apoptosis by up-regulating the pro-apoptotic p53 pathway, allowing a more efficient release of virions [130, 127, 124].

In 2013, Telieps et al. [115] investigated the role of apoptosis on immune cells during the clearance of infections. For this purpose, transgenic mice (vavFLIP$_R$ mice), whose CD8$^+$ T cells (CTLs) over-express the apoptosis inhibitor protein c-FLIP$_R$, were challenged with Listeria monocytogene [115, 100]. vavFLIP$_R$ mice showed less liver necrosis and better bacterial clearance compared with infected wild-type mice (WT mice), proving that apoptosis resistant CTLs guarantee a more efficient immune response against Listeria infection [115].

Tafrishi [107] investigated the role of apoptosis upon immune cells during an IAV infection by challenging vavFLIP$_R$ mice, –whose Natural killer (NK) cells over express c-FLIP$_R$ – with IAV. Interesting and counterintuitive results were obtained in this

research. First of all, a higher accumulation of NK cells was observed in vavFLIP$_R$ at the peak of the infection. Secondly, despite the higher number of NK cells, vavFLIP$_R$ presented a higher viral load than WT mice at the peak of infection. Thirdly, *in vitro* experiments demonstrated that IAV can directly infect NK cells and effectively reproduce within them. This IAV strategy aims to impair NK cells functionality. Finally, NK cells of both vavFLIP$_R$ and WT mice were depleted prior and during the IAV infection, which results in the disappearance of differences in the viral load between both types of mice; such results may indicate that NK cell dynamics is responsible for the changes in the viral load observed in vavFLIP$_R$ mice.

As IAV infection remains an ongoing worldwide threat for public health [101, 117, 91], understanding the relationship among apoptosis, innate immune response (NK cells) and IAV is crucial, so that new strategies can be developed to prevent and treat influenza infection.

In order to further understand the mechanisms behind the experimental results obtained by Tafrishi [107], a mathematical model based on a system of ordinary differential equations (ODEs) is proposed. The model contains variables and parameters that represent populations and interactions between healthy and infected epithelial cells, virions and NK cells. The estimation of the critical parameters of the model allows the evaluation of different hypotheses. By these assessments, the questions of interest such as the role of NK cells during an IAV infection, the reason behind the increase in the viral load and the role of the apoptosis on immune cells during viral infection, can be answered.

In chapter 2, an introduction of the programmed cell death via apoptosis along with the main elements of the immune response during an IAV infection is presented. Furthermore, in chapter 3, the main mathematical concepts used for the development of this work, such as dynamical modelling, statistical modelling and parameter estimation methods, are introduced. Finally, a summary of the state-of-art in the mathematical model of IAV infection is presented. In chapter 4, the experimental data obtained by Tafrishi [107] is introduced. Information regarding the kinetics of viral load, NK cells, proinflammatory cytokines and *in vitro* experiments regarding IAV binding to NK cells is presented. This data was critical for the development of the model and different hypotheses proposed afterwards.

The IAV infection model is presented in chapter 5. Herein, a comprehensive explanation of the assumptions and the structure of the model is provided. Additionally, a detailed description of the numerical methods and statistical model used for the parameter estimation is also introduced. At the end of this chapter, a simple example is presented in order to demonstrate the capabilities of the parameter estimation algorithm. In the subsequent chapter, the fitting to WT mice data is introduced. Description of the initially assumed probability distributions of the parameters and further simplifications in the parameter space are presented herein as well. After-

wards, the probability distributions of the parameters after the data fitting are provided. Moreover, the effect of the adaptive immune response is presented at the end of this chapter, in order to analyse the prediction capabilities of the model.

In chapter 7, different hypotheses are proposed in order to explain the vavFLIP$_R$ phenomenon. A comparison of such hypotheses is also presented. Finally, in the last chapter, the results of this work will be summarized and an outlook to further research will be provided.

2 Biological framework

In this chapter, a theoretical background about the main biological concepts used in this work is provided. The concept of apoptosis as well as the main components of the immune response during the IAV infection are introduced.

2.1 Cell death

Cell death is a biochemical process by which a cell ceases to perform its functions. This may occur as a consequence of old cells being replaced by new ones, internal damage or pathogens. This process is crucial in tissues homeostasis, embryonic development and elimination of undesirable cells [37, 107]. Hitherto, five main forms of cell death have been identified: apoptosis, necroptosis, pyroptosis, necrosis and autophagy. This classification is based on the mode of cell death, i.e. programmed or accidental, the initiators and the production of inflammatory cytokines [67].

Apoptosis is mainly characterized by cell size reduction and the fragmentation of the cytoskeleton, forming vesicles –apoptotic bodies– which are phagocytosed afterwards [114]. During the necrosis process, on the other hand, the cytoplasm and organelles are swelled and the plasma membrane breaks, releasing the intracellular components. In contrast, necrosis is mainly characterized by an enormous oxidative stress [46]. Recent experiments have provided evidence of a regulated form of necrosis, at a molecular level. In order to distinguish between the deregulated and regulated necrosis, the latter one is called necroptosis [85, 36].

Another important form of programmed cell death is pyroptosis. This biological event can occur due to different pathological stimuli – most likely as a response to microbial infections – , and is characterized by a highly inflammatory form. Cells under pyroptosis undergo a rapid membrane rupture, releasing proinflammatory intracellular contents [13]. Autophagy is a self-digestive process, generally triggered by nutrient

deprivation. In this process, vacuoles are formed and subsequently phagocytosed in a specific sequence [103]. All this process must be highly regulated. Otherwise the homeostasis between cellular proliferation and cell death may be broken, leading to malignant diseases [79].

2.2 Apoptosis

Apoptosis is a series of complex biochemical processes of programmed cell death which occurs in multicellular organisms. This mechanism must be highly regulated and controlled; otherwise, harmful illnesses such as cancer and autoimmune diseases may occur [34, 107]. Apoptosis plays a key role in the elimination of undesirable cells during development and maintenance of tissues as well as in the depletion of immune cells to maintain immune homeostasis [37]. Furthermore, during immune responses against viral and bacterial infections, apoptosis restricts the resources available for pathogen replication by inducing death to infected cells [46].

Cell death via apoptosis can be initiated by two different paths, the intrinsic or mitochondrial-initiated pathway and the extrinsic or death receptor-mediated pathway [57]. In both cases, different signals activate enzymes (cysteine proteases or caspases), which in turn, degrade proteins without distinction until the cell dies. The intrinsic pathway can be initiated by different stressors such as DNA damage, free radicals, toxins, UV radiation etc. In contrast, the extrinsic pathway is initiated by signals from the death receptors on the cell surfaces, such as CD95 ligand [87, 107]. Once stimulated, CD95 recruits pro-apoptotic factors, contributing to the formation of the multiprotein complex, death-inducing signaling complex (DISC) [31]. This protein DISC activates the initiator (caspase 8 or 9), which in turn, activate executioner caspases (caspase 3, 6 or 7), resulting then in apoptosis [2, 107]. CTLs and NK cells use CD95L as a mechanism to eliminate infected cells [93]. Nevertheless, during the immune response, apoptosis is regulated by cellular FLIP proteins (c-FLIP) directly at the DISC of death receptors, by interfering with initiator caspases activation [100, 115, 107]. Recent studies have presented evidence, suggesting that certain viruses, such as IAV, may take advantage of the apoptosis mechanism in order to improve their replication [127, 107].

2.3 Influenza virus

Influenza viruses are part of the orthomyxoviridae family and are characterized by a negative-sense single-stranded segmented RNA genome. Influenza A, B and C viruses distinguish themselves from each other by the antigenic differences in nuclear and matrix proteins. Additionally, a further classification of IAV can be carried out by analyzing the surface glycoproteins, hemagglutinin (HA) and neuraminidase (NA) [98, 120, 107].

The respiratory diseases caused by influenza virus are an ongoing worldwide challenge for public health. Seasonal epidemic outbreaks generated by influenza virus provoke as many as 5 millions severe cases and $500,000$ deaths per year [101, 117, 91, 55]. Reported outbreaks such as Asiatic Flu (H2N8), Spanish Flu (H1N1), Asian Flu

(H2N2), Hong Kong Flu (H3N2) and swine Flu (H1N1) have uncovered significant high mortality rate from this type of virus. Although all age groups can get infected by influenza, toddlers, pregnant women, seniors and immuno-compromised individuals are more susceptible to complications [17, 84, 113, 107]. Furthermore, this pandemic infection can produce an impact on the economy due to hospitalization and health complication expenses [94, 69].

The continuous antigenic variation of influenza virus is the main reason for which this pathogen continues to be a threat to public health. By this mechanism, the virus is able to alter its surface proteins, evading the host immune response. The antigenic variation of IAV occurs by two mechanisms, antigenic shift and antigenic drift [25, 72, 19]. Further changes can happen due to different host factors. Therefore, the immunity of a host may be compromised, increasing mortality rate even among healthy young adults. Moreover, these changes require continuous modifications in current vaccination and therapy strategies.

The main target of influenza virus is the epithelial cells, located in the respiratory tract. In the case of uncomplicated influenza infection, only the upper respiratory tract and the upper division of bronchi will be involved. In the more severe cases, nevertheless, the infection can reach as far as the lower lungs [9]. A typical infection starts by inhalation of virions, most of which are eliminated by non-specific clearance mechanisms such as mucus binding. The non-cleared virions infect epithelial cells by attaching to their receptors [17, 9]. The absorption of the receptor bound virions on the cell surface takes 20 minutes via endocytosis [86, 94].

Once inside the epithelial cell, the virions replicate by means of the machinery and resources which, under normal conditions, the cells would use to maintain their functions. This replication occurs when the virions fuse with the endosomal membrane and subsequently, viral nucleic acid is uncoated and transcribed; then the protein is synthesized, assembled and finally released into the extracellular environment [112, 107]. The period during the binding and the release of new virions is called eclipse phase, which lasts between 5 and 12 hours post infection (p.i.) [17, 9, 56].

The fast replication of virions results in an exponential growth, typically reaching the peak of infection at day 2 or 3 p.i. [112]. The clearance of the infection usually takes place around day 5 and 10 p.i. Due to the high infection rate of the virus, the innate immune response, whose main components are NK cells and interferons, plays an important role [27, 102, 107]. The adaptive immune cells, mainly CTLs, and the specific antibodies, peak after day 7 and contribute to the final clearance of the infection. However, in the case of a secondary infection, antibodies and CTLs can respond around day 3 p.i. [17, 9].

Programmed cell death by apoptosis is deeply related to different aspects of the IAV infection. Several researches have reported that IAV uses apoptosis resources to

facilitate its replication. During the first stage of the infection, IAV inhibits apoptosis by up-regulating the anti-apoptotic pathway PI3 K-AKT, in order to gain time to replicate. Afterwards, the virus induces apoptosis by up-regulating the pro-apoptotic p53 pathway, allowing a more efficient release of virions [130, 127, 124].

2.4 Immune response to influenza A virus infection

2.4.1 Innate immune response

Influenza viral infection stimulates the activation of the immune response – adaptive and innate– so that the pathogen can be cleared. The main characteristic of the innate immune response is to provide resistance to pathogens – viruses and bacteria– in a nonspecific manner. Nevertheless, recent studies have proved the critical role of the innate immune response during the clearance of IAV [95, 118, 78].

The first line of defense consists of physical barriers, i.e. the airway tract mucosa. Its main function is to protect the lungs from pathogen and external threats [41]. Nonetheless, if the viruses are able to successfully go through the mucous layer, they will bind and infect the epithelial cells of the upper respiratory tract. The recognition of infected cells by innate immune cells results in the production of pro-inflammatory cytokines. Type I Interferon (IFN) limits significantly the ability of the virus to infect the target epithelial cells and to replicate within the infected epithelial cells [99].

High levels of cytokines and chemokines recruit and activate different immune cells involved in the innate immune response, such as NK cells, neutrophils, macrophages and dendritic cells [59, 107]. Activated neutrophils phagocytose the apoptotic infected cells and secrete pro-inflammatory cytokines [38, 107]. Furthermore, neutrophils regulate the specific CTLs response [58]. Activated macrophages, on the other hand, play a key role as antigen presenting cells during the IAV infection and in the production of pro-inflammatory cytokines [120, 107]. Tumpey et al. showed that depletion of macrophages before day three p.i. results in a rapid viral replication [120].

Dendritic cells are antigen-presenting cells. During an IAV infection, dendritic cells migrate at a high rate to the draining lymph nodes of the lung [73]. This high rate migration can persist up to day 7 p.i., depending on the viral dose and virus strain [11]; however, different studies have proven that dendritic cells accumulate into the lung without any further migration after day 5 p.i. [60]. Antigen presentation can occur via MHC class I and II [20]. The antigen can be taken either from the infected cell or from apoptotic infected cells [61]. Bender et al. [12] showed that IAV is able to directly infect and replicate within dendritic cells. Nonetheless, this replication is abortive, i.e. the new formed virions are not infectious.

Another important component of the innate immune system is the NK cells. These granular lymphocyte cells play a major role in containment and clearance of infection by inducing apoptosis in infected cells [75]. Cytotoxic activity of NK cells is regulated by the recognition of activating and inhibitory receptors expressed in their surface and in the target cell membrane [70]. Different combinations of activating and inhibiting ligands expressed by NK cells allow them to respond to different pathological stimuli [75]. Inhibition of cytotoxic activity of NK cells occurs upon recognition of the major histocompatibility complex (MHC) class-I on target cells. Viral infected cells and tumor cells downregulate MHC class I. This prevents CTLs recognition but makes them vulnerable to NK cell-mediated killing [75]. Once the infected cell is recognized, NK cells form pores in the membrane of the target cell by means of perforin; through these pores, granzyme and other enzymes enter the cell, which triggers apoptosis [75].

During an IAV, NK cell receptors NKp44 and NKp46 recognize the hemagglutinin (HA) proteins, expressed on the membrane of influenza A infected cells [11, 6]. This recognition allows the NK cell to induce apoptosis in the infected cell via perforin/granzyme mechanism [14].

2.4.2 Adaptive immune response

The adaptive immunity consists of a specialized set of cells in charge of eliminating specific pathogens. The main components of this part of the immune system are B- and T- lymphocytes. During the influenza viral infection, the number of influenza-specific CTLs increases around day 5 p.i. [73, 45]. These cells accumulate in the lungs in order to clear the infection [73].

Another important component of the adaptive immune response is the $CD4^+$ T cell. The most important activity performed by $CD4^+$ T cells is to provide support during the priming of CTLs, by producing IL-2 and IFN-γ in the draining lymph, crucial cytokines for the proliferation of CTLs [3, 119]. As mentioned above, although $CD4^+$ T cells are not critical for the clearance of the infection, a deficient number of them affect the cytotoxic functions of the CTLs [63].

Influenza-specific antibodies are produced by B cells. These antibodies have two different functions during viral clearance. The first one is to obstruct the binding of the virus to the epithelial cells, by blocking the receptor that allows endocytosis (Anti-HA antibodies). The second one is to regulate the proteins required for the release of the new virions; by doing so, they are able to restrict the propagation of the viruses (Anti-NA antibodies) [126, 62, 107].

3 Mathematical framework

Herein, the main mathematical concepts used in the development of this work are presented. At the end of the chapter, a summary of the state of the art of mathematical modelling of influenza A virus infection is provided.

3.1 Mathematical modelling of dynamical systems and statistical model for the experimental data

In this section, the concepts of dynamical models, statistical models for parameter estimation of ODEs and Markov Chain Monte Carlo (MCMC) methods are introduced.

3.1.1 Modelling of dynamical systems

A dynamical system is a system which evolves in time under external excitation. Such systems are often described by deterministic mathematical models, i.e. random events do not affect the evolution in time of the state variables.

The mathematical modelling of dynamical systems provides a deeper understanding of the intricate mechanisms of the system, the effects of its different components and quantitative predictions up to a certain level of precision. Moreover, computer simulations can be utilized to evaluate dynamical systems under different conditions by means of such models, instead of performing expensive or impractical experiments. Additionally, the development of mathematical models, explaining repeatable experimental results, often leads to important theoretical discoveries [42, 129, 22].

Dynamical models are governed mostly by ODEs. ODEs can be defined as a set of equations written in terms of deterministic functional relationships between the state variables and its derivatives with respect to one independent variable, time. Mathematically, this can be described as follows:

Let $\mathbf{x}(t) \in \mathbb{R}^N$ be a vector of unknown state variables at the time t, whose time-evolution is described by a system of different equations, $\mathbf{f}$. This is written in the following way:

$$\frac{d\mathbf{x}(t)}{dt} = \mathbf{f}(\mathbf{x}(t), t, \theta), \tag{3.1}$$

where $\theta \in \mathbb{R}^p$ represents the p parameters of the equations and $\mathbf{f} \in \mathbb{R}^N$ is a vector of N functions describing the change of the states variables in time. Unique solutions of such systems depend on the initial conditions $\mathbf{x}_0 = \mathbf{x}(t_0)$, where t_0 is the initial time.

Achieving the analytical solution of such problems may not always be a feasible task, due to complex geometries, non-linearities, etc. Hence, numerical methods arise as an alternative to such problems. These methods allow obtaining numerical solutions of differential equations with a certain level of accuracy. By means of numerical methods, the ODEs are discretized, –the infinite states of a system in a given time interval become finite–, so that the future state can be approximated from the current state by an algebraic equation. The selection of such methods, however, must be carried out with care as their results can be heavily affected by the specific structure of the model, its geometrical characteristics and the values of the parameters [48].

3.1.2 Statistical model for the experimental data

Uncertainties of a true state $\mathbf{x}(t) \in \mathbb{R}^N$ of a system can arise due to uncertain initial conditions, uncertainty in the model description or both. Let $\mathbf{y}(t) \in \mathbb{R}^M$ be a vector of observables at time t, which depends linearly on the true state $\mathbf{x}(t)$ but it is disturbed by the associated error of measurements ϵ. Then, the statistical model can be described as follows:

$$\mathbf{y}(t) = \mathbf{H}\mathbf{x}(t) + \epsilon, \tag{3.2}$$

where $\mathbf{H}$ represents a linear measurement operator mapping $\mathbb{R}^N \to \mathbb{R}^M$ [22, 88]. Note that $M \leq N$, since usually not all the states involved in a dynamical system can be measured. In fact, the observables are often combinations of two or more states, in either a linear or a non-linear manner. The error of measurements ϵ is often assumed to follow a Gaussian distribution; although this assumption may not always be correct.

3.2 MCMC methods for parameter estimation

Herein, the main statistical concepts, required to accomplish the parameter estimation in the framework of the MCMC methods are introduced.

3.2.1 Bayesian inference

Since the behavior of an ODE model can be strongly altered by the value of its parameters, a proper estimation of these components is crucial for understanding the

mechanism behind the corresponded dynamical system. Nevertheless, an exact estimation of such parameters is an infeasible task as a mathematical description of the natural world is limited and the available data is usually incomplete and subjected to errors [125]. Additionally, methods for direct measurements of parameters are often nonexistent or lead to noisy results, especially in biology. Therefore, mathematical and numerical methods have to be applied in order to infer the parameters from noisy data. This is the so-called inverse problem. The inference is accomplished by finding a set of parameters, so that the outputs of the model fit the experimental data. However, as the complexity of the dynamics increases, parameter inference becomes convoluted [111].

Two main strategies can be used to infer parameters of a model, the frequentist and the Bayesian approach. In the frequentist approach, the estimation procedure consists of finding a unique set of parameters $\theta \in \mathbb{R}^p$ (where p is the number of parameters) which maximizes the likelihood function $\mathcal{L}(\theta) = \Pr(\mathbf{y}|\theta)$, where $\mathbf{y} \in \mathbb{R}^M$ represents the data and Pr is the probability function. From this approach, the least square estimation method arises [125, 18].

The frequentist approach, nonetheless, can present several problems. Consider, for example, a parameter θ_i whose changes have an insignificant effect on the model output. Then θ_i is considered to be unidentifiable. Such a situation can occur due to measurement uncertainty and model structure [111, 96]. In this case, a collection of most probable values of θ_i, rather than the unique most probable one, should be computed, as reliable results in the parameter estimation are required to make a high quality prediction of the dynamical system [22]. Furthermore, even if the most likely set of parameters is able to exactly fit the data, they may fail to accurately predict future behaviors or fit additional measurement. This phenomenon is known as over-fitting [21, 29, 15].

The Bayesian approach, on the other hand, provides distributions of parameters given prior knowledge and a set of measurements. In the Bayesian framework, measurement uncertainties propagate in the system in a mathematically consistent manner. Additionally, assumptions are explicitly incorporated and the knowledge –posteriors– can be updated as more data is acquired [125].

Bayesian inference is based on the Bayes' theorem. This theorem describes the conditional probability of an event A given an event B, as a function of the probability of A and B and the probability of the event B given the event A, i.e.

$$\Pr(A|B) = \frac{\Pr(B|A)\Pr(A)}{\Pr(B)}. \tag{3.3}$$

Therefore, the posteriors of the ODEs parameters θ, given a data $\mathbf{y} \in \mathbb{R}^M$, are proportional to the prior of the parameters $\pi(\theta)$, multiplied by the joint likelihood

of the data given data model outputs $\mathbf{x}(\theta) \in \mathbb{R}^N$ as a function of the parameters. Mathematically, this is described as follows:

Assuming that M is equal to N,

$$\Pr(\theta|\mathbf{y}) = \frac{\Pr(\mathbf{y}|\mathbf{x}(\theta))\,\pi(\theta)}{\Pr(\mathbf{y})} = \frac{\Pr(\mathbf{y}|\mathbf{x}(\theta))\,\pi(\theta)}{\int Pr(\mathbf{y}|\mathbf{x}(\theta))\,\pi(\theta)\,d\theta} \quad , \tag{3.4}$$

where, $\Pr(\mathbf{y})$ represent the marginal likelihood, i.e. the probability of y without reference to $\mathbf{x}(\theta)$. The marginal likelihood normalises the posterior density $\Pr(\mathbf{y}|\mathbf{x}(\theta))\,\pi(\theta)$, i.e. the conditional probability of $\mathbf{y}$ given $\mathbf{x}(\theta)$ times the prior of parameters [15, 125, 64, 97].

3.2.2 Monte Carlo methods

Obtaining analytical solutions of integrals such as the one presented above (equation (3.2.1)), is often an infeasible task. Numerical methods such as Gauss Quadrature could be utilized to obtain approximations of them [48]; however, these methods are based on space discretization, leading to larger computational complexities as the dimension of the problem increases. In such situations, Monte Carlo methods can be a very useful tool.

Monte Carlo methods are based on the idea of approximating expectations of functions under a probability distribution (known as target density), by drawing a set independent samples from it [111, 74]. Therefore, the sampling of the target density allows to perform convoluted computations by using simple statistics. This idea is especially useful when dealing with high dimensional probability distributions.

Given R sample from $\mathbf{z} \sim \Pr(\mathbf{z})$, the integral of a function $f(\mathbf{z})$ can be approximated using the Monte Carlo estimator, as follows:

$$\int f(\mathbf{z})P(\mathbf{z})d\mathbf{z} \approx \frac{1}{R}\sum_{r=1}^{R} f\left(\mathbf{z}^{(r)}\right). \tag{3.5}$$

This estimator is unbiased and converges to the true value of the integral as $K \to \infty$. In order to draw samples from a distribution different methods such as the inverse transform method, accept-rejects methods and Markov Chain can be used [97].

3.2.3 Markov Chain

A Markov Chain is a stochastic process, describing a sequence of events in which the probability of the current state i depends uniquely on the previous state $i-1$

[39, 5, 43]. This is the so-called Markov property, which can be mathematically described as follows:

$$\Pr\left(x^{(i)}|x^{(i-1)},...,x^{(0)}\right) = \Pr\left(x^{(i)}|x^{(i-1)}\right). \tag{3.6}$$

The collection of events in a Markov Chain is called state space. In discrete cases, the transition between states can be described by the transition probability Matrix or Markov Kernel $P = [p_{ij}]$, where each element p_{ij} represents the probability of moving from state i to the state j. If the transition probability Matrix does not change over time, the Markov Chain is considered time homogeneous. The Markov Chain process possesses a series of properties that are ideal to accomplish the sample needed to perform Monte Carlo approximations of high dimensional integrals. Among these properties, the most important ones are irreducibility, aperiodicity and recurrence.

A Markov Chain is considered irreducible if any point $x^{(i)}$ in the Chain can be reached with a positive probability after a certain time t, regardless of the initial point $x^{(j)}$. This is defined as follows:

$$\Pr\left(x^{(i)}|x^{(j)}\right) = p_{ij}^{t} > 0, \tag{3.7}$$

where p_{ij}^{t} is the probability of moving from the state i to the state j after a time t. Markov Chain is periodic if, given the state $x^{(i)}$ as initial state, $x^{(i)}$ is periodically achieved after multiples of k steps; otherwise, the Markov Chain is aperiodic. Periodicity is mathematically expressed as follows:

$$k = \gcd\left\{n > 0 : \Pr\left(x^{(i)}|x^{(i)}\right)\right\} > 0, \tag{3.8}$$

where gcd is the greatest common divisor and n is a natural number. If $k = 1$, the Chain is aperiodic.

Another important property of the Markov Chain is the recurrence. This property guarantees that, given a state $x^{(i)}$, there is a probability of 1 to return to it after a time t, that is:

$$\Pr\left(x^{(i)} \text{ for some } t > 0 \mid x^{(i)}\right) = 1. \tag{3.9}$$

Finally, a finite time homogeneous Markov Chain that is irreducible and aperiodic has a unique stationary distribution π and the Chain will converge in the sense of distributions from any initial distribution.

3.2.4 Markov Chain Monte Carlo

Metropolis et al. [80] were the first to suggest the usage of Markov Chains to draw samples from any arbitrary distribution. Since then, more sophisticated methods based on this idea have been developed. By means of MCMC methods, a Markov Chain is simulated such that its stationary distribution is the target distribution. Nevertheless, the samples obtained from Markov Chains are correlated samples from the target distribution (as the current state depends on the previous one); thus, a MCMC able to reduce such correlations as much as possible is desirable. For this purpose, defining a transition density able to explore the distribution space and propose minimally correlated states is crucial [74, 111, 22]. Different algorithms have been proposed for accomplishing such a task, which are introduced below.

Metropolis Hasting algorithm.

The standard MCMC is based on the metropolis-hasting algorithm. The goal is to carry out a random walk to explore the state space, by sampling from an initial distribution. The exploration is then modified by probabilistic rules, i.e. acceptance and rejection of proposed states, such that the random walk sample the target distribution [74, 111]

This algorithm, as presented in table 3.1, was developed by Hasting [52], who proposed a more general application of Markov Chains sampling since at the time, it was used mostly for statistical mechanic problems. Given the random variable φ, which will be sampled, the proposal density $Q(\varphi_p|\varphi_c)$ is used to draw the proposed state φ_p, according to the current state φ_c. Metropolis' original idea required the proposal density to be symmetric, while Hasting proposed it to be any normalised probability distribution. Once the proposed state φ_p is sampled, the acceptance ratio α is calculated as indicated in table 3.1. Therefore, the proposed state is accepted with probability α. If φ_p is rejected, a new candidate state is drawn from the proposal density. This is an iterative process and the stop condition depends on the convergence of the target distribution. In the algorithm, the Matrix Σ is the variance of the proposal density, which must be tuned.

Table 3.1: Metropolis-Hasting algorithm

1. Given the current State φ_c, draw a proposed state φ_p from the transitional kernel $Q\left(\varphi_p|\varphi_c, \Sigma\right)$.
2. Compute the acceptance ratio $\alpha = \min\left[1, \frac{Q(\varphi_c|\varphi_p,\Sigma)\pi(\varphi_p)}{Q(\varphi_p|\varphi_c,\Sigma)\pi(\varphi_c)}\right]$.
3. Draw u from $U[0,1]$, where $U[0,1]$ is a uniform distribution.
4. If $u < \alpha$ then $\varphi_c = \varphi_p$ otherwise $\varphi_c = \varphi_c$.

Hamiltonian Monte Carlo

Hamiltonian dynamics is a reformulation of the classical mechanics based on Newton's equations of motion. In this context, a closed system can be described by generalized coordinates and their momenta [50]. Hamiltonian Monte Carlo is a metropolis method, which uses Hamiltonian dynamics as a proposal mechanism. This method reduces the random walk by using gradient information of the target distribution, leading the space exploration towards the states with the highest probabilities. In the Hamiltonian Monte Carlo method, there are two type of proposals, a random proposal for the momentum variable $\mathbf{p}$, leaving the state space φ unaltered and the second proposal which changes φ and $\mathbf{p}$ using the Hamiltonian dynamics [74]. Hamiltonian function is defined as follows:

$$H(\varphi, \mathbf{p}) = E(\varphi) + K(\mathbf{p}), \tag{3.10}$$

where $K(\mathbf{p})$ represents the kinetic energy and $E(\varphi)$ the potential energy. The density of $\mathbf{p}$, $\Pr(\mathbf{p})$, is given by $\mathcal{N}(\mathbf{p}|0, \mathbf{M})$, where $\mathbf{M}$ is a diagonal Matrix, known as mass Matrix. $\mathbf{M}$ is associated with the directions in the state space. φ and $\mathbf{p}$ allow to create samples by means of the joint density, which is described as follows:

$$\Pr(\varphi, \mathbf{p}) = \frac{1}{Z_H} e^{-H(\varphi,\mathbf{p})} = \frac{1}{Z_H} e^{-E(\varphi)} e^{-K(\mathbf{p})}, \tag{3.11}$$

where Z_H is the normalization constant. Since the density $\Pr(\varphi, \mathbf{p})$ is separable, a sequence of sample $\{\varphi^{(t)}\}$ can be obtained by discarding the momentum variables $\{\mathbf{p}^{(t)}\}$ [74].

The potential energy and the kinetic energy are mathematically represented as follows:

$$E(\varphi) = -\log \Pr(\varphi) - \log Z_E, \tag{3.12}$$

$$K(\mathbf{p}) = \frac{\mathbf{p}^\intercal \mathbf{M}^{-1} \mathbf{p}}{2}. \tag{3.13}$$

Therefore, the deterministic proposal for the state space φ is accomplished by solving the following system of equations, obtained by means of calculus of variations [40]:

$$\frac{d\varphi_i}{dt} = \frac{\partial H(\varphi, \mathbf{p})}{\partial p_i} = [M^{-1}p]_i, \tag{3.14}$$

$$\frac{dp_i}{dt} = \frac{\partial H(\varphi, \mathbf{p})}{\partial \varphi_i} = -\frac{\partial E(\varphi)}{\partial \varphi_i} = \frac{\partial \log \Pr(\varphi_i)}{\partial t}. \tag{3.15}$$

The analytical solution of such systems is usually not possible. Therefore, numerical methods are required to obtain approximated solutions. The Hamiltonian system must be solved with symplectic numerical methods, such as the leapfrog algorithm, guaranteeing that the geometrical conservative properties of Hamiltonian systems are preserved [48].

Nevertheless, every numerical integration procedure presents an associated error; thus, the obtained sample does not belong to the target distribution. This problem is addressed by embedding the Hamiltonian Monte Carlo proposal within a Metropolis algorithm as presented in table 3.2. In the algorithm, the parameters ϵ, L and the matrix $\mathbf{M}$ must be tuned.

Table 3.2: Hamiltonian Monte Carlo algorithm

1. Given the current State φ_c, generate a random momentum $p_c \sim \mathcal{N}(\mathbf{0}, \mathbf{M})$.
2. Calculate $E = -\log \Pr(\varphi_c)$ and $\frac{\mathbf{p_c^T M^{-1} p_c}}{2}$.
3. Propose φ_p and $\mathbf{p}_p$ by solving the Hamiltonian System for a step ϵ for L iterations.
4. Calculate $E = -\log \Pr(\varphi_p)$ and $\frac{\mathbf{p_p^T M^{-1} p_P}}{2}$.
5. Calculate the acceptance ratio $\alpha = \min\left[1, e^{(H(\varphi_c p_c)) - (H(\varphi_p p_p))}\right]$.
6. Draw u from $U[0,1]$, where $U[0,1]$ is a uniform distribution.
7. If $u < \alpha$ then $\varphi_c = \varphi_p$ otherwise $\varphi_c = \varphi_c$.

Metropolis adjusted Langevian Monte Carlo

Metropolis adjusted Langevian Monte Carlo method uses Langevian diffusion equation as a proposal mechanism. This stochastic differential equation describes the random movement of molecules in Brownian motion and is defined as follows:

$$d\varphi(t) = \frac{1}{2}\frac{\partial \log \Pr(\varphi)}{\partial \varphi}dt + d\mathbf{Z}(t), \tag{3.16}$$

where $\mathbf{Z}$ denotes the d-dimensional Brownian motion. After applying the first order Euler method, the discretized equation is defined as:

$$\varphi_{\mathbf{n+1}} = \varphi_{\mathbf{n}} + \frac{\epsilon^2}{2}\frac{\partial \Pr(\varphi)}{\partial \varphi} + \epsilon\mathbf{Z}, \tag{3.17}$$

where $\mathbf{Z} \sim \mathcal{N}(\mathbf{0}, \mathbf{I})$, $\mathbf{I}$ is the identity matrix and ϵ is the step size of the Euler method. As in the previous case, the target distribution differs from the one obtained by this method due to discretization errors. Therefore, the Metropolis-Hasting algorithm is used to correct the approximation errors, guaranteeing the convergence to the target distribution [44].

Let denote

$$\mu(\varphi, \epsilon) = \varphi + \frac{\epsilon^2}{2}\frac{\partial \Pr(\varphi)}{\partial \varphi}. \tag{3.18}$$

Then, the proposal density is defined as:

$$Q(\varphi_{\mathbf{p}}|\varphi_{\mathbf{c}}) = \mathcal{N}(\varphi_{\mathbf{p}}|\mu(\varphi, \epsilon), \epsilon^2\mathbf{I}), \tag{3.19}$$

with acceptance probability:

$$\alpha = \min[1, \frac{\pi(\varphi^p)Q(\varphi_{\mathbf{p}}|\varphi_{\mathbf{c}}))}{\pi(\varphi^c)Q(\varphi_{\mathbf{c}}|\varphi_{\mathbf{p}}))}] \tag{3.20}$$

Note that metropolis adjusted Langevian Monte Carlo does not use gradient information of the parameter space. Thus, it may exhibit random walk behavior. Further MCMC methods, which exploit the representation of a statistical model as a Riemannian manifold, have been recently developed [44]. These methods intend to circumvent the tuning required for Hamiltonian Monte Carlo and Metropolis adjusted Langevin algorithms. Nevertheless, as in the Hamiltonian Monte Carlo and Metropolis Adjusted Langevian Monte Carlo, this approach requires a drastic increase of computational time as additional dynamical systems must be solved.

Importance of MCMC Methods

As described above, MCMC methods are sampling algorithms. The idea behind these techniques is to draw random samples from the required distribution by running a Markov Chain for a long period of time. In this section, three algorithms of the MCMC were described: the metropolis-hasting algorithm, Hamiltonian Monte Carlo and Metropolis-Adjusted Langevian Monte Carlo, each of which uses a different approach to construct the Markov Chain.

In this work, the metropolis hasting algorithm was used to estimate the parameters of the proposed IAV model. This method was selected because, unlike the Hamiltonian Monte Carlo and Metropolis-Adjusted Langevian Monte Carlo, it does not suffer the so-called curse of dimensionality, i.e. the probability of rejection does not increase with the number of dimensions.

Another advantage of the metropolis hasting algorithm is the reduced computational time. In order to estimate the parameter distributions of ODE models, the ODE system must be repeatedly solved by numerical methods. For the Hamiltonian Monte Carlo and Metropolis-Adjusted Langevian Monte Carlo, not only the ODE system must be solved, but also additional equations (Eq.(3.2.4) and (3.2.4)), which increases the computing time.

3.3 Akaike information criteria

Akaike Information Criteria (AIC) evaluates the quality of data fit for a set of models with respect to each other. AIC, however, do not asses the absolute quality of a model and is calculated as follows:

$$AIC = 2k - 2\ln \mathcal{L} \tag{3.21}$$

where k represents the number of parameters in the model and $\mathcal{L}$ represents the maximum value of Likelihood function. The selected model will be then the one with the minimum value. Notice from equation 3.21, that AIC includes a penalty for a higher number of estimated parameters, avoiding overfitting problems [21].

3.4 Review of Modelling of influenza A virus infection

Despite numerous researches, there are plenty of aspects of influenza infection that have not been discovered yet. In recent years, however, mathematical modelling has arisen as a tool for a better understanding of the influenza kinetic. The information obtained by such models is critical in the evaluation of new hypotheses, the design of new experiments and the proposal of new and better treatments and therapies against influenza [9].

Mathematical models of influenza infection have allowed estimating kinetic parameters that are difficult or expensive to estimate by means of experimentation. However, a proper estimation of parameters is still a complicated task, especially when the data is limited. In fact, as Beauchemin *et al.* mentioned, there are significant differences in the estimated kinetic parameters, due to different experimental settings, host and influenza A strains [9, 17].

Boianelli *et al.* summarized a general guideline for mathematical modelling. First of all, different models must be formulated. These models must account for hypotheses obtained by analyzing the experimental data. Secondly, the sensitivity analysis of the model must be carried out, i.e. evaluate if the parameters can be uniquely determined, given the experimental data and the structure of the model. Subsequently, an uncertainty estimation of the obtained set of parameters must be carried out to obtain intervals of confidence. Finally, the prediction of the models must be tested in order to propose new knowledge or hypotheses which may lead to the design of new experiments [17].

The most basic mathematical model used to describe the dynamics of influenza infection is the target-cell limited model, which has been previously used for HIV research. This consists of a set of ODEs, representing the populations and interactions of target cells, infected cells and virions. Some authors have included the dynamics of the so-called latent phase in the target-cell limited model, so that the time period between the viral binding and the beginning of viral production is considered. In the latter model, the target cells get infected by the virus. These recently infected cells undergo eclipse phase and after a certain time, replicate the virus. Afterwards, infected cells die due to apoptosis, while virions decay due to unspecified clearance mechanisms. This model has been widely used to describe both *in vivo* and *in vitro* data. Although immune responses are not explicitly included, their effect is incorporated within the estimated values of the death rate of infected cells and the nonspecific viral clearance. Nonetheless, in some cases, the model predicts that most of the target cells are depleted after 54 hours [9]. This prediction, however, depends on the estimated parameters.

In 1976, Larson et al. proposed a mathematical model to describe the viral infection dynamics in the lungs, trachea and nasopharynx of mice. Even though most of the obtained parameters cannot account for any infection mechanism, this research showed that the primary area of deposition of the virus was the lungs. This information was obtained by evaluating the viral load at each compartment of the respiratory system throughout time. Nonetheless, with a different administration of the viral dose, the main area of infection may change [71].

Baccam et al. studied the infection dynamics of influenza A H1N1 by a target cell limited ODE models, with and without the eclipse phase. The fitted parameters agreed with previous experiments and provided important information about the

kinetics of the infection such as the lifespan of infected epithelial cells and the delay of the eclipse phase. In their research, the antiviral effect of IFN was included in order to cope with a second viral load peak that arose in the simulation. However, Baccam et al. did not perform any sensitivity analysis; thus, the effect of uncertain parameters on the simulation is not considered [8].

Möler et al. investigated the *in vitro* viral replication of IAV H3N8 in animal cells by a system of ODEs. Their set of equations is similar to the target limited cell model; however, the regrowth and death rate of the target epithelial cells, as well as the consumption of the virus by binding, were included. Furthermore, the viral replication was expressed by means of a delay equation, with a lag of 4.5 hours between infection and the beginning of the viral replication. This study also indicated that the viral dynamics does not exhibit major changes if the time delay is neglected [83].

Mathematical modelling has also been used to evaluate and predict drug effectiveness during the influenza viral clearance. Beauchemin et al. analyzed the dynamics of influenza A (H3N2) for different concentrations of the antiviral drug amantadine by means of ODE models. This study allowed them to estimate the efficiency of the drug. Additionally, in this study, Beauchemin et al. found that viral loss due to endocytosis plays a prominent role for the *in vitro* models but not for the *in vivo* models [10].

One of the first mathematical models of influenza viral dynamics that included the immune response, was developed by Bocharov et al. in 1993 [16]. This model includes very detailed interactions among target epithelial cells, infected epithelial cells, virions, macrophages, CTLs, $CD4^+$ T cells, B-cells, antibodies and interferons. In this model, the main source of IFN-α are macrophages infiltrating the airway's epithelium. By including the immune response, Bocharov et al. were able to unravel how each component of the immune response affects the outcome of the influenza viral infection. Furthermore, Bocharov et al. showed that the severity of the infections depends upon virus-epithelial cell interaction rather than upon the immune response [16]. Nonetheless, in this model, the role of the NK cells was not explicitly considered.

Hancioglua et al. presented a mathematical model of IAV infection, including the immune response and epithelial cell regrowth. Additionally, an algebraic equation was included in the ODE model, to calculate the death of epithelial cells, which stimulates the antigen presenting cells and subsequently the IFN production. IFN induces the epithelial cells into a resistance state, while antigen presenting cells (APCs) promote the activation of effector cells, a combination of NK cells and CTLs. In this model, viral absorption rate by epithelial cells, viral clearance by antibody, unspecific clearance and mucociliary removal were explicitly included in the virus dynamics. Moreover, in this research, antibody production depended on antigen presentation.

Their results showed that a small initial viral dose induces an asymptomatic course of the infection. On the other hand, a typical infection can be observed for intermediate viral dose and as expected, the most critical cases arise when a higher viral dose is supplied [51].

In another research, Chang et al. [26] proved as well that the outcome of the infection depends on the initial viral load. Furthermore, Chang et al. showed that infected cell dynamics depends on the interferon while the duration of the infection is mainly determined by the cytotoxicity of CTLs. Similar results were presented by Pawelek et al. [90]. They showed that the decrease in viral dynamics after day 2 p.i. can be explained by interferon activated cells, such as NK cells, during the innate immune response. In this model, the killing rate of infected cells by innate immune cells is assumed to be proportional to IFN dynamics. This study proved that as interferon-induced antiviral effect decreases, the viral load persists or even experiences a second peak, implying the need of the adaptive immune response to explain the final viral clearance. In their research, Pawelek et al. controlled the death rate of virions by assuming it constant initially and as an exponential function after day 6 p.i., in order to emulate the antibodies effect in the viral dynamics. This manipulation, however, may have influenced the overall fitting of the model.

To the best of our knowledge, one of the first IAV models that explicitly incorporated the NK cell dynamics was proposed by Hernandez-Vargas et al. [53]. In this work, the prominent role of the IFN-I and the NK cells in the rapid control of the IAV infection was proved. In a follow-up study, Hernandez-Vargas et al. [54] evaluated the effect of aging in the immune response during the influenza viral infection by proposing different mathematical models and evaluating them with Akaike information criteria. Their results confirm the important role of CTLs for the final clearance of the virus for both young and aged mice. Furthermore, according to Hernandez-Vargas, the fit of the models is not improved by adding the killing by NK cells; however, the control of the infection is still more effective if NK cell dynamics is included.

Recently, Cao et al. [23] investigated by means of an ODEs system the behavior of a secondary influenza infection. In their research, a logistic growth of target epithelial cells as well as a transitory protection effect of IFN is included. Nevertheless, unlike previous studies, this protection effect can be overcome by a sufficiently high viral load. The killing of NK cells was included in the model as a term proportional to IFN. Their results showed that a model with a virus-resistant state is not able to reproduce the observed viral data. In a subsequent research, Cao et al. [24] proposed a model to investigate the role of CTLs on the recovery time after the IAV infection. An exponential relation was predicted, where the recovery time decreases as the number of CTLs increases.

In another research, Miao et al. studied the role of the adaptive immune response

during influenza infection, specifically the role of CTLs and the virus-specific antibodies IgM and IgG [81]. Their investigation showed that IgM is critical during IAV clearance, despite its lower levels in comparison to IgG. Furthermore, Miao et. al suggested that the killing of infected epithelial cells by CTLs has a major impact on the reduction of the viral load. In their work, however, the innate immune response was not included, which may have affected the estimation of the lifespan of infected epithelial cells. Nevertheless, the contribution of nonspecific death rate of infected epithelial cells was higher than the killing by CTLs [81].

3.4.1 Importance of Mathematical Modelling in IAV infection

The usage of mathematical models has been proved to be a valuable tool to design new experiments and to uncover mechanisms of IAV infection, which would have been difficult to find by means of experimentation [17, 8, 9, 104]. In recent years, the increase of data available and new algorithms of parameter estimation have allowed robust development and calibration of IAV models [104]. Nevertheless, there are still many challenges. Even though mathematical models are fitted to experimental data, they are still limited in their prediction capabilities and abilities to resemble some characteristics of the immune responses and viral kinetics [55, 30].

Quantitative results of IAV infections can be altered by different factors, such as virus strains, host and experimental settings [17]. Therefore, for every particular investigation, a new mathematical model should be formulated, so that the most important characteristics of the experiments can be included. In this work, a new IAV model is proposed to account for the specific features of Tafrishi's research [107]. Nevertheless, information from previous models, such as the range of some parameters and ODE structures, was considered in the development of the model.

4 Experimental data: response of WT and vavFLIP$_R$ mice to IAV infection

In order to study the regulation of the extrinsic pathway of apoptosis by c-FLIP$_R$ in immune cells, Tafrishi infected genetically modified mice (vavFLIP$_R$), which constitutively express murine c-FLIP$_R$ in all hematopoietic cells, with IAV [107]. In these experiments, Tafrishi observed a higher viral load in the vavFLIP$_R$ mice, in comparison to WT mice, despite having a higher number of NK cells. According to Tafrishi, the higher accumulation of NK cells exacerbates the IAV infection [107]. In this chapter, a detailed explanation of this and other important results is presented.

In the succeeding chapters, the data introduced herein was used to develop a mathematical model of the influenza infection and to estimate the parameters of the model. Moreover, different hypotheses were proposed and tested in order to explain the experimental results presented in this chapter.

4.1 Lymphocyte population sizes in vavFLIP$_R$ and WT are comparable

Tafrishi [107] evaluated whether the inhibition of death receptor-induced apoptosis alters lymphocyte numbers. For this purpose, lymphocyte populations in the spleen and lymph nodes of 12-17 week old vavFLIP$_R$ and WT littermates were analyzed. As observed in table 4.1, frequencies and total cell numbers of CD3$^+$ CD4$^+$ and CD8$^+$ T cells, CD19$^+$ B cells and NKp46$^+$ NK cells were comparable between both mice groups [115].

Table 4.1: Percentage and absolute cell number of in vavFLIP$_R$ and WT littermates in steady state. Data reproduced from [107] table 1.

Organ	Percentage of all acquired cells				
	CD3$^+$	CD4$^+$	CD8$^+$	CD19	NKP46
Spleen WT	20.6 ± 4.7	10.3 ± 2.7	8.20 ± 1.0	23.4 ± 6.7	0.92 ± 0.5
Spleen TG	21.7 ± 3.5	11.6 ± 2.3	7.45 ± 1.5	22.7 ± 6.4	0.87 ± 0.3
Lymph Node WT	33.9 ± 3.7	23.8 ± 2.5	16.0 ± 2.2	10.5 ± 1.1	0.21 ± 0.03
Lymph Node TG	34.1 ± 2.9	22.1 ± 2.0	17.7 ± 1.0	12.1 ± 1.6	0.19 ± 0.04

4.2 vavFLIP$_R$ mice are more susceptible to IAV infection

vavFLIP$_R$ mice were challenged with IAV in order to evaluate whether expression of c-FLIP$_R$ modifies the immune response during the influenza infection. Tafrishi supplied intranasally a viral dose of 2×10^3 FFU PR8 (H1N1) to vavFLIP$_R$ and WT female mice in the age of 12-17 weeks. Body weight was recorded daily over a period of 14 days p.i..

As presented in figure 4.1, weight loss curves of vavFLIP$_R$ and WT mice were similar during the first days of the infection [107]. Nevertheless, the body weight loss of vavFLIP$_R$R mice was slightly higher than WT mice at the peak of infection. Note that both types of mice were able to recover and regain body weight [107].

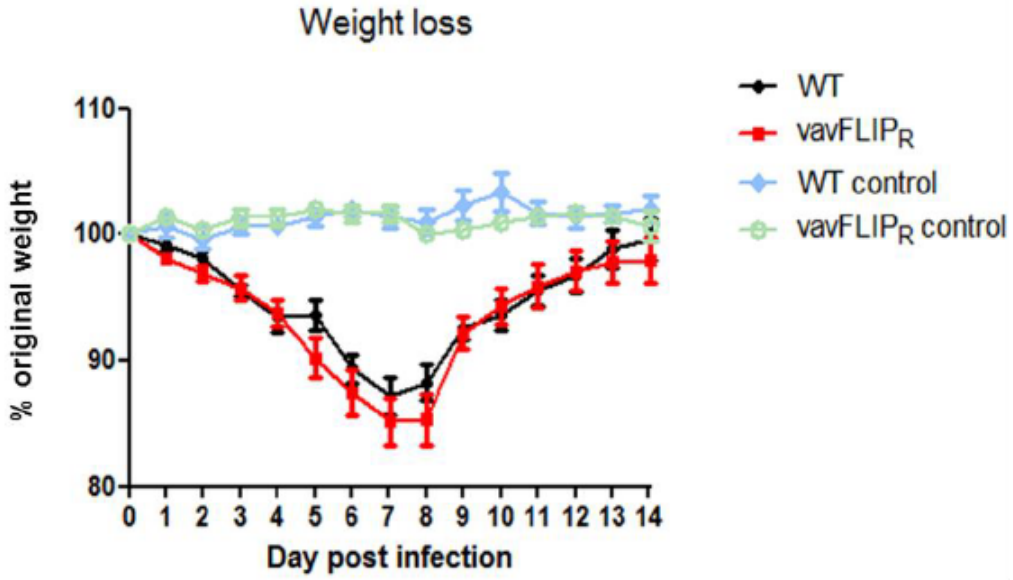

Figure 4.1: Weight loss comparison during an IAV infection. Data are presented as mean value +/- SEM. Data reproduced from [107] Fig. 11a.

The susceptibility of vavFLIP$_R$ mice was further investigated by analyzing the viral load of IAV in the lungs. For this purpose, mRNA copies of the NP gene were measured by Tafrishi [107]. This analysis allowed evaluating whether the vavFLIP$_R$ susceptibility is due to enhancing viral replication and associated tissue damage or a detrimental immune response of the host [107]. During the first days of the infection, the number of NP copies between infected WT and vavFLIP$_R$ mice were similar. However, as the infection progressed, vavFLIP$_R$ mice presented a higher viral load. Results can be observed in figure 4.2. Interestingly, the viral load for both types of mice were below the level of detection at day 10 p.i..

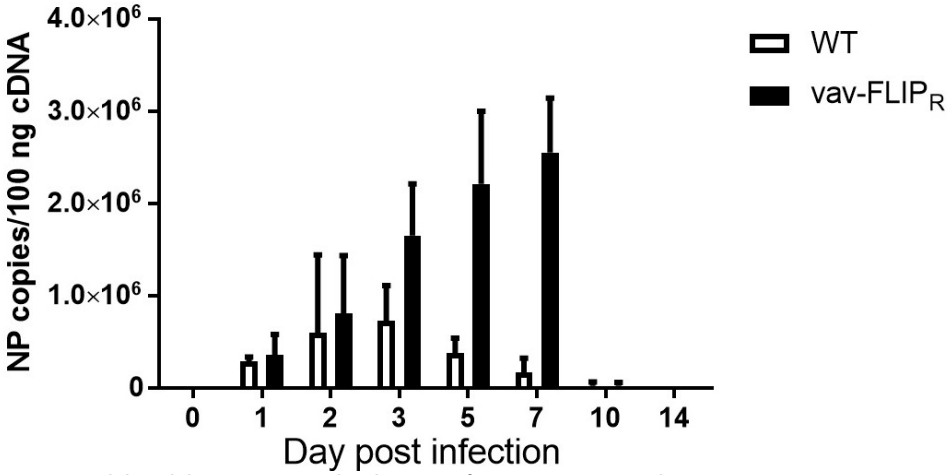

Figure 4.2: Viral load kinetics in the lungs of vavFLIP$_R$ and WT Mouse. Data reproduced from [107] Fig. 12a

4.3 vavFLIP$_R$ mice present higher accumulation of NK cells

Tafrishi [107] quantified NK cells numbers in the draining lymph node of the lung by flow cytometry in order to investigate whether NK cell kinetics presented any alterations in vavFLIP$_R$ mice during an IAV infection. WT and vavFLIP$_R$ mice showed qualitatively similar kinetics throughout the infection as it can be observed in figure 4.3. Note, nonetheless, that on days 5 and 7 p.i., the numbers of NK cells were significantly higher in vavFLIP$_R$ mice.

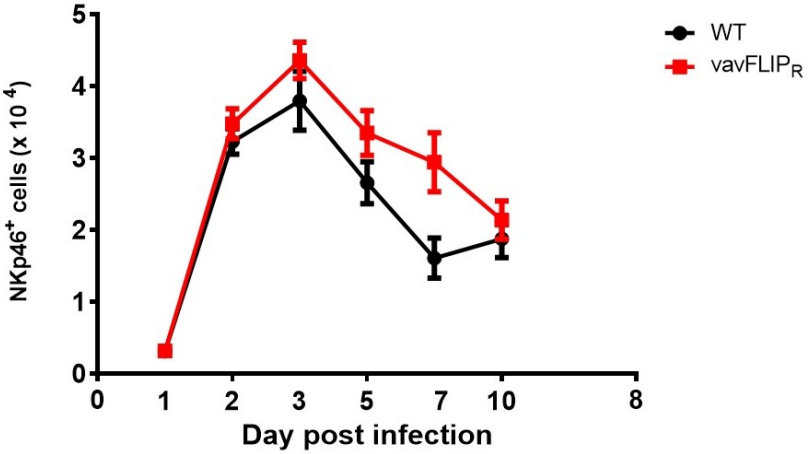

Figure 4.3: NK cell kinetics of vavFLIP$_R$ and WT mouse in draining lymph nodes. Data reproduced from [107] Fig. 18.

4.4 NK cells of vavFLIP$_R$ mice presented lower frequency of active caspase 3

In order to compare NK cells apoptosis in IAV infected vavFLIP$_R$ and WT mice, Tafrishi sorted NKp46$^+$ cells, CD4$^+$ T cells and CTLs from both mice, stained them with active caspase 3/7 stain and analyzed them with flow cytometry [107]. The result indicated that while the frequency of active caspase 3/7 in CD4$^+$ and CD8$^+$ T cells were comparable in both mice, NK cells in vavFLIP$_R$ mice presented a lower frequency of active caspase 3/7 as presented in figure 4.4 [107].

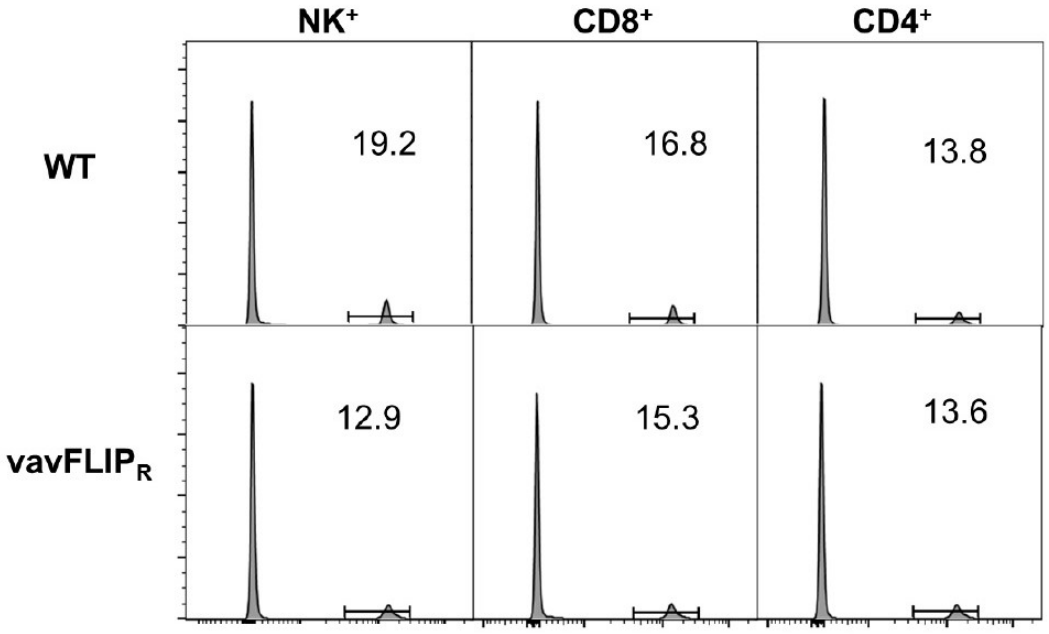

Figure 4.4: Flow cytometry histogram of active caspase 3/7 in vavFLIP$_R$ and WT Mouse. Data reproduced from [107] Fig. 17a.

4.4.1 Degranulation of NK cells is impaired in vavFLIP$_R$ mice during an IAV infection

Tafrishi characterized the functionality of NK cells from spleen by a cytotoxicity assay with YAC-1 target [107]. As it can be observed in figure 4.5, the cytotoxicity of NK cells in both mice was comparable.

In addition, Tafrishi measured NK cells' degranulation with the CD107a assay to investigate c-FLIP$_R$-related changes in their functionality. CD107a is a lysosomal-associated membrane protein used as a marker for NK cells degranulation following stimulation [133, 32, 107]. Tafrishi analyzed the level of CD107a in vavFLIP$_R$ and WT mice during the course of the infection. As illustrated in figure 4.6, the percentages of the CD107a$^+$ within NK cells were significantly lower in infected vavFLIP$_R$.

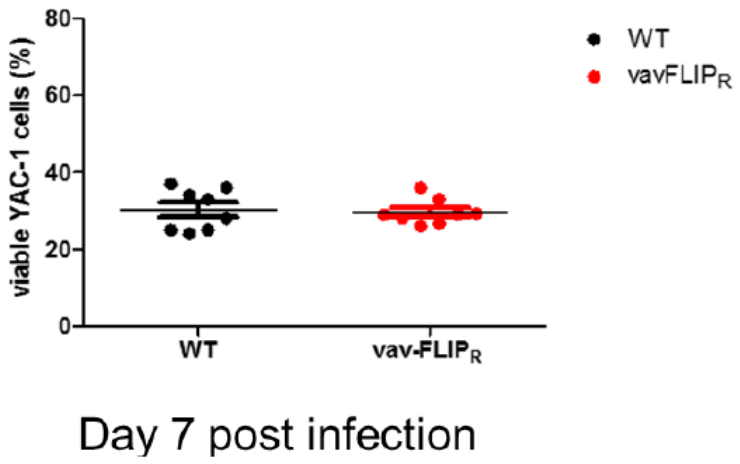

Figure 4.5: Cytotoxicity assay with YAC-1 target cells. Data reproduced from [107] Fig. 21b.

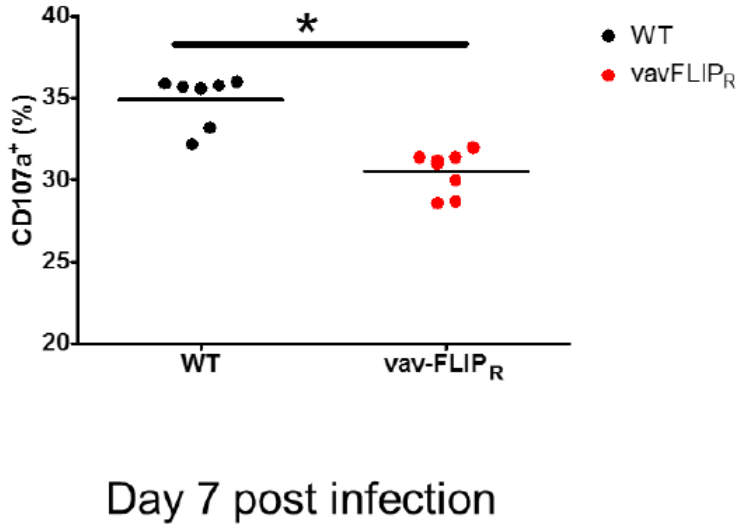

Figure 4.6: Cytotoxicity assay CD107a$^+$. Data reproduced from [107] Fig. 22b.

4.4.2 IAV can infect primary mouse NK cells

Tafrishi [107] investigated the direct effect of influenza virus on NK cells by infecting freshly isolated primary NK cells with H1N1 at a multiplicity of infection (MOI) of 2. Unabsorbed viruses were washed away after 1 hour of interaction. NP gene was detected in influenza virus-exposed NK cells. Purified resting primary human CD4$^+$ T cells were included as a negative control [82], since they cannot be directly infected by the influenza virus. No NP gene was detected in influenza virus-exposed CD4$^+$ T cells. In order to evaluate whether the progeny from infected NK cells was infectious, their supernatants were inoculated onto MDCK cells. The results illustrated that influenza virus could replicate productively in primary NK cells. Note in figure 4.7 that NK cells from vavFLIP$_R$ produced a slightly higher viral load in this *in vitro*

experiment.

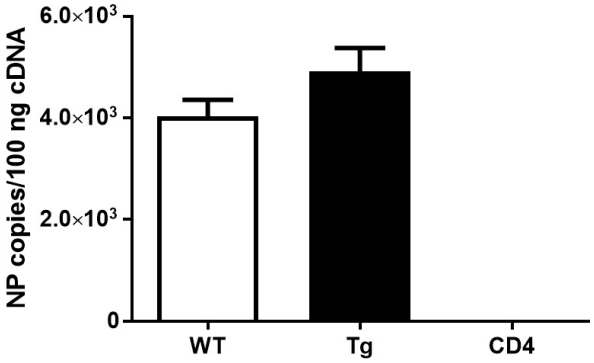

Figure 4.7: Direct infection of NK cells by influenza virus in WT and vavFLIP$_R$ mice. Data reproduced from [107] Fig. 25a.

4.4.3 NK cells depletion results in similar viral load in WT and vavFLIP$_R$ mice

Tafrishi [107] depleted NK cells in both mice using anti-Asialo-GM1 antibody in order to determine the role of NK cells in the higher viral load observed in vavFLIP$_R$ mice. Subsequently, the NK cell depleted mice were infected with 2×10^3 FFU influenza virus and the viral load was measured on day 7 p.i. Note in figure 4.8 that the viral load differences between vavFLIP$_R$ and WT mice disappeared as a result of the NK cells depletion. Such observation suggests that an excessive number of NK cells is involved in higher viral load in vavFLIP$_R$ mice at the peak of infection. However, the viral loads in NK cell depleted mice were higher than the IgG controls.

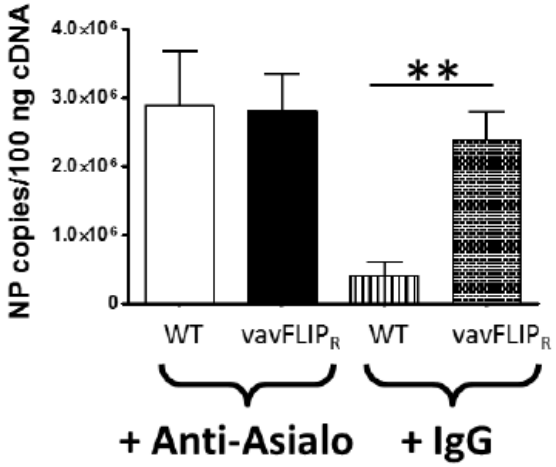

Figure 4.8: Virus titers determined by qPCR and foci assay. Data reproduced from [107] Fig. 24.

4.5 vavFLIP$_R$ mice present higher levels pro-inflammatory cytokines

As pro-inflammatory responses have a definitive role in the pathogenesis of influenza virus, Tafrishi evaluated the contribution of the IFN-γ and $-\alpha$ in the severity of influenza infection in vavFLIP$_R$ mice [107]. The results are presented in figures 4.9 and 4.10. Note that vavFLIP$_R$ presented higher levels of IFN-α at day 2 p.i. as well as a higher peak of IFN-γ at day 7 p.i.. However, no significant differences in the kinetics were observed [108, 107]. The second peak of IFN-α at day 7 p.i. has been observed in different IAV research; nevertheless, to the best of our knowledge, no mechanism has been proposed to explain this reproducible observed kinetic.

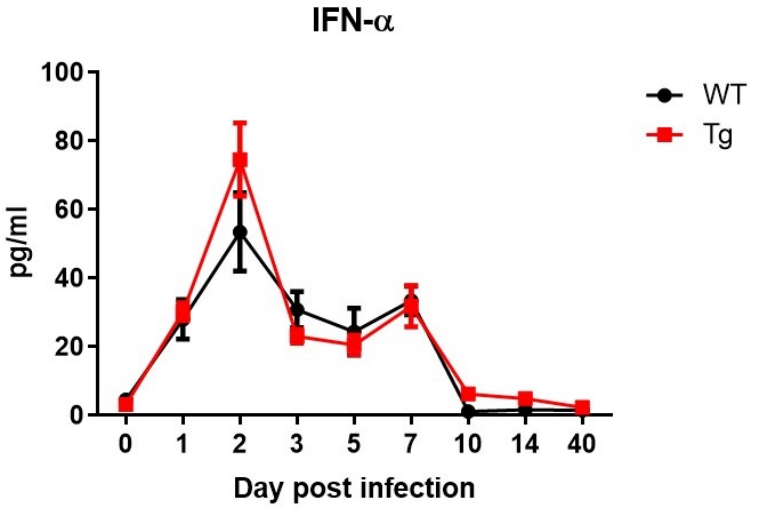

Figure 4.9: Kinetics of IFN-α. Data reproduced from [108]

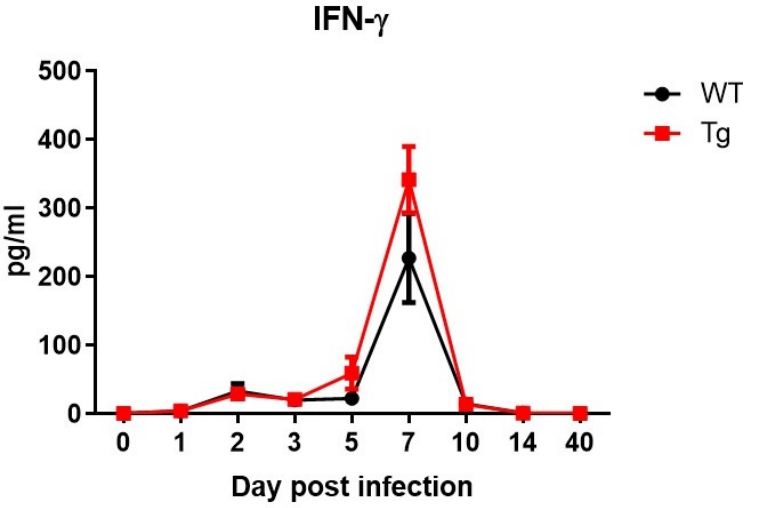

Figure 4.10: Kinetics of IFN-γ. Data reproduced from [108]

4.6 Similar kinetics of CTLs for WT and vavFLIP$_R$ mice

CTLs numbers were quantified by flow cytometry during an IAV infection in the lymph node. The results are presented in figure 4.11 [107]. Following infection, both groups of mice showed similar kinetics. There was, nonetheless, a slight decrease of CTLs at day 7 p.i. in vavFLIP$_R$ [108, 107].

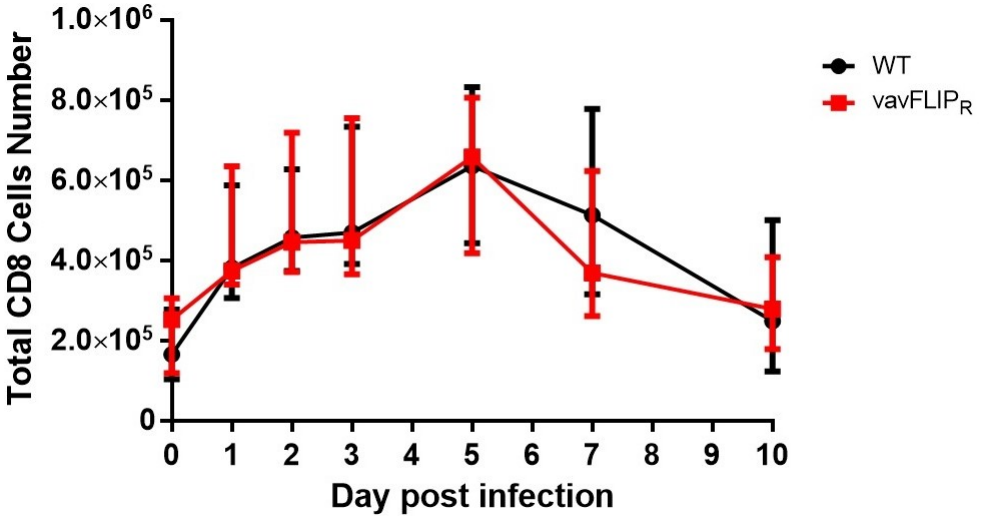

Figure 4.11: CD8$^+$ Dynamics. Data reproduced from [108]

4.7 Summary and open questions

In this chapter, a review of the experimental data obtained by Tafrishi [107] was provided. As mentioned above, in the steady state, vavFLIP$_R$ and WT mice presented similar numbers of immune cells. However, during an IAV infection, vavFLIP$_R$ mice exhibited a higher number of NK cells and a higher viral load in comparison to WT mice. Tafrishi reported that by depleting NK cells in WT and vavFLIP$_R$ mice, the differences in the viral load disappeared. This suggests that a higher number of NK cells contributes to the exacerbation of the influenza infection. Nevertheless, the underlying mechanism behind this result is unknown.

Moreover, Tafrishi demonstrated that IAV can directly infect and replicate in primary murine NK cells, which may be a strategy developed by the virus to evade the NK cells antiviral response. According to Tafrishi, from an intracellular perspective, the main differences between the NK cells of WT and vavFLIP$_R$ mice are the frequency of active caspase 3 and percentage of degranulation [107]. This information is critical for the development of hypotheses that can account for the viral and NK

cell kinetics observed in vavFLIP$_R$ mice. Some of the hypotheses to be tested in this work are presented below.

4.7.1 The possible effects of a lower frequency of caspase 3 in NK cells

Apoptosis resistant NK cells may provide a reservoir for viral replication

The higher viral load exhibited by vavFLIP$_R$ mice may be related to the caspase 3 levels of NK cells. According to Mao et al. [77], influenza virus induces apoptosis in infected NK cells. However, due to the lower frequency of active caspase 3, infected NK cells in vavFLIP$_R$ mice may resist apoptosis. Therefore, less apoptosis in infected NK cells may provide a reservoir for influenza virus to replicate for a longer period of time. This may result in a higher viral load. Apoptosis resistance may also explain the higher accumulation of NK cells observed in the vavFLIP$_R$ mice during influenza infection.

Lower frequency of caspase 3 may enhance the viral replication within infected NK cells

Several researches have reported that IAV may utilize the resources of apoptosis to facilitate its replication [130, 127, 124]. Walter et al. have reported that caspase 3 plays a critical role in the replication of influenza virus within cells [123]. Therefore, lower frequency of active caspase 3 may allow a more effective viral replication within infected NK cells which may account for the results obtained by Tafrishi [107].

4.7.2 The possible effects of impaired degranulation of NK cells

c-FLIP$_R$ may produce changes in the functionality of NK cells

As mentioned above, NK cells of infected vavFLIP$_R$ mice presented impaired degranulation. This may imply that c-FLIP$_R$ expression affects the functionality of NK cells. The reduction of the cytotoxic capabilities of NK cells due to c-FLIP$_R$ expression may allow the virus to use the resources of epithelial cells to replicate for a longer period of time. This may lead to higher levels of viral replication.

5 Model of IAV infection and parameter estimation algorithm

In this chapter, the model, algorithms and numerical methods used in this work are introduced. In the first section, the assumptions of the influenza model and its mathematical description are presented. Subsequently, a detailed explanation of the methodology for the estimation of parameters as well as the solver used to obtain the numerical solution of the ODE model are provided. At the end of the chapter, a simple example is presented in order to demonstrate how the routine of the parameter estimation works.

5.1 Formulation of the IAV infection model

In the proposed model, the viral particles and immune response are interpreted as population dynamics. This is expressed mathematically as a system of ODEs. No spatial distribution of cells, virions and/or molecules is considered; therefore, a homogeneous distribution is assumed. The eclipse phase, i.e. the period of time in which the target cells are successfully infected but do not produce virions [17], is not taken into account. This is justified according to Kaisa et al. [65], showing that the inclusion of cells in the eclipse phase does not improve the quality of the data fit.

The state variables included in this model are target (T) and infected epithelial cells (I), IAV load (V), healthy (N) and infected NK cells (I_N), which are assumed to be the most important components in the early phase of the IAV infection. The proposed model allows to evaluate the role of the NK cells in the clearance of the virus in the early stages of the infection, as well as their interactions with the virus. Nevertheless, starting from day 5 p.i., other adaptive immune components are engaged into the process.

The interactions between the host cells and viruses are presented in figure 5.1. The set of equations representing the infection dynamics and the antiviral response is as follows:

$$\frac{dT(t)}{dt} = -\delta V(t)T(t) \tag{5.1}$$

$$\frac{dI(t)}{dt} = \delta V(t)T(t) - \xi N(t)I(t) - \mu_I I(t) \tag{5.2}$$

$$\frac{dV(t)}{dt} = \rho_V I(t) + \gamma\rho_V I_N(t) - \mu_V V(t) \tag{5.3}$$

$$\frac{dN(t)}{dt} = \rho_N I - \alpha\delta V(t)N(t) - \mu_N N(t) \tag{5.4}$$

$$\frac{dI_N(t)}{dt} = \alpha\delta V(t)N(t) - \mu_{I_N} I_N(t) \tag{5.5}$$

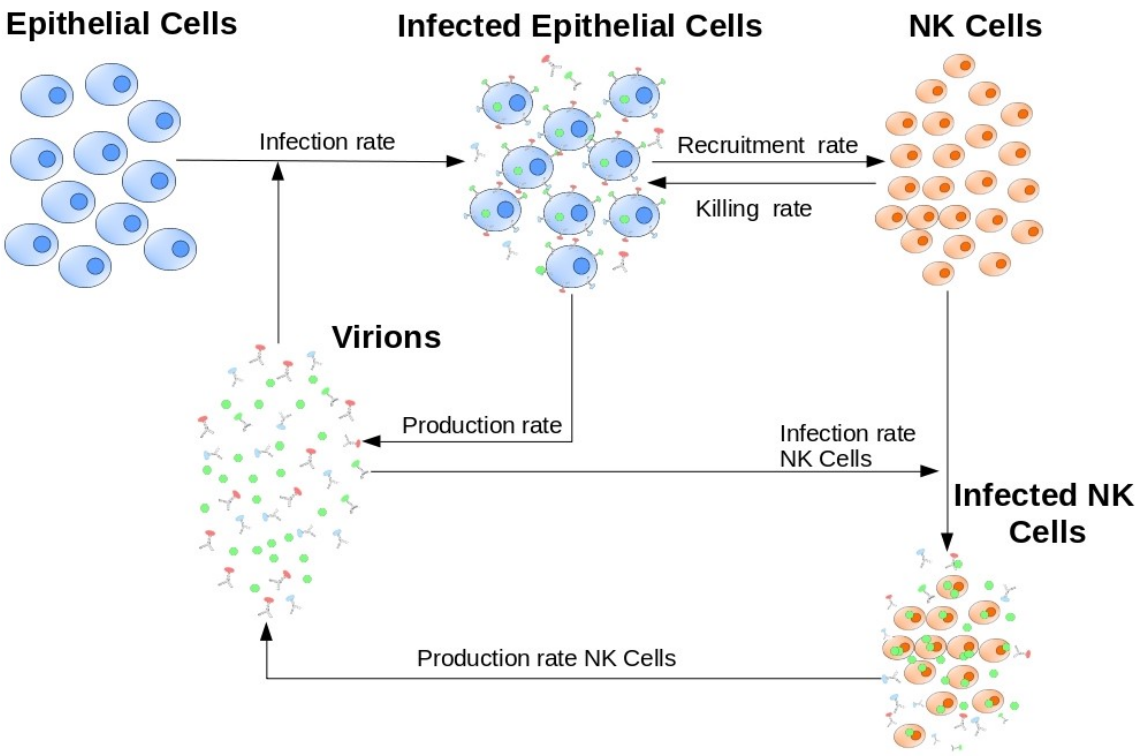

Figure 5.1: Schematic representation of the influenza model. Epithelial target cells T get infected by IAV V. The newly infected epithelial cells I produce virus V and recruit NK cells N, which in turn contain the infection by killing infected epithelial cells I. NK cells N get infected by IAV V. The newly infected NK cells I_N produce the virus V until they die.

Equation (5.1) represents the dynamics of target epithelial cells, which become infected by virus binding at a rate δ. The protection of target epithelial cells by type I IFN is neglected since its effect is temporal. However, such temporal protection may affect the estimation of the infection rate δ. Many authors differentiate between susceptible target cells and protected or resistant target cells by including the dynamics of the latter one [51, 65, 23]. However, under this consideration, the possibility that protected cells may get infected by a sufficiently high concentration of virions is neglected [16]. Recently, Cao et al. [23, 24] incorporated a logistic growth term in the dynamics of target epithelial cells, in order to account for the recovery of the tissue at later stages of the infection. In this work, this term is also neglected as the recovery process is slow and negligible during the 14 days of the IAV infection, as stated by Miao et al. [81].

The dynamics of infected epithelial cells is introduced in equation (5.2). Infected epithelial cells have a mean lifespan of $1/\mu_I$. According to Guo et al., cytotoxic potential of NK cells is significantly down-regulated when infected by influenza virus [47]. Hence, killing of infected epithelial cells is assumed to be accomplished only by healthy activated NK cells at a rate ξ. As explained in the section 4.7.2 of the previous chapter, c-FLIP$_R$ may affect the cytotoxicity of the NK cells of vavFLIP$_R$ mice. Therefore, the value of the killing rate ξ may be different in the vavFLIP$_R$.

Equation (5.3) describes the rate of change of the viral load, whose components are the viral production by infected epithelial and NK cells and an unspecified decay rate. Viral loss due to endocytosis is neglected since according to Beauchemin [10], this process plays no prominent role for *in vivo* models. Since eclipse phase is not considered in the model, the newly infected epithelial cells begin to produce virus immediately at a rate ρ_v. Experimental data showed that infected NK cells are able to replicate infectious virus particles [107]. However, this viral replication is assumed to be less efficient than within infected epithelial cells. Therefore, viral replication of infected epithelial cells ρ_v is restricted by the parameter $\gamma \in [0, 1]$. This guarantees a viral production less than or equal to the one of infected epithelial cells. Additionally, this approach reduces the search in the parameter space. The lifespan of the virus is $1/\mu_V$. This term represents mechanisms that cannot be explicitly incorporated in the model, such as mucociliary clearance, decay of the virus that are not able to bind to any cells and neutralization by antibodies at the advanced stages of the infection.

The dynamics of NK cells is introduced in equation (5.4). The recruitment of these cells depends on the dynamics of infected epithelial cells (I), modeled in the equation by the term $\rho_N I$. Since NK cells are not the main target of IAV, they are assumed to be infected at a rate less than or equal to the one of the target epithelial cells; therefore, the infection rate of epithelial target cells δ is multiplied by a parameter $\alpha \in [0, 1]$, guaranteeing that this assumption is fulfilled. NK cells have a lifespan of $1/\mu_N$. To the best of our knowledge, there is no evidence that CTLs or healthy NK

cells are able to kill infected NK cells. For this reason, the infected NK cells I_N are assumed to die only due to biological exhaustion and apoptosis induced by the viral infection at the rate μ_{I_N}. As mentioned in section 4.7.1, the lifespan of both healthy and infected NK cells may be altered in vavFLIP$_R$ mice due to the overexpression of c-FLIP. Therefore, the value of the parameters μ_N and μ_{I_N} may be different in the vavFLIP$_R$ case.

5.1.1 Statistical model for the experimental data of the influenza infection

In this work, the statistical model presented in section 3.1.2 was utilized. As presented in the previous chapter and according to the proposed model, the data to be fitted consist of viral load $\mathbf{V_d} \in \mathbb{R}^5$ and total number of NK cells $\mathbf{N_T} \in \mathbb{R}^5$. The dimension of the space is determined by the number of time points to be fitted, i.e. the first 5 days p.i.. The data of observables $\mathbf{y}$ is defined as follows:

$$\mathbf{y} = \begin{bmatrix} \mathbf{V_d} \\ \mathbf{N_T} \end{bmatrix} \tag{5.6}$$

Note that in the data there is no differentiation between healthy and infected NK cells. Therefore, in order to compute the joint observational likelihood, the state variables N and I_N from equation (5.4) and (5.5) are summed up and compared to the total number of NK cells $\mathbf{N_T}$. In this sense, given the state variables

$$\mathbf{x} = \begin{bmatrix} \mathbf{T} \\ \mathbf{I} \\ \mathbf{V} \\ \mathbf{N} \\ \mathbf{I_N} \end{bmatrix} \tag{5.7}$$

where $\mathbf{T}, \mathbf{I}, \mathbf{V}, \mathbf{N}$, and $\mathbf{I_N} \in \mathbb{R}^5$. Given the dimensions of the data of observables $\mathbf{y}$, the linear measurement operator $\mathbf{H}$ is defined as:

$$\begin{pmatrix} \mathbf{0} & \mathbf{0} & \mathcal{I} & \mathbf{0} & \mathbf{0} \\ \mathbf{0} & \mathbf{0} & \mathbf{0} & \mathcal{I} & \mathcal{I} \end{pmatrix} \tag{5.8}$$

where $\mathcal{I} \in \mathbb{R}^{5\times5}$ is the identity matrix and $\mathbf{0} \in \mathbb{R}^{5\times5}$ is the zero matrix. As previously stated, the error ϵ associated with the measurements is assumed to follow a Gaussian distribution with zero mean, i.e. $\mathcal{N}(\mathbf{0}, \mathbf{\Sigma})$.

5.2 Parameter estimation algorithm and numerical methods

In this section, a detailed explanation of the algorithm and numerical tools used in this work is introduced. Afterwards, a simple example shows how this algorithm works in practice.

5.2.1 Parameter estimation algorithm

In order to estimate the parameters governing the dynamics of IAV and immune response, the random walk MCMC method was used. As previously mentioned, this algorithm was selected because it does not present the so-called curse of dimensionality, i.e. the probability of rejection does not increase with the number of dimensions. Moreover, the number of the equations to be solved is smaller than in the case of Hamiltonian Monte Carlo and Metropolis adjusted Langevian Monte Carlo. The goal of this method is to perform a Bayesian inference on the parameters given the available data by considering the uncertainty associated with it. The main advantage of MCMC is to circumvent the practical and occasionally structural non-identifiability problems of the ODEs. Furthermore, additional knowledge from literature can be incorporated in the estimation in the form of priors, reducing the search in the parameter space [121].

Herein, the observations of the dynamical system are assumed to be the true values with an associated Gaussian error from the measurement procedure. Therefore, the data $\mathbf{Y} \in \mathbb{R}^{M\times\tau}$ represents a time series set of measurements of the states $\mathbf{X}(\theta) \in \mathbb{R}^{N\times\tau}$, where θ is the set of parameter, M is the number of the measured states, N is the number of the true states and τ is the discrete time series; $\mathbf{X}(\theta)$ is the numerical solution of a set of differential equations. This numerical solution is obtained from MATLAB solver, ode15s. This solver was chosen so that possible numerical stiffness can be properly solved. Stiffness is a numerical problem that can arise when processes of different rates occur within a dynamical system, affecting the performance of the numerical methods [49]. Given the values of the NK cells and viral load, stiffness may arise during random search in the parameter space.

Then, given a set of measured states $\mathbf{Y}$, the true states $\mathbf{X}$ and the linear measurement operator $\mathbf{H}$, the joint observational likelihood is estimated as follows:

$$\Pr(\mathbf{Y}|\mathbf{H}\,\mathbf{X}(\theta)) = \prod_{m\in M} \mathcal{N}(\mathbf{Y_m}|\mathbf{X_m}(\theta), \sigma^2\mathbf{I}) \tag{5.9}$$

where $\mathbf{Y_m}$ and $\mathbf{X_m}$ are vectors of dimension τ, corresponding to the measurement and computed state m for each observed time, σ^2 is the variance and $\mathbf{I}$ represents the identity matrix.

Given an initial set of parameters θ, in every step, a single candidate parameter $\hat{\theta}_i$

is randomly sampled from a Gaussian transition Kernel $\mathcal{N}(\hat{\theta}_i|\theta_i, k_{ii})$. k_{ii} is diagonal element of the covariance matrix $\mathbf{K}_{\theta\theta}$. $\mathbf{K}_{\theta\theta}$ must be tuned so that the acceptance rate for every parameter lies between 40% and 70%, which in practice is reasonable performance by MCMC [22]. The new set $\hat{\theta}$ is then created with the elements of θ but replacing θ_i by $\hat{\theta}_i$.

The acceptance ratio ζ is calculated as follows:

$$\zeta = \min\left[1, \frac{\Pr(\mathbf{Y}|\mathbf{HX}(\hat{\theta}))\pi(\hat{\theta})}{\Pr(\mathbf{Y}|\mathbf{HX}(\theta))\pi(\theta)}\right] \tag{5.10}$$

where $\pi(\theta)$ represents the prior of θ. Given $u \sim \mathcal{U}[0,1]$, where $\mathcal{U}[0,1]$ is a uniform distribution, the candidate set of parameters $\hat{\theta}$ is accepted if $u < \zeta$. The converged chain will be the distribution of interest.

5.2.2 A simple example

Consider the following system [68]:

$$\frac{dx_1(t)}{dt} = \theta_1 x_1(t) - 7.191 x_2(t) \tag{5.11}$$

$$\tag{5.12}$$

$$\frac{dx_2(t)}{dt} = -\theta_1 x_1(t) - \theta_2 x_2(t) \tag{5.13}$$

where θ_1 and θ_2 are the parameters to be estimated and whose nominal values are -3.5 and 2.1, respectively. The solution of the system can be easily calculated by means of the eigenvalues of the Jacobi matrix, i.e.

$$\begin{pmatrix} \theta_1 & -7.191 \\ -\theta_1 & \theta_2 \end{pmatrix} \tag{5.14}$$

The synthetic experimental data $\mathbf{y}$ was simulated by adding Gaussian noise to the analytical solution $\mathbf{x}$, as presented in figure 5.2.

Given the simplicity of the system, the analytical posterior of the parameters was obtained by solving analytically the system for different parameter sets (see figure 5.3). Starting from different initial parameters, and after applying the burn-it (i.e. the first 5000 iterations are discarded) the posterior observed in figure 5.4 was obtained. The parameter set which produces the highest likelihood and their associated standard deviation were $\{\theta_1 = -3.474 \pm 0.4, \theta_2 = 1.954 \pm 0.3\}$, which agrees with the nominal value presented above. Note how the histogram resembles the analytical posterior, while exploring the parameter space of interest.

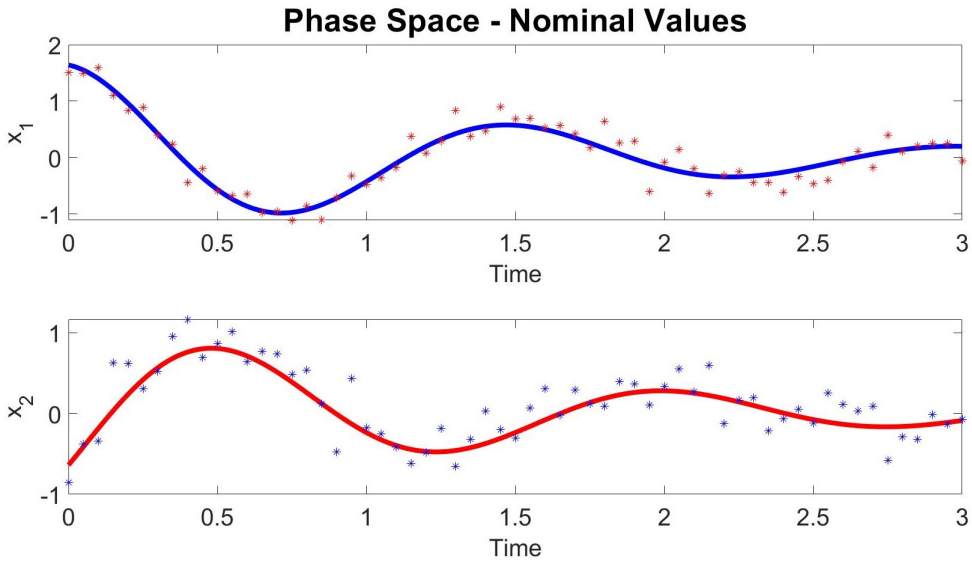

Figure 5.2: Solution of the ODE system and simulated data. The phase space was obtained by solving the ODE system (equation 5.11 and 5.13). The simulated data was created by adding Gaussian noise to the phase space.

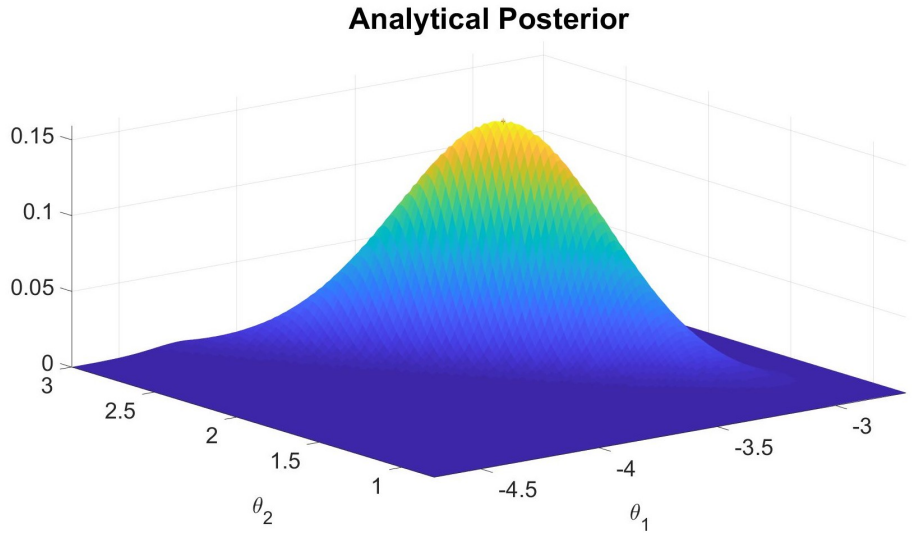

Figure 5.3: Analytical posterior of the parameters. The posterior was obtained by solving the ODE system for different parameter sets.

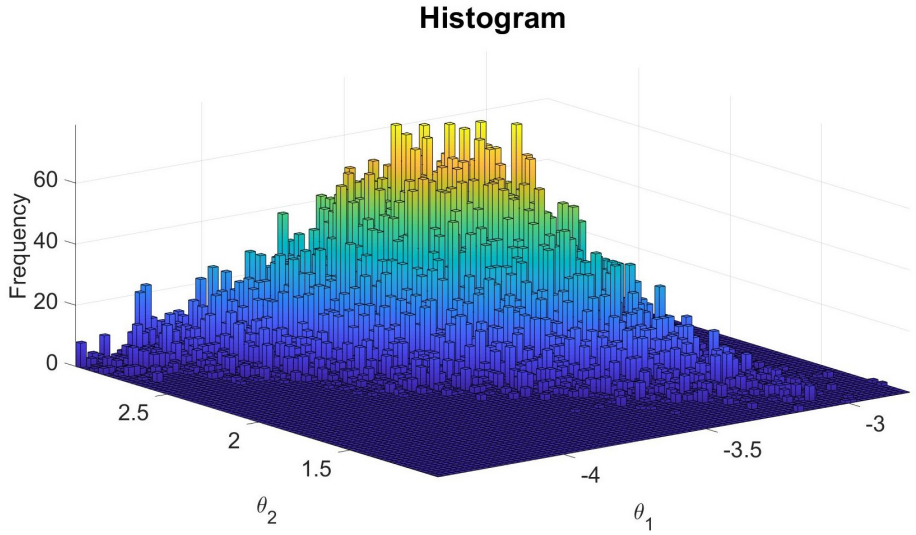

Figure 5.4: Computed posterior of the parameters. This was obtained by applying the MCMC algorithm to the ODE system and the simulated data.

6 Fitting of WT mice data to the proposed IAV infection model

The fitting of the influenza model to the WT data is presented in this chapter. Simplifications regarding the parameter space and assumptions are explained in detail. The parameter set that can explain the measured viral and immune kinetics of WT mice as well as the underlying uncertainty are discussed.

The model was fitted to WT mice data only up to the first 5 days p.i.. The reason behind this approach is to estimate the parameters of the model in a time interval where the antiviral activity of the innate immune response is thought to be dominant and the uncertainties associated with the adaptive immune response are minimal. Nevertheless, the simulations are carried out till day 10 p.i..

6.1 Priors of the parameters

The parameter representing the lifespan of the virus and infected epithelial cells as well as the initial number of epithelial target cells were taken from the literature [9, 8, 106]. This allows a significant reduction in the exploration of the parameter space. Initial number of the infected epithelial cells and infected activated NK cells were assumed to be zero prior to the infection. The initial viral load was informed from the experimental protocol and fine-tuned by the parameter fitting process. The initial number of healthy activated NK cells was at first set to be estimated by the MCMC algorithm. Nonetheless, numerical results (presented below) showed that its impact on the fit is negligible and its estimated value tends to be low. The parameters α and γ are set in the interval $[0, 1]$; for this purpose standard uniform distributions were used. Since there is no prior information regarding the probability distribution of the infection rate δ, killing rate of infected epithelial cells by NK cells ξ, viral production rate ρ_V and NK cell recruitment rate ρ_N, no priors were set for these parameters.

The lifespan of healthy activated NK cells $1/\mu_N$ is not known; however, an upper bound limit was imposed. Zhang et al. stated that a naive NK cell can live between 7 and 10 days [128]. Since activated NK cells are expected to live shorter, the upper bound of their lifespan was constrained to a maximum of 7 days. Thus, a continuous uniform distribution was used as a prior for $1/\mu_N$, corresponding to a lifespan between 0.4 and 7.0 days; this sets the evaluation of $1/\mu_N$ into a biologically relevant range. The lifespan of infected NK cells was assumed to have a similar prior.

As presented below, data fitting process tends to estimate lifespans of healthy and infected NK cells to similar values and a flat distribution for the lifespan of infected NK cells was obtained; this implies that there is not enough information to predict accurately the distribution of this parameter. A better quality of the fit was obtained when healthy and infected NK cells were assumed to have the same lifespan.

6.2 Estimating the initial number of healthy NK cells

Different parameter sets were estimated to fit the WT mice data. In this section, different lifespan for healthy NK cells, $1/\mu_N$ and infected NK cells $1/\mu_{I_N}$ were assumed. Moreover, the initial condition for the healthy activated NK cells, N_0 was set to be estimated. A continuous uniform distribution was used as a prior for N_0, where the lower bound was constrained to zero and the upper bound was the number of total NK cells at day 2 p.i.. The estimated parameters are presented in the table 6.1.

Table 6.1: Estimated parameters and initial conditions of the model, including initial number of healthy NK cells.

Parameter	Value	Units	Reference
δ	$3.89e-09$	$days^{-1}[V]^{-1}$	Estimated
ξ	$1.69e-04$	$days^{-1}[Cells]^{-1}$	Estimated
μ_I	2.0	$days^{-1}$	Fixed [9]
ρ_V	$3.58e+03$	$[V]days^{-1}[Cells]^{-1}$	Estimated
γ	0.953	–	Estimated
μ_V	5.0	$days^{-1}$	Fixed [9, 8]
ρ_N	32.960	$days^{-1}$	Estimated
α	0.889	–	Estimated
μ_N	0.639	$days^{-1}$	Estimated
μ_{I_N}	1.392	$days^{-1}$	Estimated
T_0	$2.38e+06$	$[Cells]$	Fixed [106]
I_0	0.0	$[Cells]$	Fixed
V_0	$6.049e+04$	$[V]$	Estimated
N_0	27.357	$[Cells]$	Estimated
I_{N_0}	0.0	$[Cells]$	Fixed

Figures 6.1 and 6.2 show the data as well as the fitting of the viral load and the total number of NK cells for this trial. The fitting procedure was performed up to day 5 p.i.; nevertheless, simulation was carried out until day 10 p.i.. A persistent state of the infection can be observed in the figure 6.1 after day 5 p.i., since no viral clearance occurs. Due to the fact that the model is not able to eliminate the virus, additional mechanisms, such as the adaptive immune system, are required.

The predicted higher viral load results in more infected epithelial cells; according

to the mechanism imposed in the model, a higher number of infected epithelial cells produces an increase in the recruitment of NK cells. This explains the higher number of NK cells observed in figure 6.2 after day 5 p.i.. The posterior distribution of the initial number of healthy NK cells N_0 is presented in figure 6.3. This figure was obtained by the sampling procedure performed by the MCMC. The estimation for the initial number of healthy NK cells tends to low values. This result seems to be logical as lower values of activated healthy NK cells are expected when no infection takes place. The most repeated value during the space exploration was $N_0 = 100$.

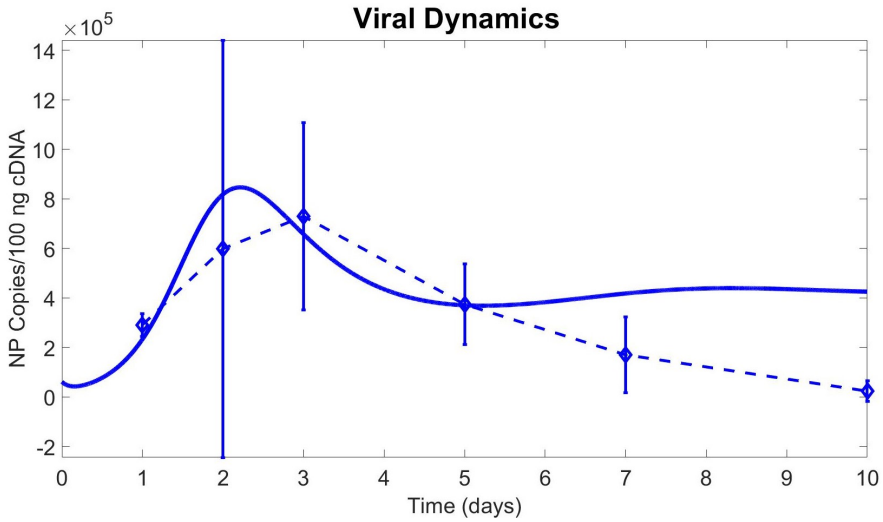

Figure 6.1: Time evolution of the viral load. The parameters were estimated based on the first 5 days of infection, and simulated up to day 10 p.i..

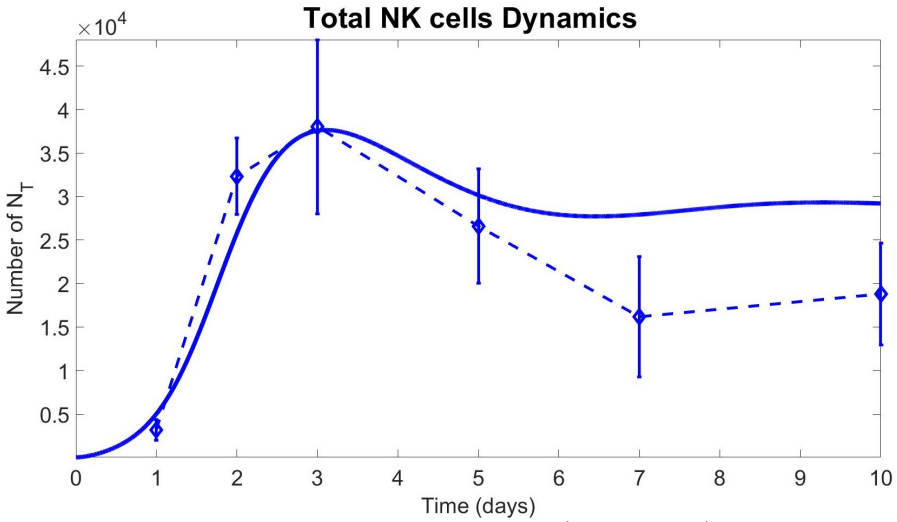

Figure 6.2: Time evolution of the of total NK cells (N and I_N). The parameters were estimated based on the first 5 days of infection, and simulated up to day 10 p.i..

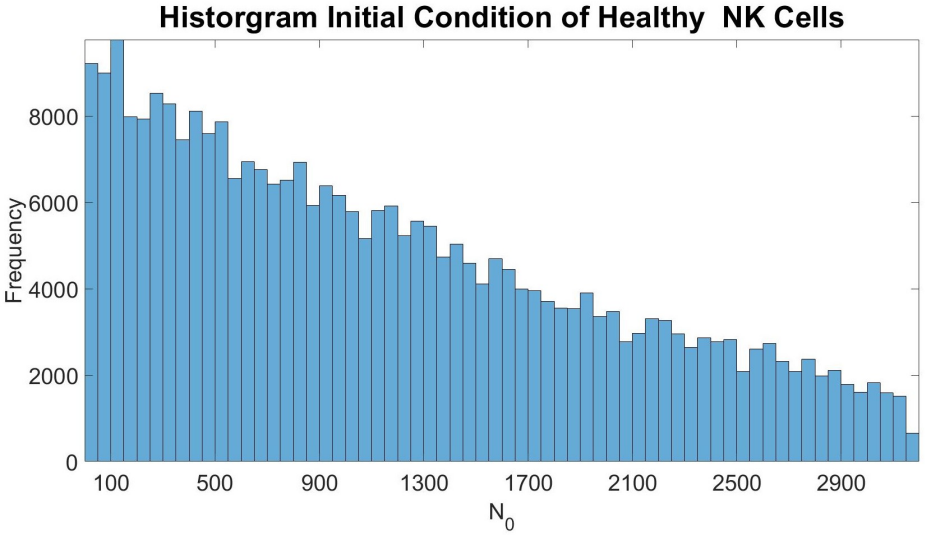

Figure 6.3: Posterior distribution of initial number healthy NK cells. The histogram was obtained by the parameter space exploration of the MCMC algorithm.

6.3 Fixing the initial number of healthy NK cells to 100

As observed in figure 6.3, the most frequent estimated values for the initial amount of healthy NK cells are in the neighbourhood of 100; therefore, in order to simplify the parameter space search, N_0 was set to 100 *cells*. The parameter estimation was carried out by considering different death rates for healthy and infected NK cells, μ_N and μ_{I_N} respectively. The results are presented in table 6.2.

The fitting of viral load and total number of NK cells are presented in figures 6.4 and 6.5. The steady state of the viral load produces a constant number of infected epithelial cells which keep the recruitment of NK cells at a steady level, as observed in figure 6.5.

The sampling of the MCMC produced a relatively flat posterior of the death rate of infected NK cells μ_{I_N}, as presented in figure 6.6. This result indicates the posterior distribution of this parameter cannot be estimated from data.

Table 6.2: Estimated parameters and initial conditions of the model with a fixed initial number of healthy NK cells.

Parameter	Value	Units	Reference
δ	$6.988e-08$	$days^{-1}[V]^{-1}$	Estimated
ξ	$1.447e-04$	$days^{-1}[Cells]^{-1}$	Estimated
μ_I	2.0	$days^{-1}$	Fixed [9]
ρ_V	$1.915e+02$	$[V]days^{-1}[Cells]^{-1}$	Estimated
γ	0.923	–	Estimated
μ_V	5.0	$days^{-1}$	Fixed [9, 8]
ρ_N	1.809	$days^{-1}$	Estimated
α	0.897	–	Estimated
μ_N	0.692	$days^{-1}$	Estimated
μ_{I_N}	1.172	$days^{-1}$	Estimated
T_0	$2.38e+06$	$[Cells]$	Fixed [106]
I_0	0.0	$[Cells]$	Fixed
V_0	$6.928e+04$	$[V]$	Estimated
N_0	100	$[Cells]$	Estimated
I_{N_0}	0.0	$[Cells]$	Fixed

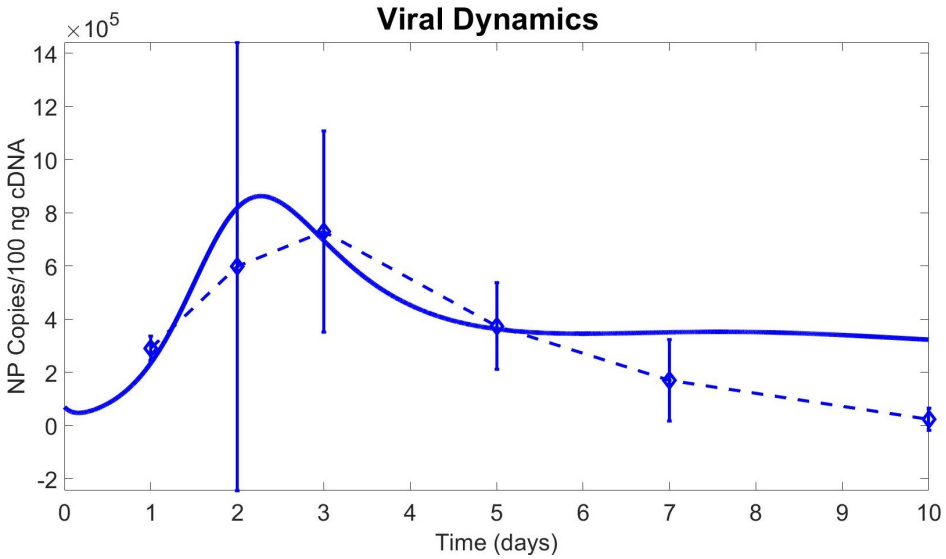

Figure 6.4: Time evolution of the viral load. The parameters were estimated based on the first 5 days of infection, and simulated up to day 10 p.i..

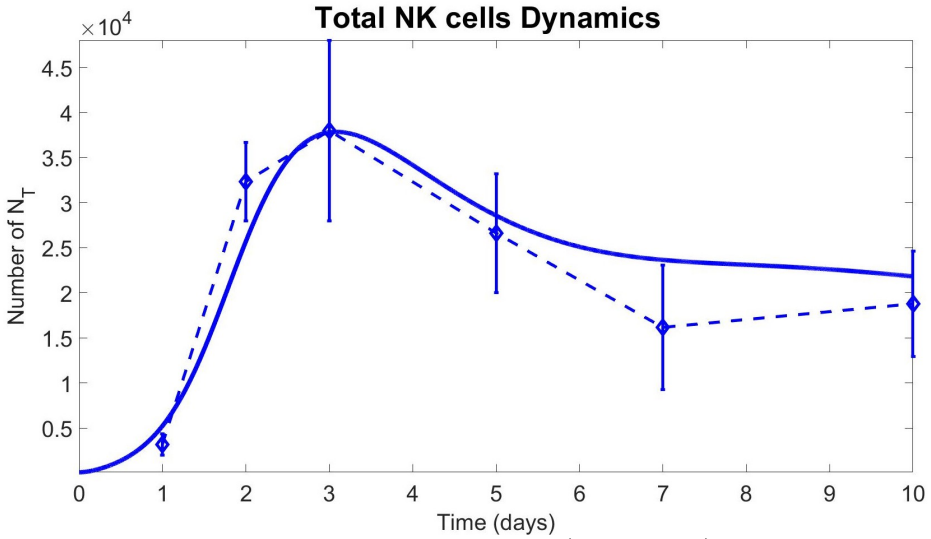

Figure 6.5: Time evolution of the of total NK cells (N and I_N).The parameters were estimated based on the first 5 days of infection, and simulated up to day 10 p.i..

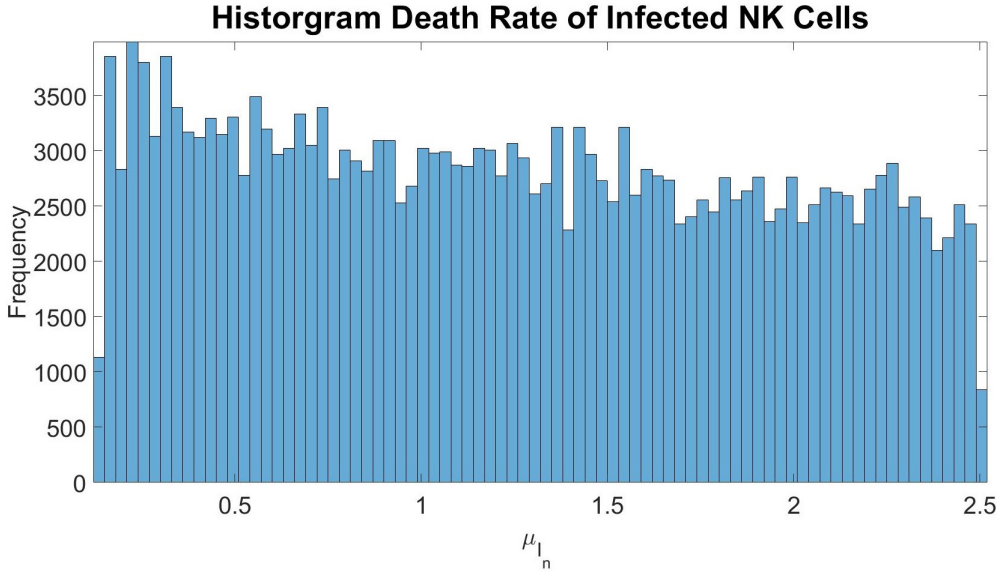

Figure 6.6: Posterior distribution of death rate of infected NK cells with a fixed initial number of healthy NK cells. The histogram was obtained by the parameter space exploration of the MCMC algorithm.

6.4 Assuming an equal lifespan for healthy and infected NK cells

To cope with the lack of information to estimate the posterior of μ_{I_N} (see figure 6.6), the lifespan of healthy and infected NK cells were assumed to be equal. Moreover, the initial number of healthy NK cells was fixed to 100 *cells*. This reduces the

parameter space exploration. The parameters which produce the highest likelihood by the MCMC algorithm are introduced in table 6.3. The results of the simulation and the fitting are presented in figures 6.7 and 6.8.

Table 6.3: Estimated parameters and initial conditions of the model assuming equal lifespan for healthy and infected NK cells and setting $N_0 = 100$ *cells*.

Parameter	Value	Units	Reference
δ	$1.318e-07$	$days^{-1}[V]^{-1}$	Estimated
ξ	$1.415e-04$	$days^{-1}[Cells]^{-1}$	Estimated
μ_I	2.0	$days^{-1}$	Fixed [9]
ρ_V	$1.046e+02$	$[V]days^{-1}[Cells]^{-1}$	Estimated
γ	0.936	–	Estimated
μ_V	5.0	$days^{-1}$	Fixed [9, 8]
ρ_N	1.051	$days^{-1}$	Estimated
α	0.914	–	Estimated
μ_N	0.770	$days^{-1}$	Estimated
T_0	$2.38e+06$	$[Cells]$	Fixed [106]
I_0	0.0	$[Cells]$	Fixed
V_0	$5.97e+04$	$[V]$	Estimated
N_0	$1.00e+02$	$[Cells]$	Fixed
I_{N_0}	0.0	$[Cells]$	Fixed

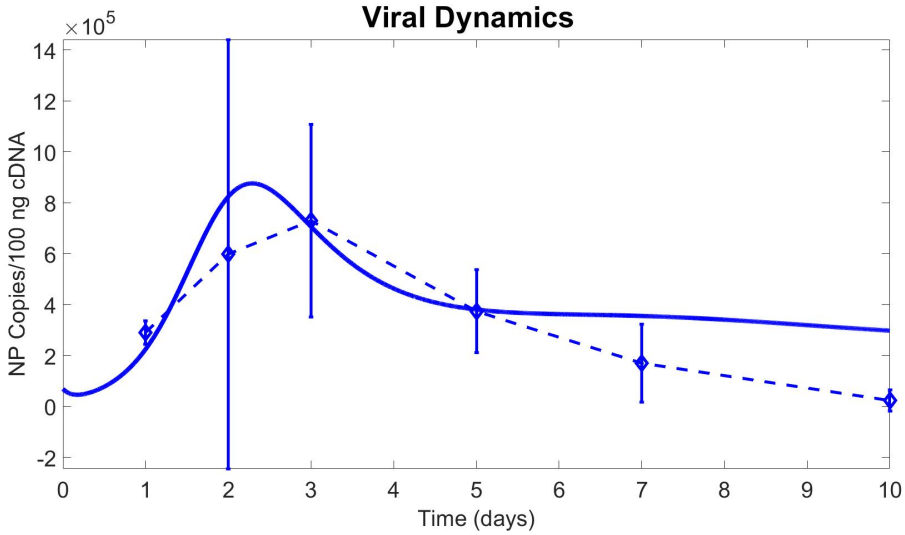

Figure 6.7: Time evolution of the viral load. The parameters were estimated based on the first 5 days of infection, and simulated up to day 10 p.i..

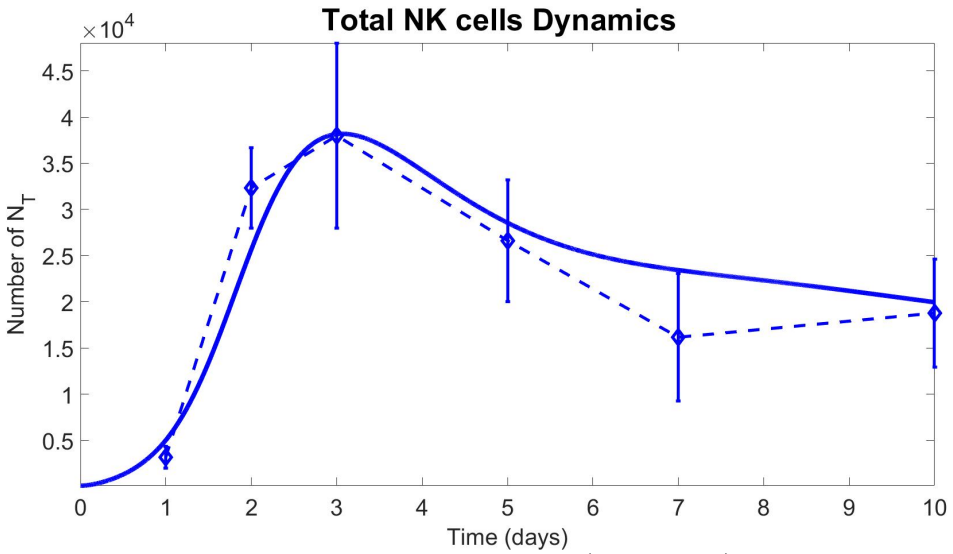

Figure 6.8: Time evolution of the of total NK cells (N and I_N).The parameters were estimated based on the first 5 days of infection, and simulated up to day 10 p.i..

6.5 Comparison of fittings to WT data

In order to select the best fitting to WT data, a comparison between the three approaches presented above was carried out by analyzing the joint observational likelihood produced by the MCMC estimation. Moreover, the AIC was also computed. The set of parameters with the highest likelihood and lowest AIC is the one that explains the data with the smallest complexity given the proposed model. The results are presented in table 6.4.

Table 6.4: Comparison of observational likelihoods and AIC of the fittings to WT data

Assumptions	Likelihood	AICc
Estimation of the initial number of healthy NK cells.	$5.2650e-06$	44.322
Fixed initial number of healthy NK cells.	$5.3631e-06$	42.271
Fixed initial number of healthy NK cells and equal lifespan for healthy and infected NK cells.	$\mathbf{5.4210e-06}$	**40.250**

According to the table 6.4, the highest likelihood and the lowest AIC are obtained by setting the initial number of healthy NK cells to 100 and by assuming an identical death rate for healthy and infected NK cells. Therefore, these assumptions guarantee a more accurate description of the data. This result justifies the usage of this parameter set in the subsequent chapter.

6.6 State variables and dynamical terms of the best fit to the WT data

6.6.1 State Variables

In this section, the state variables obtained from the simulation of the model with the parameters presented in table 6.3 are introduced. These parameters were obtained by fitting the WT data, fixing $N_0 = 100$ *cells* and assuming an equal death rate for healthy and infected NK cells. The dynamics of target (T) and infected epithelial cells (I), as well as healthy (N) and infected NK cells (I_N) are presented in figure 6.9.

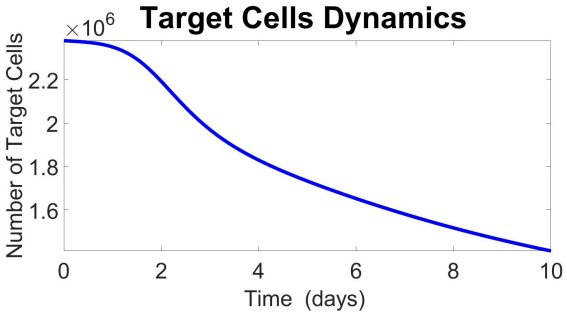

(a) Time evolution of the epithelial cells T

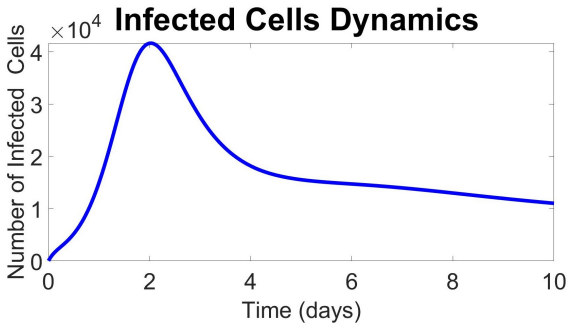

(b) Time evolution of the infected epithelial cells I

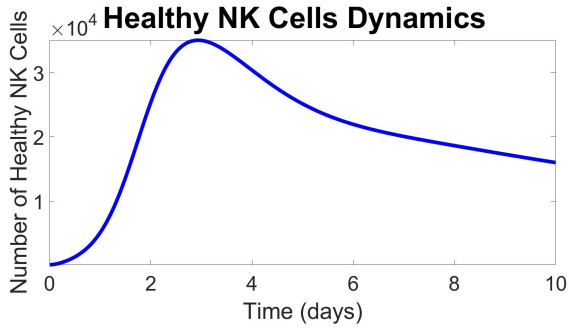

(c) Time evolution of the healthy NK cells N

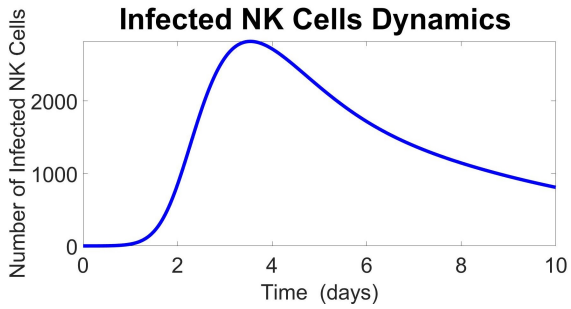

(d) Time evolution of the infected NK cells I_N

Figure 6.9: Time evolution of the state variables. The parameters were estimated based on the first 5 days of infection, and simulated up to day 10 p.i ..

The lack of viral clearance predicted by the simulation (figure 6.7) produces a steady number of infected epithelial cells as observed in figure 6.9b, which in turn, recruit more NK cells. Consequently, NK cells get also infected, achieving a peak of infection at day 4 p.i. and then reaching a temporary plateau, i.e. quasi steady state. Since the available target epithelial cells are limited and no recovery process is considered in the model, a decrease in the curves can be expected for a larger time interval. Nonetheless, in the considered time gap of the simulation, i.e. from day 0

to 10 p.i., the quasi steady state assumption is valid. Additionally, simulation results suggest that NK cells are not infected during the first 1.5 *days*; this can be observed in figure 6.9d, as there is a delay in the rising phase of the infected NK cells.

Interestingly, the damage of epithelial target cells (ratio of dead epithelial cells over initial amount) at the 10 p.i. is 40%. Around day 5.5 p.i., when the adaptive immune response starts to be detected in the site of infection, the estimated damage was 30%. Both results agree with previous studies [8, 16].

6.6.2 Dynamical terms of the ODE system

To further evaluate the behaviour of the IAV infection model, the terms of the right hand side (r.h.s.) of the ODE system were independently analysed. The evolution in time of these terms are introduced in figures 6.10 and 6.11.

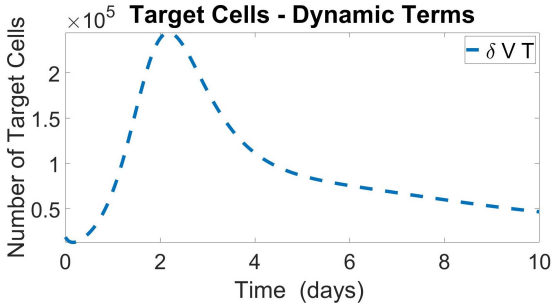

(a) Components of the r.h.s. of the Target cell dynamics

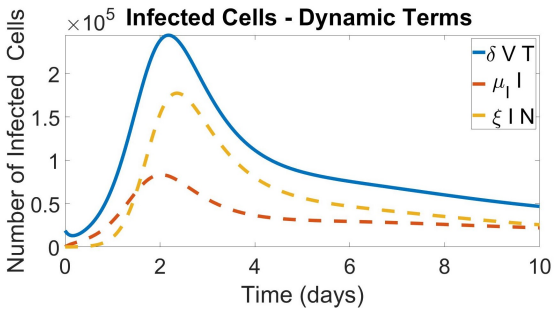

(b) Components of the r.h.s. of the Infected cell dynamics

Figure 6.10: Terms of the r.h.s. of Target cell dynamics (Eq. 5.1) and Infected cell dynamics (Eq. 5.2).

As observed in figure 6.10b, the term ξIN, which represents the killing of infected epithelial cells by healthy NK cells, exhibits a delay of 1 day due to the absence of NK cells at the beginning of the IAV infection. However, the contribution of this term in the infected epithelial cell dynamics increases rapidly and after day 2, it overcomes the contribution of the unspecified death rate of infected epithelial cells, i.e. $\mu_I I$. Note that as the infection progresses, these two terms tend to similar values.

The terms of the viral dynamics are presented in figure 6.11a. Note that the curve corresponding to the term $\gamma\rho_V I_N$ is significantly less prominent than the other curves, implying that viral replication within infected NK cells does not play a critical role in the overall viral dynamics. Since the parameter estimation procedure suggests that

viral replication within epithelial and NK cells are similar, the minor impact of the term $\gamma\rho_V I_N$ is attributed to the small population of infected NK cells, in comparison to infected epithelial cell numbers. The minor contribution of the term $\gamma\rho_V I_N$ explains why the fitting of viral dynamics in previous research has been accurate even though the infected NK cell dynamics has not been included in those models.

In figure 6.11b, the terms of the healthy NK cell dynamics are introduced. Note that the influence of the infection rate of NK cells ($\delta\alpha NV$) to the overall NK cell dynamics is negligible. Since the infection rate is proportional to the size of the NK cell population, it can be inferred that the minor contribution of the term $\delta\alpha NV$ is related to the small size of the NK cell population. Finally, a delay in the terms of the infected NK cell dynamics is observed in figure 6.11c, which, as previously mentioned, occurs due to the reduced number of healthy NK cells at early stages of the IAV infection.

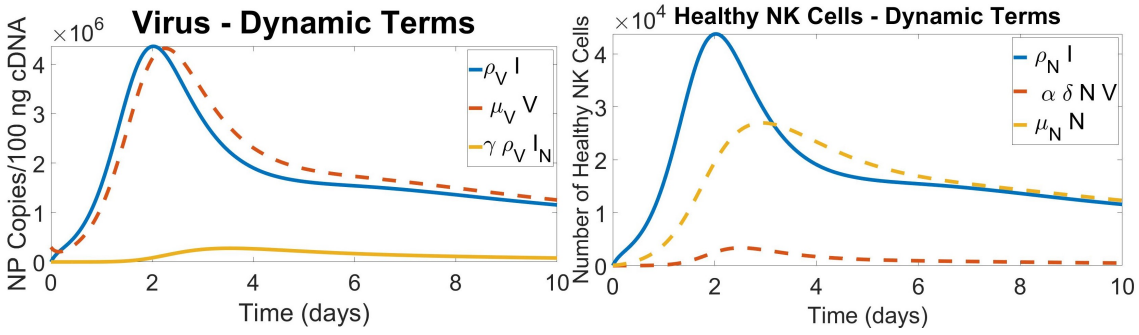

(a) Components of the r.h.s. of the Viral dynamics

(b) Components of the r.h.s. of the NK cell dynamics

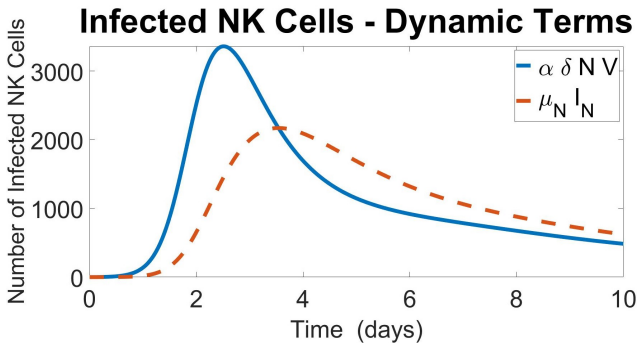

(c) Components of the r.h.s. of the infected NK cell dynamics

Figure 6.11: Terms of the r.h.s. of Viral dynamics (Eq. 5.3), Healthy and Infected NK cell dynamics (Eq. 5.4 and 5.5, respectively).

6.7 Posteriors and correlations of the estimated parameters for WT data

The posterior distributions of the parameters are presented in figures 6.12 and 6.13. Such results were obtained from the parameter space exploration performed by the MCMC algorithm. None of the posteriors of the parameters are conventional distributions, which reveals a complicated parameter space.

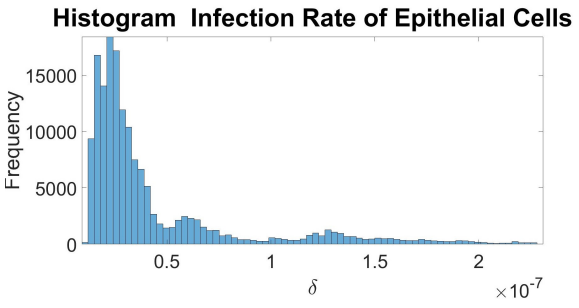

(a) Posterior distribution of infection rate of epithelial cells, δ.

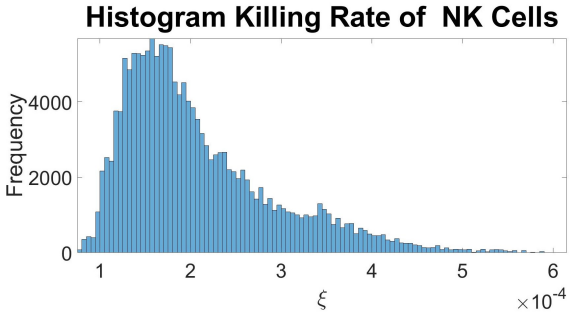

(b) Posterior distribution of killing rate of infected epithelial cells by NK cells, ξ.

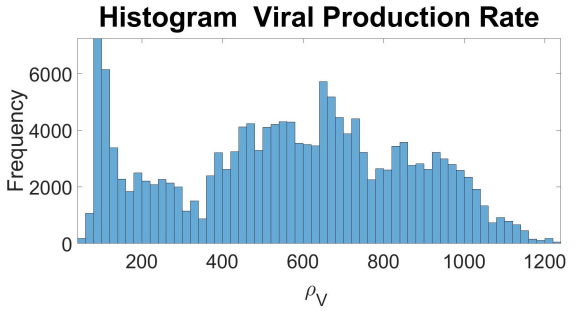

(c) Posterior distribution of viral production by infected epithelial cells, ρ_V.

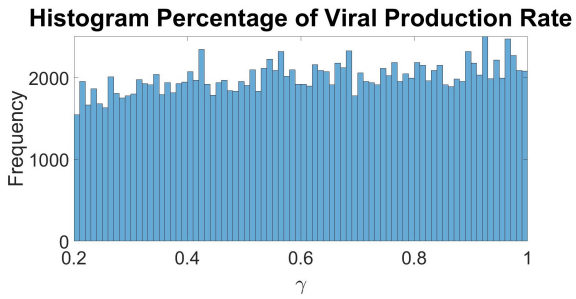

(d) Posterior distribution of percentage of viral production by NK Cells, γ.

Figure 6.12: Posterior distributions of the parameters δ, ξ, ρ_V and γ

The most interesting results are observed in the parameters γ and α, presented in figures 6.12d and 6.13b, respectively. Both of these distributions are flat, implying that the effect of their values to the outcome of the fitting is negligible. Moreover, these results suggest that the available data is insufficient for an accurate estimation of their distributions. Therefore, additional data and mechanisms regarding NK cell dynamics are required. For instance, the parameter α may depend on spatial movement of NK cells or further mechanism of infection such as contact with infected epithelial cells, which are not explicitly included in the model. The values of γ and α on the maximum likelihood (as presented in table 6.3) may indicate that infection rate and viral production rate of NK cells are similar to epithelial cells. Further experiments to determine viral production and infection rate by NK cells are

necessary.

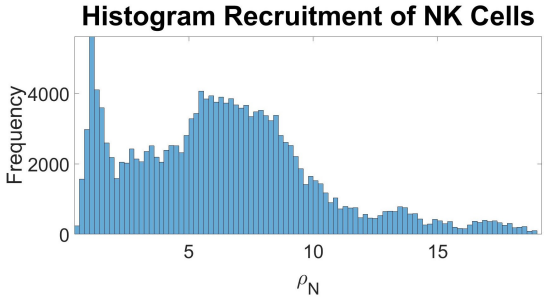

(a) Posterior distribution of recruitment of NK cells, ρ_N.

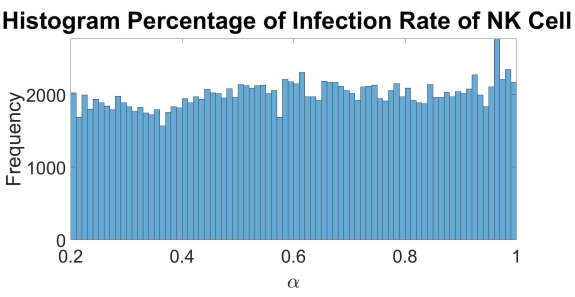

(b) Posterior distribution of percentage of infection rate of NK cells, α.

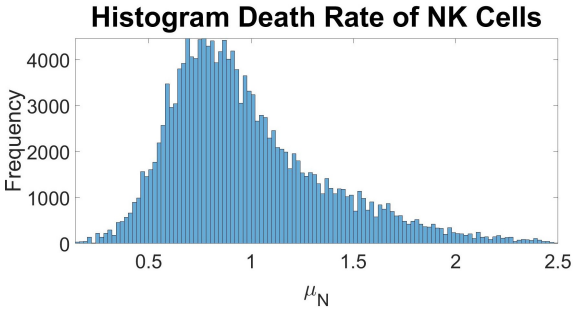

(c) Posterior distribution of death rate of NK cells, μ_N.

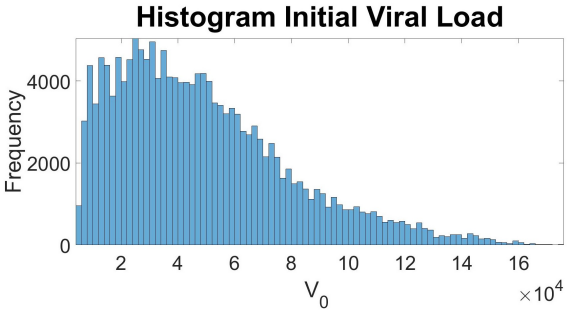

(d) Posterior distribution of initial viral load, V_0.

Figure 6.13: Posterior distributions of the parameters ρ_N, α, μ_N and V_o

In order to evaluate possible relationships between the parameters a correlation analysis was carried out. This will highlight possible limitations in the predicted distributions. The most important results are presented in figure 6.14.

A negative non-linear correlation was observed between δ and ρ_V, representing infection rate of target epithelial cells and viral production within infected epithelial cells (see figure 6.14a). This correlation may occur due to insufficient observables, as there is no independent information regarding target or infected epithelial cell dynamics; thus, in order to fit the viral load data, these two parameters compensate one another. Furthermore, a positive linear correlation between the recruitment rate of NK cells ρ_N and viral production rate by the infected epithelial cells ρ_V was observed (see figure 6.14b). Note that this type of correlation may arise due to the structure of the model, as an increase in the viral production, requires an increase in the number of NK cells to control the infection. Finally, the previous described correlations produced an additional one between δ and ρ_N, presented in figure 6.14c.

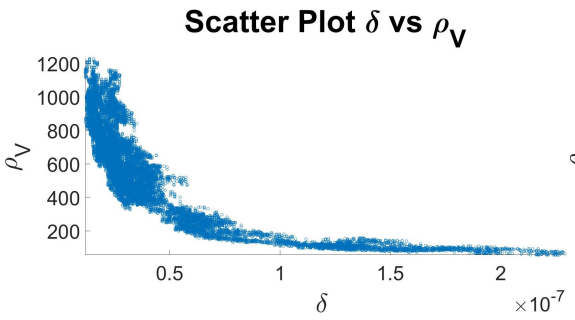

(a) Scatter plot of infection rate of epithelial cells, δ vs viral production rate by infected epithelial cells, ρ_V.

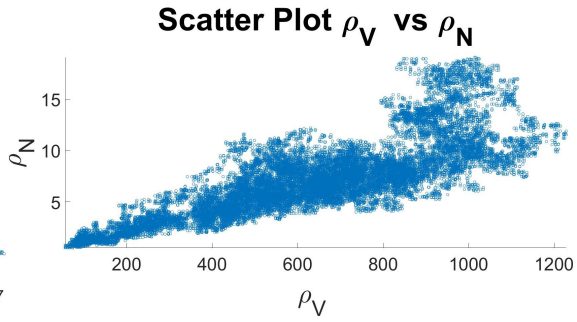

(b) Scatter plot viral production rate by infected epithelial cells, ρ_V vs NK cells recruitment rate, ρ_N.

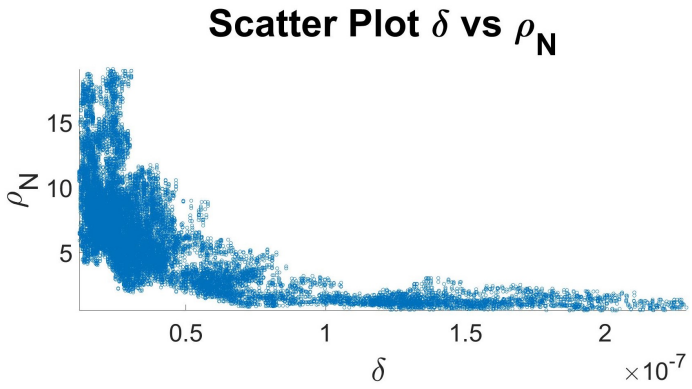

(c) Scatter plot infection rate of epithelial cells, δ vs NK cells recruitment rate, ρ_N.

Figure 6.14: Correlation analysis of the parameters

6.8 Adaptive immune response role in IAV infection model

In order to observe the effect of the adaptive immune response in the IAV model, a killing rate of infected epithelial cells by CTLs (C) was included in the right hand side of the equation 5.2, i.e.

$$\dot{I} = \delta VT - \xi NI - \mu_I I - \kappa \mathbf{IC} \tag{6.1}$$

where, κ represents the killing rate of infected epithelial cells by CTLs. Since the data presented in section 4.6 does not correspond to CTLs accumulation in the site of infection, the CTL kinetics was emulated in the model by a Hill equation (see figure 6.15). This guarantees that CTLs arrive at the site of the infection after day 5 p.i. and peak after day 7 p. i., in agreement with the literature [110, 17].

The simulation was carried out up to day 10 p.i. with the parameters presented in the table 6.3 , while the parameter κ was the only one to be fitted. The MCMC

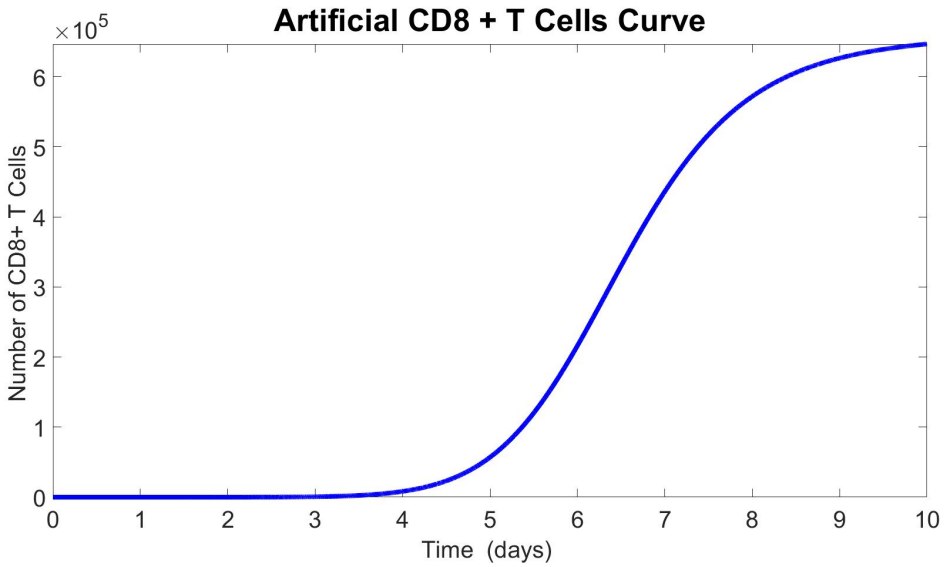

Figure 6.15: Assumed curve of CTL kinetics from Hill equation

algorithm estimated $\kappa = 3.745 \times 10^{-06}[days^{-1}cells^{-1}]$. The result of the fitting are presented in figures 6.16 and 6.17.

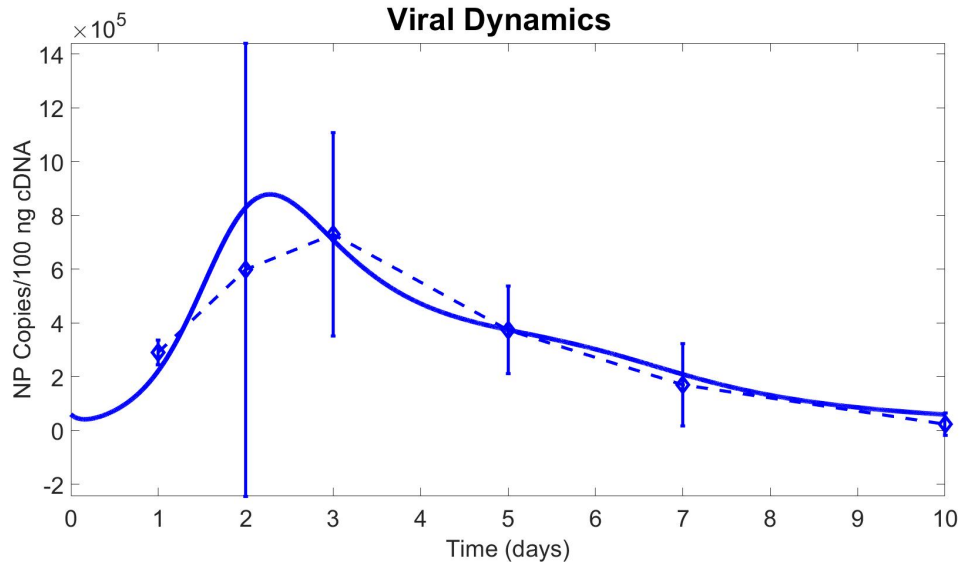

Figure 6.16: Time evolution of the viral load V. The killing rate κ was estimated up to day 10 p.i..

An improvement in the fitting of viral load after day 5 p.i. was observed. However, fitting quality of the NK cells at day 10 p.i. worsened. This may be due to the simplified model used in this study. NK cells are recruited by IFN type I; therefore, the increment in the recruitment at day 10 p.i., in comparison with day 7 p.i., may be related to the second peak observed in the IFN-α data (figure 4.9). Nonetheless,

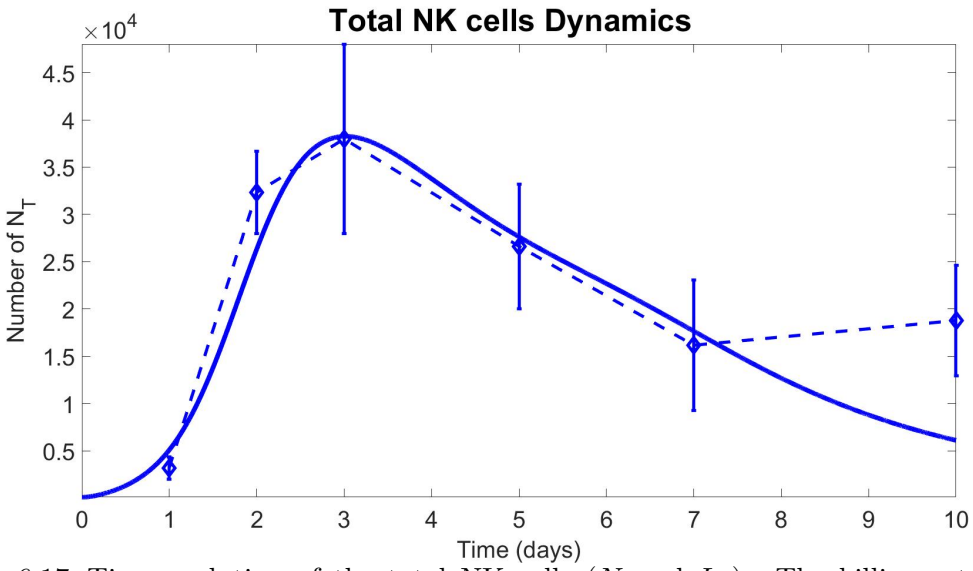

Figure 6.17: Time evolution of the total NK cells (N and I_N). The killing rate κ was estimated up to day 10 p.i..

incorporating the IFN dynamics is a rather complicated task as there is no explanation in the literature that can account for its second peak at day 7 p.i.. Nevertheless, dendritic cell dynamics may explain the increases of IFN-α at day 7 p.i..

Following influenza infections, dendritic cells migrate from the lungs to the lymph nodes, where the antigen is presented to the naive CTLs. Afterwards, dendritic cells accumulated into the lungs without any further migration [60]. Given the fact that dendritic cells are one of the main sources of IFN-α, one can infer that this dendritic accumulation in the lung may be the reason for the second peak of IFN-α in the lavage. However, as previously stated, there is no evidence that can support this hypothesis.

6.9 Summary

In this chapter, the IAV model presented in the previous chapter was fitted to the WT data. The highest joint observational likelihood was obtained by assuming that healthy and infected NK cells have an equal lifespan. By such assumption, the mathematical model was able to represent the experimental data more accurately. According to the parameter fitting results, infection and viral replication rate within NK cells are similar to the epithelial cells. However, the data used in this study was insufficient to accurately determine the distribution of those parameters. Furthermore, the simulation results showed a persistent state of the infection after day 5 p.i., which is associated with the absence of adaptive immune response in the model. The predicted damage (ratio of dead epithelial cells over initial amount) obtained by the simulation was 30%, which is consistent with the literature [16, 8].

7 Analysis of c-FLIP$_R$ cell death modulation on NK cells

The experimental data presented in chapter 4 suggest that, during the IAV infection, the differences in the viral load between vavFLIP$_R$ (which express murine c-FLIP$_R$ in all hematopoietic cells) and WT mice are related to the NK cell kinetics. Therefore, in this chapter, changes in parameters associated with NK cell dynamics are proposed to be responsible for the altered viral dynamics. According to Tafrishi [107] and the experimental data at the intracellular level, NK cells of infected vavFLIP$_R$ mice present a lower frequency of active caspase 3 as well as a lower degranulation. From these observations, three basic hypotheses were inferred herein. First of all, a lower level of active caspase 3 indicates that NK cells may resist apoptosis (see section 4.7.1). Hence, the death rate for both healthy and infected NK cells might be altered. Herein, the assigned value for the death rate of infected NK cells μ_{I_N} is the same as the death rate of healthy NK cells, μ_N, unless otherwise stated. Secondly, different studies have shown that activation of caspase-3 is essential for an effective viral replication [124, 123, 7], which means that a different viral production rate within infected NK cells may occur as well (see section 4.7.1). Therefore, a new estimation of the viral production rate of the infected NK cells γ might be required. Finally, since a lower degranulation was detected in the NK cells of vavFLIP$_R$ mice, a different killing rate ξ may be required as well (see section 4.7.2).

Moreover, there is a possibility that the intracellular characteristics exhibited by NK cells in vavFLIP$_R$ mice may affect IAV kinetics in more than one way. For this reason, combinations of the basic hypotheses are also tested. In this chapter, the analysis of the basic hypotheses and their combination is presented.

For the simulation in this chapter, the initial conditions were assumed to be the same as in the previous chapter, since, as stated in chapter 4, under steady state the lymphocyte population is similar in both mice. Moreover, the viral load supplied intranasally to vavFLIP$_R$ and WT littermates was the same.

7.1 Basic hypotheses tested to fit vavFLIP$_R$ mice data

As previously mentioned, during the IAV infection, the differences between vavFLIP$_R$ and WT mice are associated with the NK cell intracellular characteristics, i.e. lower levels of active caspase 3 and lower degranulation. Thus, different hypotheses that

can account for alterations related to those findings are evaluated. For this purpose, the parameters derived in the previous chapter are used and only the parameters corresponding to the respective hypothesis are estimated. The proposed hypotheses were analyzed by investigating how well their corresponding mathematical representation fits to the experimental data. The accuracy of the hypothesis is evaluated by the observational likelihood. The basic hypotheses are presented in this section. Subsequently, combinations of the hypotheses are presented

7.1.1 Lower expression levels of active caspase 3 may affect the lifespan of healthy and infected NK cells in vavFLIP$_R$

Lifespan of healthy NK cells in vavFLIP$_R$ mice

According to the experimental data [107], NK cells of infected vavFLIP$_R$ mice express a lower frequency of active caspase 3, indicating that they may resist apoptosis. Hence, changes in the death rate of healthy NK cells μ_N were first assumed. The parameter μ_N was re-estimated by the MCMC algorithm to a value of 1.010 $days^{-1}$. This value is higher compared to the results for the WT fitting, which may indicate that healthy NK cells do not resist apoptosis. The fitting is presented in figure 7.1. Note that the qualitative behavior of the NK cell dynamics is accurately emulated, although slightly underestimated. However, the fitting of the viral dynamics could not fit the data at day 3 and 5 p.i.. Therefore, changes in the lifespan of healthy NK cells alone cannot explain the vavFLIP$_R$ data.

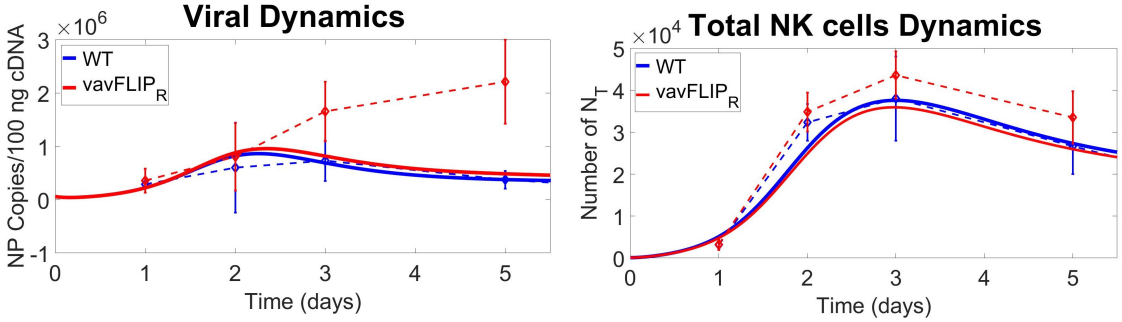

(a) Viral dynamics of vavFLIP$_R$ mice

(b) Total NK cell dynamics of vavFLIP$_R$

Figure 7.1: Fitting to vavFLIP$_R$ data assuming that lower frequency of active caspase 3 affects the lifespan of healthy NK cells. Data points up to day 5 p.i. are considered for the parameter fitting.

Lifespan of infected NK cells in vavFLIP$_R$ mice

Lower frequency of active caspase 3 may also affect the lifespan of infected NK cells. Therefore, the parameter μ_{I_N} was set free in the MCMC algorithm and re-estimated in order to fit the vavFLIP$_R$ data. The parameter estimated value was

$\mu_{I_N} = 0.0100\ days^{-1}$. This estimation is significantly lower than the one obtained in the WT case and may be related to the viral load data 4.2. Since there is no additional source of viral production, the algorithm tries to adjust the lifespan of infected NK cells to greater values, so that their viral production is sustained for a longer period of time; thus, the viral load data can be better adjusted.

The results are presented in figure 7.2. Note that the fitting procedure, as in the previous case (7.1a), does not satisfy the viral data reported in chapter 4. Total NK cell dynamics is fitted within the intervals of the standard deviation of the data, although NK cells are slightly underestimated at day 2 p.i.. Additionally, after day 4 p.i., a steady state is observed in the viral dynamics as well as in the NK cell dynamics. These results suggest that changes in death rate of infected NK cells cannot explain the vavFLIP$_R$ data.

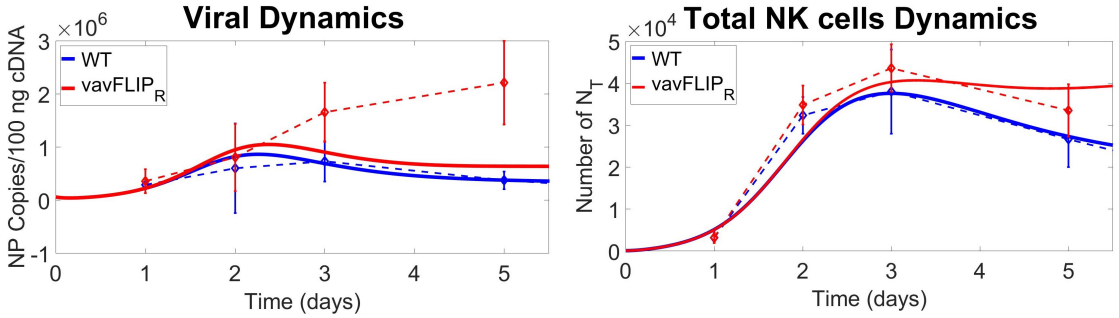

(a) Viral dynamics of vavFLIP$_R$ mice

(b) Total NK cell dynamics of vavFLIP$_R$ mice

Figure 7.2: Fitting to vavFLIP$_R$ data assuming that lower frequency of active caspase 3 affects the lifespan of infected NK cells. Data points up to day 5 p.i. are considered for the parameter fitting.

7.1.2 Lower frequency of active caspase 3 may improve the viral production within infected NK cells in vavFLIP$_R$ mice

Apoptosis has been reported to be deeply related to different aspects of IAV infection [130, 127, 124]. Walter et al. reported that caspase 3 plays a critical role in the replication of influenza virus within cells [123]. Based on this observation, the parameter γ, which is a factor that is associated with viral production of infected NK cells, was re-estimated by the MCMC algorithm. This allowed to evaluate a possible impact of lower frequency of active caspase 3 in viral replication within infected NK cells. The parameter was estimated to $\gamma = 5.040$, which is significantly higher compared to the results obtained for WT. The results are presented in figure 7.3. Note that the qualitative behavior of the viral dynamics resembles the experimental results in a more accurate manner than in the previous cases. Nonetheless, the fitting of total NK cells worsened with a highly overestimation at day 5 p.i.. The obtained results

may indicate that a higher viral production by infected NK cells is needed for a better fitting of the viral load data.

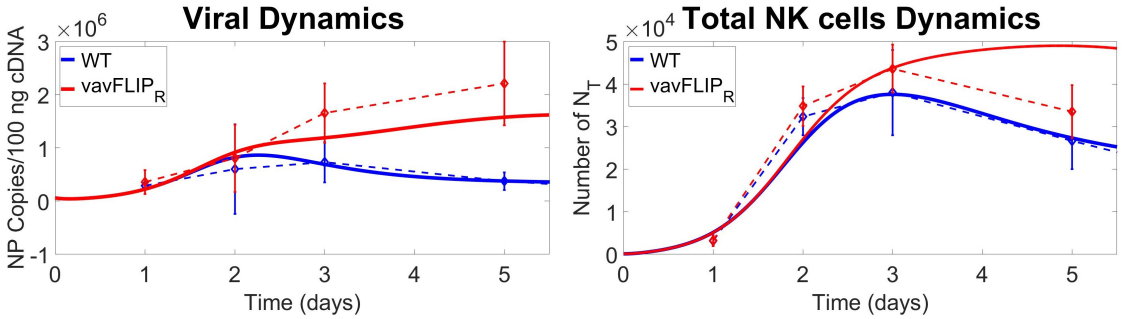

(a) Viral dynamics of vavFLIP$_R$ mice (b) Total NK cell dynamics of vavFLIP$_R$ mice

Figure 7.3: Fitting to vavFLIP$_R$ data assuming that lower frequency of active caspase 3 improves the viral production within infected NK cells. Data points up to day 5 p.i. are considered for the parameter fitting.

7.1.3 Impaired degranulation of NK cells may be linked to a different killing rate in vavFLIP$_R$ mice

According to Tafrishi [107], a lower cytotoxicity of NK cells was detected at day 7 p.i. in infected vavFLIP$_R$ mice (section 4.4.1). Therefore, the parameter ξ was re-estimated by the MCMC algorithm in order to assess possible changes of the killing rate of healthy NK cells as the cause for the vavFLIP$_R$ data. Such changes may be related to c-FLIP alteration in functionality of NK cells [107]. The fitting results are introduced in figure 7.4. The parameter was estimated to $\xi = 1.077 \times 10^{-04}\ days^{-1}[cells]^{-1}$, a relatively smaller number in comparison to the estimation for the WT mice. Note that the NK cell dynamics was accurately fitted. Nonetheless, as in the first two cases, the viral dynamics behavior did not fit the data at day 3 and 5 p.i..

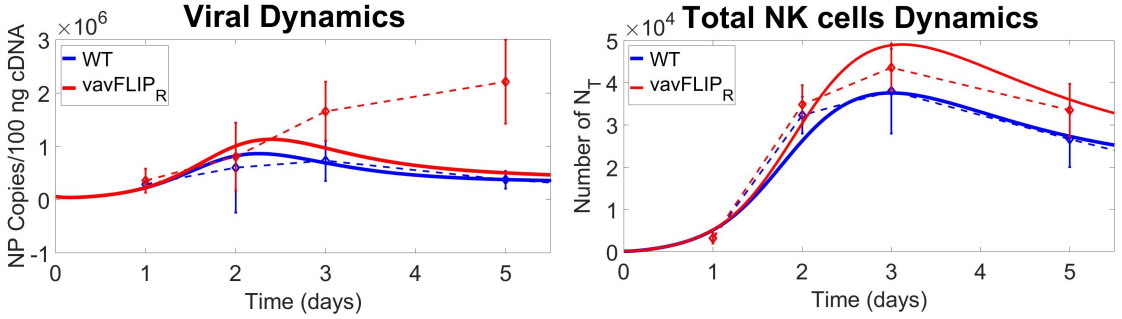

(a) Viral dynamics of vavFLIP$_R$ mice (b) Total NK cell dynamics of vavFLIP$_R$ mice

Figure 7.4: Fitting to vavFLIP$_R$ data assuming a different killing rate of NK cells. Data points up to day 5 p.i. are considered for the parameter fitting.

7.2 Hypotheses Comparison

As previously mentioned, combinations of the basic hypotheses were tested to evaluate simultaneous effects of the low frequency of active caspase 3 and the low degranulation of NK cells during the IAV infection. The proposed hypotheses and their associated parameter set and observational likelihood are summarized in table 7.1.

Table 7.1: Hypothesis and observational likelihood evaluation.

Hypothesis	Estimated parameter set	Likelihood	AIC
Lower expression levels of active caspase 3 may affect the lifespan of healthy NK cells in vavFLIP$_R$ mice	$\{\mu_N\}$	6.811×10^{-10}	44.215
Lower frequency of active caspase 3 may affect the lifespan of infected NK cells in vavFLIP$_R$ mice	$\{\mu_{I_N}\}$	9.370×10^{-09}	38.972
Lower frequency of active caspase 3 may improve the viral production within infected NK cells in vavFLIP$_R$ mice	$\{\gamma\}$	4.080×10^{-07}	31.424
Impaired degranulation of NK cells may be linked to a different killing rate in vavFLIP$_R$ mice	$\{\xi\}$	1.402×10^{-08}	38.166
Lower frequency of active caspase 3 may affect the lifespan of healthy and infected NK cells in vavFLIP$_R$ mice	$\{\mu_N\, \mu_{I_N}\}$	2.584×10^{-08}	38.943
Lower frequency of caspase 3 may affect the lifespan of healthy NK cells and impaired degranulation may indicate a different killing rate of NK cells in vavFLIP$_R$ mice	$\{\mu_N\, \xi\}$	1.367×10^{-06}	31.006
Lower frequency of caspase 3 may affect the lifespan and viral production of infected NK cells in vavFLIP$_R$ mice	$\{\mu_{I_N}\, \gamma\}$	$\mathbf{3.377} \times 10^{-06}$	**29.197**
Lower frequency of caspase 3 may affect the lifespan of infected NK cells and impaired degranulation may be link to a different killing rate of healthy NK cells in vavFLIP$_R$ mice	$\{\mu_{I_N}\, \xi\}$	2.295×10^{-08}	39.180
Lower frequency of active caspase 3 may affect the lifespan of healthy NK cells and improve the viral production within infected NK cells in vavFLIP$_R$ mice	$\{\mu_N\, \gamma\}$	$\mathbf{5.145} \times 10^{-06}$	**28.355**

Most of the hypotheses allowed to obtain a satisfactory fit of the NK cell dynamics. However, only by assuming changes in the lifespan of healthy NK cells and the viral production of infected NK cells, the data of vavFLIP$_R$ mice was adequately fitted. In the IAV infection model, these changes are associated with the parameter set $\{\gamma, \mu_N\}$. This conclusion is supported by comparing the observational joint likelihood of the hypotheses and the AIC (table 7.1). Note that the assumptions related to the set $\{\gamma, \mu_N\}$ produced the highest observational likelihood. The obtained parameter values were $\mu_N = 1.319\ days^{-1}$ and $\gamma = 5.531$. The results of the fitting are presented in figure 7.5. The viral dynamics was fitted within the standard deviation

of the experimental data. Note however, that no change in the curvature of the viral load was observed. Hence, the monotonic increase of the viral load was accurately emulated. On the other hand, NK cells number was slightly overestimated at day 5 p.i.; however, the quantitative behavior of the NK cell dynamics was more accurately approximated than in the other cases.

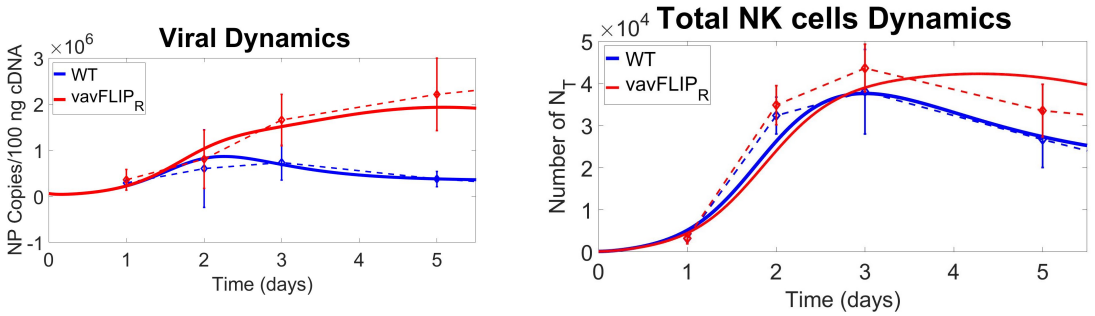

(a) Viral dynamics of vavFLIP$_R$ mice

(b) Total NK cell dynamics of vavFLIP$_R$ mice

Figure 7.5: Fitting to vavFLIP$_R$ data assuming that the lower frequency of 3 may affect the lifespan of healthy NK cells and the viral production of infected NK cells. Data points up to day 5 p.i. are considered for the parameter fitting.

Data fitting process predicts that a higher viral production rate of infected NK cells - up to 5 fold higher than the estimation for WT mice - causes the viral load observed in vavFLIP$_R$ mice. Therefore, one can infer that lower levels of active caspase 3 may contribute to a more efficient viral replication within infected NK cells. This conclusion may also explain the relatively higher viral load produced by infected NK cells of vavFLIP$_R$ mice in the *in vitro* experiment of section 4.4.2.

Furthermore, a slight increase in the death rate of healthy NK cells was estimated. This increment may be related to a higher biological exhaustion. As the infection exacerbates, more NK cells are recruited in the site of the infection. Consequently, more healthy NK cells get infected, losing their overall cytotoxic capabilities. Meanwhile the remaining healthy NK cells may be overwhelmed by an increase in the required killing of infected epithelial cells. This result may explain the impaired degranulation found on vavFLIP$_R$ NK cells (see section 4.4.1).

Note that the parameter set $\{\gamma, \mu_{I_N}\}$ –viral production rate and lifespan of infected NK cells, respectively– also provides a relatively high joint observational likelihood and low AIC. The following results were obtained: $\mu_{I_N} = 2.499\ days^{-1}$ and $\gamma = 12.283$. Interestingly, as in the previous case, an increase in the viral production rate of infected NK cells was obtained. Nevertheless, this increment was higher than in the previous hypothesis, which may be related to the elevated value of the parameter μ_{I_N}. Since infected NK cells die at a faster rate in this hypothesis, a higher viral production is required so that the viral load data can be satisfied. The fitting results are shown in figure 7.6. Note that the viral dynamics was fitted in the standard

deviation of the experimental data. However, the maximum of the curve is observed before day 5 p.i.. Hence, the monotonic increase of the viral load is not followed. On the other hand, the number of NK cells was highly overestimated at day 5 p.i..

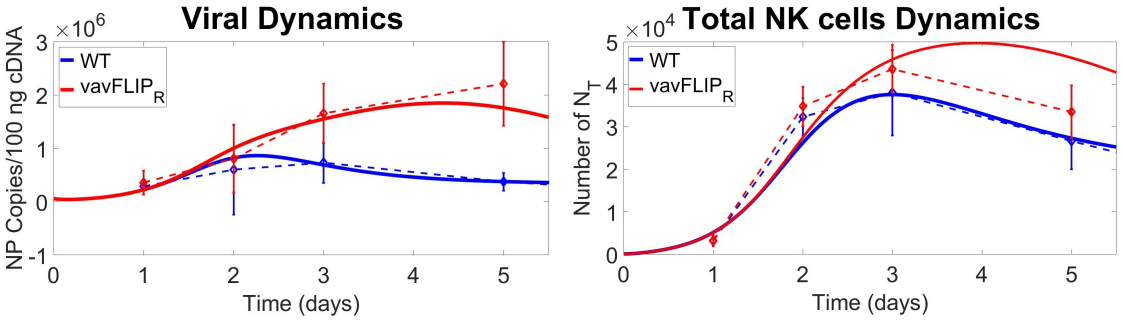

(a) Viral dynamics of vavFLIP$_R$ mice (b) Total NK cell dynamics of vavFLIP$_R$ mice

Figure 7.6: Fitting to vavFLIP$_R$ data assuming that lower frequency of 3 may affect the lifespan and viral production of infected NK cells. Data points up to day 5 p.i. are considered for the parameter fitting.

7.2.1 Lower frequency of active caspase 3 may affect the lifespan of healthy and infected NK cells and improve the viral production within infected NK cells in vavFLIP$_R$ mice

Previous results suggest that alterations in lifespan of both healthy and infected NK cells as well as in the viral production rate within infected NK cells, are required to accurately fit both viral and total NK cell data in vavFLIP$_R$ mice. All these alterations are associated with the lower frequency of active caspase 3 observed in NK cells of vavFLIP$_R$ mice. Thus, the parameters μ_N, μ_{I_N} and γ were re-estimated by the MCMC algorithm. The results are presented in figure 7.7 and in table 7.2. The obtained joint observational likelihood was $\mathbf{1.611 \times 10^{-05}}$.

Note that, despite an underestimation of the NK cells at day 2 p.i., most of the data points are predicted within their respective standard deviation. The maximum of the viral load was observed at day 4.2 p.i.. The monotonic increase of the viral load is not satisfied. A significant increment in the estimation of the viral production rate γ and lifespan of infected NK cells μ_{I_N} were observed. Such results may imply a connection between these two parameters. Therefore, a correlation analysis between them was performed. A co-linear dependency between μ_{I_N} and γ was found, as observed in figure 7.8. As infected NK cells die at a faster rate, the algorithm estimates a higher viral replication so that the viral load data can be fit. Therefore, in order to estimate both of these parameters properly, additional information regarding infected NK cell kinetics is required.

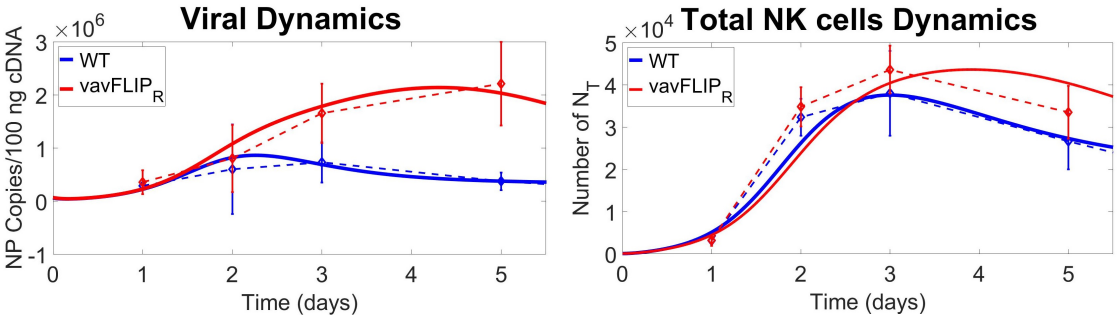

(a) Viral dynamics of vavFLIP$_R$ mice (b) Total NK cell dynamics of vavFLIP$_R$ mice

Figure 7.7: Fitting to vavFLIP$_R$ data assuming the lower frequency of active caspase 3 affects the lifespan of healthy and infected NK cells and improves the viral production within infected NK. Data points up to day 5 p.i. are considered for the parameter fitting.

Table 7.2: Parameters

Parameters	Values	Units
μ_N	1.201	$days^{-1}$
μ_{I_N}	2.476	$days^{-1}$
γ	13.820	

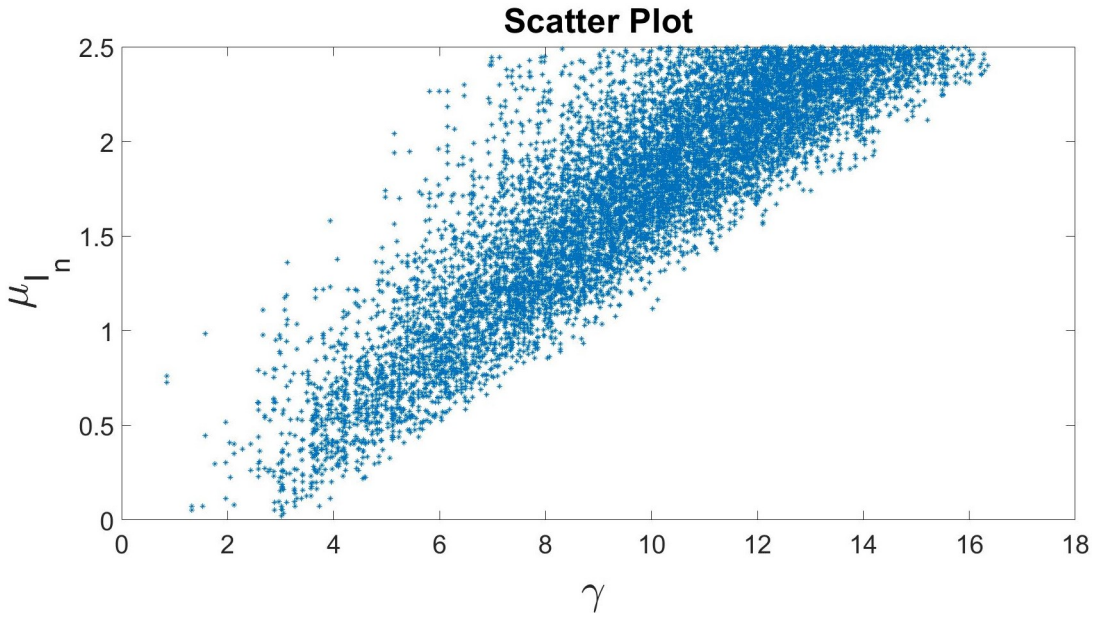

Figure 7.8: Scatter plot γ vs μ_{I_N}. A co-linear dependency exists between the viral production rate and the lifespan of infected NK cells.

7.3 Phase space and dynamical terms of the best fitting of vavFLIP$_R$ data

7.3.1 State Variables

In this section, the phase space obtained by best fit is presented. Simulation is performed up to day 10 p.i.. The results are presented in figures 7.10 and 7.9.

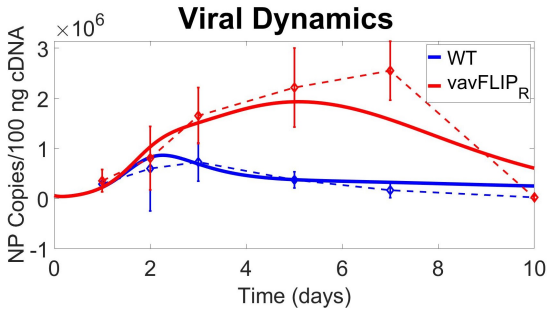

(a) Viral dynamics of vavFLIP$_R$ mice

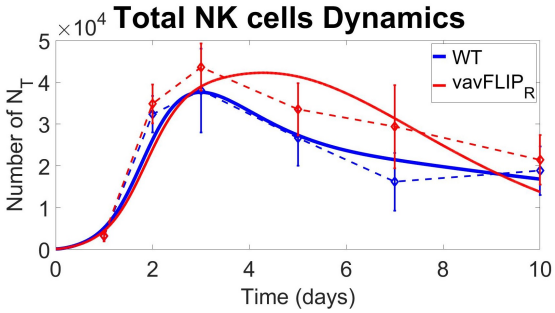

(b) Total NK cell dynamics of vavFLIP$_R$ mice

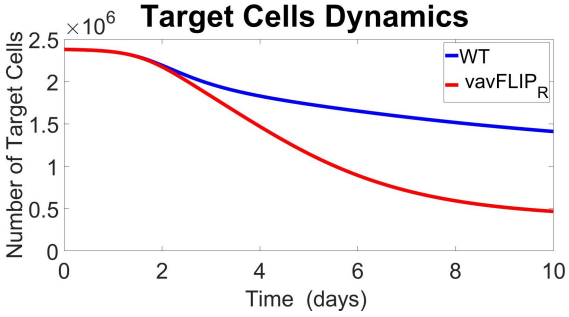

(c) Time evolution of the epithelial cells T

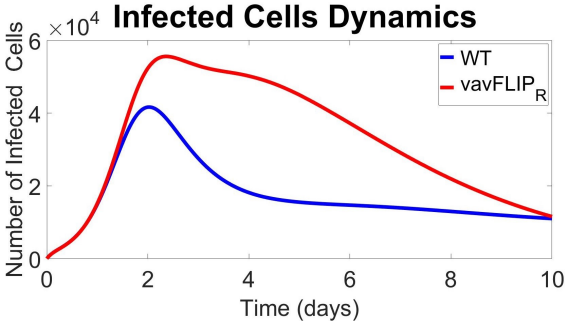

(d) Time evolution of the infected epithelial cells I

Figure 7.9: Time evolution of the virus V, total number of NK cells N_T, Target cells T and infected cells I. The parameters were estimated based on the first 5 days of infection, and simulated up to day 10 p.i ..

Note that viral clearance is not fully achieved at day 10 p.i.. Similar to the results of WT, the absence of the adaptive immune response affects the prediction capabilities of the model at day 10. Moreover, similar to the WT case, the NK cell dynamics at day 10 p.i. is not accurately predicted, which may occur due to the simplifications imposed in the model regarding NK cell recruitment and activation. Interestingly, a drastic decrease of the viral load is observed without the inclusion of the adaptive immune response. As expected a higher number of infected epithelial cells is predicted, with a 33% increment compared to the WT case. At the peak of

the infection, up to 50% of the epithelial cells were dead. Additionally, similar to the WT case, a delay of infected NK cells can be observed in figure 7.10b, implying that a minimal viral load (around $6 \times 10^5\, NP\, Copies/\, 100\, ng\, cDNA$)is required so that infection of NK cells takes place.

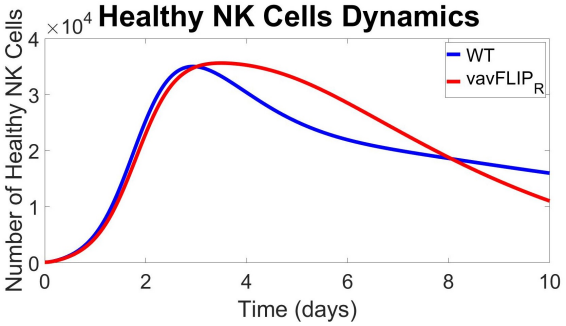

(a) Time evolution of the healthy NK cells N

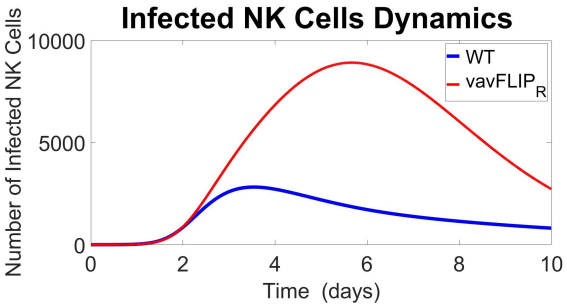

(b) Time evolution of the infected NK cells I_N

Figure 7.10: Time evolution of the NK cells N and infected NK cells I_N . The parameters were estimated based on the first 5 days of infection, and simulated up to day 10 p.i ..

7.3.2 Dynamical terms of the ODE system

The terms of the r.h.s of the ODE model were independently analysed to evaluate the behavior IAV kinetics in vavFLIP$_R$ mice. The evolution in time of these terms are presented in figures 7.11 and 7.12.

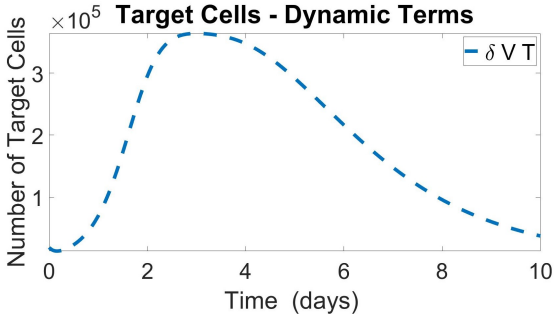

(a) Components of the r.h.s. of the Target cell dynamics

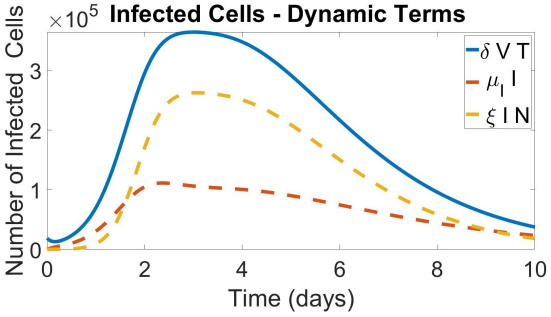

(b) Components of the r.h.s. of the Infected cell dynamics

Figure 7.11: Terms of the r.h.s. of Target cell dynamics (Eq. 5.1) and Infected cell dynamics (Eq. 5.2) in vavFLIP$_R$ data.

As observed in figure 7.11b, the qualitative behavior of the terms of the viral dynamics in vavFLIP$_R$ is similar to the one observed in WT (see figure 6.10b).

The terms of the viral dynamics are presented in figure 7.12a. Note that the viral replication within infected NK cells plays an important role in the viral dynamics; in fact, after day 5 p.i., viral production by infected NK cells is higher than by infected epithelial cells. In figure 7.12b, the terms of the healthy NK cell dynamics are introduced. As in the WT results, the influence of the infection rate of NK cells ($\delta\alpha NV$) to the overall NK cell dynamics is minor. Notice in 7.12c that the death rate of infected NK cells overcomes the contribution of the infection rate on NK cells around day 6 p.i., i.e. 2 days later than in the WT case (see figure 6.11c).

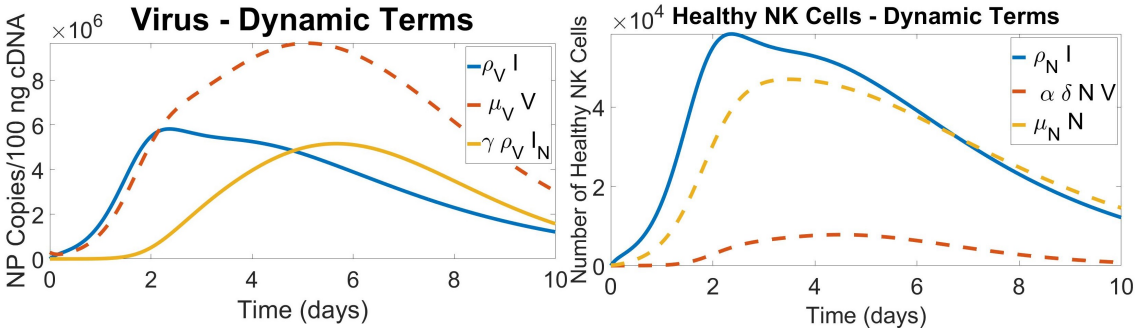

(a) Components of the r.h.s. of the Viral dynamics

(b) Components of the r.h.s. of the NK cell dynamics

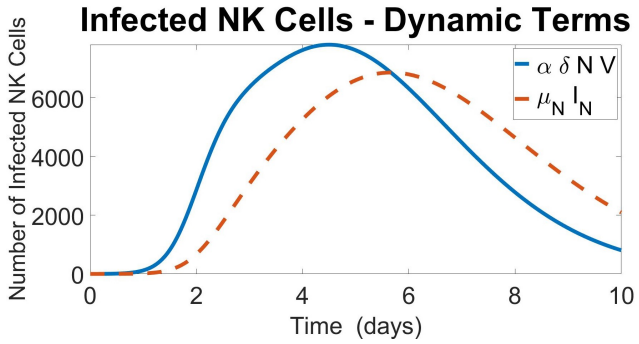

(c) Components of the r.h.s. of the infected NK cell dynamics

Figure 7.12: Terms of the r.h.s. of Viral dynamics (Eq. 5.3), Healthy and Infected NK cell dynamics (Eq. 5.4 and 5.5, respectively) in vavFLIP$_R$ data..

7.4 Summary

The parameters estimated from WT mice data in the previous chapter were used for simulating the vavFLIP$_R$ mice. Alteration in parameters associated with NK cell dynamics were proposed to be responsible for the altered viral dynamics in vavFLIP$_R$ mice. Three basic hypotheses were formulated and tested: 1) lower frequency of

active caspase 3 indicates that the lifespan of healthy and infected NK cells is affected; 2) lower frequency of active caspase 3 suggests that viral replication within NK cells is altered; 3) lower degranulation of NK cells found in vavFLIP$_R$ mice indicates a different killing rate. Combination of these hypotheses were also tested. The hypotheses were analyzed by investigating how well their corresponding mathematical representation fits to the experimental data.

The data fitting process predicted that a higher viral production rate within infected NK cells is responsible for a higher viral load in vavFLIP$_R$ mice. Furthermore, it is predicted that the lifespan of healthy NK cells is decreased in the transgenic mice; this may be associated with a biological exhaustion due to the high level of infection. This result implies that NK cells in vavFLIP$_R$ mice do not resist apoptosis. A correlation study revealed a co-linear dependency between viral production and the lifespan of infected NK cells. This correlation arises due to the lack of information regarding the infected NK cell kinetics.

Moreover, a drastic decrease in the viral load was observed, despite the absence of the adaptive immunity after day 7 p.i.. Therefore, the role of CTLs in the final clearance may not be as critical as expected. This result may explain the similar CTL kinetics observed in the Tafrishi's experiments 4.6. The decrease in the viral load is associated with the reduction in the number of infected NK cells.

8 Discussion

8.1 Usage of mathematical model to investigate IAV infection

Despite numerous researches, there are plenty of aspects of IAV infection that have not been discovered yet. In recent years, mathematical modelling has arisen as a tool to explain and quantify IAV kinetics and its relationship with the immunological response of the host. The information obtained by such models is critical in the evaluation of new hypotheses which could be impossible or very difficult by means of current experimentation [9]. Furthermore, the usage of mathematical models has been proved to be a valuable tool to design new experiments, propose better treatments and evaluate the effects of drugs, not only for IAV but also for human immunodeficiency viruses (HIV) and hepatitis C viruses (HCV) [17, 9, 92, 28].

Mathematical models are constructed from limited data and simplifying assumptions. These assumptions are implemented in order to reduce the complexities of the system and to address the most important characteristic of experimental settings [30]. This is necessary because every experiment is subjected to variation associated with virus strain, host, genetic modifications etc. [17]. In this study, a mathematical model based on a system of ODEs was used as a tool to dissect the experimental results obtained by Tafrishi [107]. One particular important characteristic of the experiments carried out by Tafrishi is the interaction between NK cells and IAV.

Different studies have shown that NK cells, as well as other cell types of the innate immune response, can get infected by IAV. This mechanism enables IAV to evade the effect of the innate immune response [76, 107]. Mao et al. stated that the new virions produced by infected NK cells are not productive [76]. Conversely, Tafrishi found that infected NK cells' progeny were indeed infectious [107]. However, this phenomenon has not been quantified nor has been included in previous mathematical models. The IAV model presented in this research is the first one to include the dynamics of infected NK cells. The contribution of infected NK cell population during an IAV infection was observed by fitting the proposed IAV model to the WT data of Tafrishi's investigation and by evaluating the r.h.s. of the respective ODE system. As presented in figure 6.11c, the role of the viral replication within infected NK cells in the viral dynamics is minor in comparison to the other terms. The negligible effect of the infected NK cell dynamics explains the accurate fitting of the viral dynamics in previous research [53, 54], which did not consider the infection mechanism of NK

cells. Nevertheless, in the vavFLIP$_R$ mice, the contribution of viral replication within infected NK cells is critical in order to explain the viral load observed in vavFLIP$_R$ mice. This result proves the importance of data specific modelling to study IAV infection.

In the proposed IAV infection model, NK cells are considered to get infected only by direct virus binding. However, additional mechanisms, such as contact of healthy NK cells with infected epithelial cells and interactions between healthy and infected NK cells may also play a role. In those cases, spatial distribution of the cells must be taken into account. Therefore, partial differential equations or agent based models are required. Elimination mechanisms of infected NK cells, such as killing by either healthy NK cells and/or CTLs, could also affect the clearance of the infection. Nonetheless, the assumptions used in this research allowed an adequate fitting to the experimental data.

8.2 Parameter Estimation Methods

In this research, the parameters of the ODE system were estimated by the MCMC random walk algorithm. This method performs a Bayesian inference on the parameters given the available data. Bayesian inference was selected because it allows to incorporate data uncertainty in a mathematical consistent manner. In general, MCMC methods are computationally expensive due to exploration of the parameter space. Recently, new methodologies which use sample-free Bayesian update, have been developed [88]. These methods represent random variables with spectral series expansions, reducing the computational time required to estimate the parameters. The reduction of the computational time is critical for the evaluation of large mathematical models. However, given the size of the ODE system and the reduced number of parameters estimated in this research, the computational time of the random walk MCMC was adequate. Another advantage of the sample-free Bayesian update is that the measurement errors are not assumed to follow any specific distribution [88]. However, since random errors are represented reasonably well by normal distributions, it was assumed in this work that the measurement errors of the data follow a normal distribution.

MCMC allows to circumvent practical non-identifiability problems of ODEs and to reduce the search in parameter space by including knowledge from the literature in the form of prior distributions [121, 22]. However, the limited amount of data can affect the ability of the algorithm to approximate the distribution of the parameters. This is observed in the distribution of the parameters γ and α, which represent the percentage of viral production and infection rate of NK cells in relation to the epithelial cells. Both of these distributions are flat. Therefore, the uncertainty of these parameters cannot be evaluated.

8.3 The role of c-FLIP$_R$ in antiviral immunity

The anti-apoptotic c-FLIP proteins inhibit apoptosis at the death-inducing signaling complex of death receptors. The role of c-FLIP$_R$ protein in the immune system has been investigated by using transgenic mice which express murine c-FLIP$_R$ in all hematopoietic cell [115, 107]. When challenged with Listeria monocytogenes, vavFLIP$_R$ mice exhibited better bacterial clearance, less liver necrosis and less caspase 3 activation compared with infected WT littermate [115]. In Tafrishi's investigation, on the other hand, vavFLIP$_R$ presented a higher viral load than WT mice, despite having a higher number of NK cells [107]. By depleting NK cells *in vivo* prior to and during an IAV infection, Tafrishi observed the viral load differences between vavFLIP$_R$ and WT mice disappeared. These results indicated that a higher number of NK cells is responsible for the exacerbation of the IAV infection [107]. Nevertheless, the causes behind these results were not clear. In this research, different mechanisms were investigated in order to account for the results obtained by Tafrishi.

The fitting to the vavFLIP$_R$ data produced interesting and counterintuitive results, which differ from Tafrishi's interpretation of the experimental data. One of the explanations provided by Tafrishi regarding the role of C-FLIP$_R$ was that apoptosis resistant NK cells in vavFLIP$_R$ mice may provide a reservoir for IAV to replicate for a longer period of time [107]. However, in this work, a decrease in the lifespan of healthy NK cells was predicted, implying that c-FLIP$_R$ expression does not make NK cells more resistant to apoptosis (see section 7.2.1). Moreover, IAV infected NK cells with a longer lifespan alone cannot explain the observed viral load in vavFLIP$_R$ mice. The data fitting process predicted that a higher viral production within infected NK cells is a necessary condition for emulating the viral load (see section 7.2).

Additionally, the higher viral replication within NK cells of vavFLIP$_R$ mice, found in this work, can explain the results obtained in vitro experiment performed by Tafrishi (see section 4.4.2). In her research, Tafrishi infected freshly isolated NK cells and measured the NP copies produced by them after 6 hours. As observed in figure 4.7, NK cells from vavFLIP$_R$ mice produced a higher viral load than NK cells from WT mice. Considering the short period of time in which this experiment was carried out, a longer lifespan of infected NK cells, as suggested by Tafrishi, may not play a significant role in the observed differences in the viral loads. However, a more efficient viral replication within NK cells of vavFLIP$_R$ mice can account for this result, since this effect can be observed even in short time periods. Nevertheless, the intracellular mechanisms of such results are unknown. In fact, the results obtained in this work disagrees with previous research. Wurzer et al. found that caspase 3 activation during apoptosis is critical for the propagation of IAV within MDCK cells [127]. On the other hand, caspase-3-independent apoptosis has been recently investigated [109]. According to Takahashi, sulfatide is responsible for a more efficient IAV propagation

in caspase-3-independent apoptosis. This research may indicate that by blocking the caspase-3 apoptosis, IAV may use a different mechanism to propagate more efficiently within NK cells.

Finally, a correlation study revealed a co-linear dependency between viral production and the lifespan of infected NK cells. This correlation arises due to the lack of information regarding the infected NK cell kinetics. As the algorithm estimated the lifespan to shorter values to satisfy the NK cells data, an increment the viral production rate occurs in order to accurately fit the viral load. Therefore, further studies that independently evaluate the infected NK cell kinetics in vavFLIP$_R$ mice are required so that their impact can be evaluated by the model.

8.4 NK cell kinetics during an IAV infection

One of the most important simplifications imposed in this work was to assume that the lifespan of healthy and infected NK cells were equal. This assumption was set due to the limited information regarding the infected NK cell kinetics. Tafrishi investigated NK cell kinetics during an IAV infection by measuring the total number of NK cells in lung-draining lymph nodes [107]. However, the kinetics of healthy and infected NK cells were not independently quantified. For this reason, the random walk MCMC algorithm estimated a flat posterior of the death rate of infected NK cells (see figure 6.6). The highest joint observational likelihood (i.e. the most accurate data fitting) was obtained by fixing the initial number of healthy NK cells to 100 $cells$ and setting the lifespan of healthy and infected NK cells to be equal. This lifespan was estimated to 1.298 $days$. The selected initial number of healthy NK cells is consistent with the distribution obtained in previous parameter estimations. Moreover, a flat posterior was obtained for the parameters related to the infection and viral production rate within infected NK cells in WT mice. This suggests that the information used in this study is insufficient to accurately determine the uncertainties of these parameters. However, their estimates indicate that infection and viral replication rate within NK cells are similar to the epithelial cells.

Another interesting model prediction was the decrease in the lifespan of healthy NK cells for vavFLIP mice. This result, however, is counterintuitive considering the higher accumulation of NK cells in vavFLIP$_R$ mice in comparison with the WT littermates (see figure 4.3). Tafrishi suggested that the higher accumulation of NK cells in vavFLIP$_R$ was related to apoptosis resistance due to the low frequency of active caspase 3. Nevertheless, factors such as a higher recruitment of NK cells due to higher levels of infections were not considered. The model outcome implies that healthy NK cells of vavFLIP$_R$ mice do not resist apoptosis despite the lower expression levels of caspase 3 observed by Tafrishi [107]. A possible explanation may lie in the biological exhaustion experienced by NK cells. A higher viral load results

in an increase in the recruitment of NK cells, but also in more infected NK cells. As a result, the overall cytotoxic capabilities of the NK cell population is reduced. Hence, the remaining healthy NK cells are forced to kill more infected epithelial cells than in WT mice. This can be confirmed by analyzing the contribution of NK cells' killing in the ODE system (see figures 6.10b and 7.11b). Note that the curve corresponding to this term is higher in the vavFLIP$_R$ mice than in WT littermates. This hypothesis may explain the impaired degranulation of NK cells from vavFLIP$_R$ mice reported by Tafrishi (section 4.4.1) [107].

Interestingly, the kinetics of the healthy NK cells in the WT and vavFLIP$_R$ were similar. As observed in figure 7.10a, the maximum number of healthy NK cells were comparable in both types of mice. However, after day 3 p.i. a relative higher number of healthy NK cells was observed, which is related to the increased recruitment rate due to the higher number of infected epithelial cells. On the other hand, the kinetics of infected NK cells of WT and vavFLIP$_R$ mice differ drastically from each other. After day 2 p.i., the number of infected NK cells in vavFLIP$_R$ mice accumulated up to 3 times the number in WT mice (see figure 7.10b). Nonetheless, the real number of infected NK cells may be different as predicted, due to the co-linear dependency between viral production and the lifespan of infected NK cells.

Furthermore, the predicted number of NK cells at day 10 p.i. was lower than expected. This underestimation arises most likely due to the simplification imposed in the IAV infection model, regarding the recruitment and activation of NK cells. In the model, NK cell recruitment is proportional to the number of infected epithelial cells. However, NK cells are recruited by IFN type I; therefore, the increment in the recruitment at day 10 p.i., in comparison with day 7 p.i., may be related to the second peak observed in the IFN-α data (figure 4.9). This result has been observed in multiple research [90, 53, 54, 23, 24]. Nonetheless, incorporating the IFN-α dynamics is a rather complicated task as there is no explanation in the literature that can account for its second peak at day 7 p.i.. Dendritic cell kinetics, however, may explain IFN-α dynamics. As previously explained, after antigen presentation, dendritic cells accumulate into the lungs. Since dendritic cells are one of the main sources of IFN type I, their accumulation in the lung may explain the second peak observed in IFN-α.

The role of NK cells in the immune response against IAV infection has been a subject of debate [105, 1, 131, 132, 33, 122]. Several studies have reported that depletion of NK cells or defects in NK cells functionality cause morbidity or delay in viral clearance [105, 1]. The WT data [107] and the simulation of this research confirms the importance of NK cells in the control of the IAV infection. As observed in figure 6.7, even without including the effect of adaptive immune response, a decrease in the viral load was observed after day 2 p.i.. The final clearance, however, seems to depend on the adaptive immune response. In contrast, there are several studies

reporting that NK cells can exacerbate the pathology of the IAV infection in mice [131, 132, 33]. The outcome of those investigations may be explained by the dynamics of infected NK cells. An increase in the number of NK cells implies a higher number of infected NK cells. Therefore, the overall cytotoxic capabilities of NK cell population may decrease. Furthermore, the evaluation of the r.h.s. terms of the ODE for WT and vavFLIP$_R$ mice suggests that viral kinetics can be affected by a sufficiently high number of infected NK cells (see figures 6.10b and 7.11b).

8.5 The role of CD8$^+$ T cells during an IAV infection

The role of CTLs during the clearance of IAV infection is critical. Researches have shown that in the absence of key components of the adaptive immune response, such as CD4$^+$ T cells, B cells and neutralizing antibody, CTLs are still able to control the viral infection [35, 45]. Besides their cytotoxic functions, CTLs are able to produce a variety of pro-inflamatory cytokines, critical for the final clearance of the infection, such as TNF-α and IFN-γ [116].

In this study, the simulation of WT data predicted a persistent viral load after day 5 p.i.. Since, the adaptive immune response starts to be detected in the site of the infection after day 5 p.i., it was concluded that the persistent viral load occurred due to the lack of the adaptive immune response in the IAV infection model. To verify this conclusion, a killing rate of infected epithelial cells by CTLs was included in the model. The CTL kinetics was emulated by a Hill equation. This resulted in a full viral clearance (see figure 6.16), confirming the importance of the CTLs in the clearance of the infection. Previous investigations have shown that CTL dynamics only can control the infection and clear the infection [54]. This could be the reason for which most IAV models do not usually include the innate immune response. Nonetheless, the decreases in the viral load in WT mice after day 2 p.i. (see figure 4.2) shows that NK cells are critical for controlling the spread of the IAV infection. However, NK cell activity is related to the initial levels of infection [122]. Therefore, NK cell role in controlling IAV infection may depend on initial viral load.

In the vavFLIP$_R$ case, the simulation results predicted a drastic decrease in the viral load, despite the absence of the adaptive immune response. Given the higher levels of IFN-γ (see figure 4.10) observed in vavFLIP$_R$ mice, CTLs were expected to be responsible for the reduction in the viral load. The model prediction may be related to the decrease in the infected NK cell population after day 7 p.i., since their contribution to viral production is critical in the vavFLIP$_R$ case. This can be observed in figures 6.11c and 7.12c. Since the full clearance is not achieved by the model in vavFLIP$_R$ mice, the crucial role of CTLs in the final clearance of IAV infection is demonstrated.

Higher levels of IFN-γ (mainly produced by CTLs) were observed by Tafrihi [107, 108]. Since the kinetics of CTLs were similar in both mice, one may conclude that the changes in IFN-γ kinetics may be related to an over-stimulated adaptive immune response. The viral load reported by Tafrishi in vavFLIP$_R$ mice may be related to the over-stimulation of CTLs. Nonetheless, NK cell activity may as well contribute to these changes. Several research have linked the activity of NK cells and CTLs during viral infection [122, 4, 89]. Tafrishi's investigation showed that CTL dynamics is not altered by NK cells depletion [107]. Nevertheless, $CD4^+$ T cells accumulation in the lungs almost duplicate after NK cell depletion. Given the importance of $CD4^+$ T cells in the activity of CTLs and the change in the kinetics of healthy NK cells predicted by the model, one can conclude that CTLs activity in vavFLIP$_R$ mice differ from the one in WT littermates.

8.6 Concluding Remarks and outlook

Apoptosis is a critical mechanism during infection, as it limits the resources for pathogen replication. Cellular-FLIP interferes with procaspase-8 apoptosis and is pivotal in its regulation during immune responses. Apoptosis has been reported to be linked to different aspects of IAV infection. The role of c-FLIP$_R$ and its relation with different aspects of IAV has been previously investigated by Tafrishi [107]. Herein, a mathematical model has been used to test different hypotheses that can account for the role of c-FLIP$_R$ within NK cells during an IAV infection.

The results of the presented computational effort provided the following main implications in the context of IAV infection and the associated experimental models. The lower expression of caspase 3 enhances the viral replication within NK cells which accounts for the increase in the viral load observed in the experiments. Furthermore, despite the low frequency of active caspase 3, NK cells in vavFLIP$_R$ do not resist apoptosis. Since there is no differentiation between healthy and infected NK cells in the data, several limitations were found in order to determine parameters of the infected NK cell dynamics. For this reason, it was necessary to assume an equal lifespan for healthy and infected NK cells for fitting the WT data. This lack of information also results in the linear correlation found between viral production and the lifespan of infected NK in vavFLIP$_R$ mice.

These findings of this thesis may suggest that IAV usage of the caspase-3 for a better replication within NK cells is not as critical as in MDCK cells. Therefore, replication mechanisms may be cell dependent. On the other hand, the results of this research may also indicate that in the absence of caspase-3, IAV may use caspase-3-independent apoptosis mechanisms for a better replication. This research underlines the importance of regulation of apoptosis in NK cells during viral infections.

The mathematical model developed in this thesis can be used in the future to further evaluate the role of NK cells during an IAV infection as a function of the viral load. For this purpose, the proposed IAV model should be simulated using different initial viral loads, so that the variations of the healthy and infected NK cell dynamics can be observed. In pursuing this objective, the parameters derived in chapter 6 (WT mice data) should be used.

As previously mentioned, an important drawback of the proposed model is that it considers viral binding as the only infection mechanism of NK cells. Nevertheless, other mechanisms such as contact of healthy NK cells with infected epithelial cells, may also be critical. Furthermore, elimination mechanisms of infected NK cells, such as killing by either healthy NK cells and/or CTLs, could also be further examined. However, in order to quantify those mechanisms, additional experimental data are required, so that their contribution can be properly inferred.

Bibliography

[1] M.F. Abdul-Careem et al. Critical role of natural killer cells in lung immunopathology during influenza infection in mice. *J. Infect. Dis.*, 206(2):167 – 177, 2012. 72

[2] B. B. Aggarwal. Signalling pathways of the TNF superfamily: a double-edged sword. *Nat. Rev. Immunol.*, 3(9):745–756, 2003. 5

[3] S. Alam et al. CD4 T cell help is limiting and selective during the primary B cell response to influenza virus infection. *J. Virol.*, 88(2):314–24, 2014. 8

[4] D. M. Andrews et al. Innate immunity defines the capacity of antiviral T cells to limit persistent infection. *PLoS One*, 207(6):1333 – 43, 2010. 74

[5] C. Andrieu et al. An introduction to MCMC for machine learning. *Machine Learning*, 50(3):5–43, 2003. 13

[6] T.I. Arnon et al. Recognition of viral hemagglutinins by NKp44 but not by NKp30. *Eur. J. Immunol.*, 31(9):2680–2689, 2001. 8

[7] G.K. Atkin-Smith et al. The induction and consequences of influenza A virus-induced cell death. *Cell Death Dis.*, 9(10), 2018. 56

[8] P. Baccam et al. Kinetics of Influenza A Virus Infection in Humans. *Journal of Virology*, 80(15):7590–7599, 2006. 20, 22, 40, 41, 44, 46, 49, 55

[9] C. Beauchemin and A. Handel. A review of mathematical models of influenza A infections within a host or cell culture: lessons learned and challenges ahead. *BMC Public Health*, 11(7), 2011. 6, 18, 19, 22, 40, 41, 44, 46, 68

[10] C.A. Beauchemin. Modeling amantadine treatment of influenza A virus in vitro. *J Theor Biol.*, 254(2):439–51, 2008. 20, 34

[11] G.T. Belz et al. Distinct migrating and nonmigrating dendritic cell populations are involved in MHC class I-restricted antigen presentation after lung infection with virus. *Proc. Natl. Acad. Sci. U. S. A.*, 101(23):8670–5, 2004. 7, 8

[12] A. Bender et al. The distinctive features of influenza virus infection of dendritic cells. *Immunobiology*, 198(5):552–567, 1998. 7

[13] T. Bergsbaken, S.L. Fink, and B. T. Cookson. Pyroptosis: host cell death and inflammation. *Nat. Rev. Microbiol.*, 7:99– 109, 2009. 4

[14] C.A. Biron et al. Natural killer cells in antiviral defense: function and regulation by innate cytokines. *Annu. Rev. Immunol.*, 17:189–220, 1999. 8

[15] C. M. Bishop. *Pattern Recognition and Machine Learning*. Springer, 2006. 11, 12

[16] G.A. Bocharov and A.A. Romanyukha. Mathematical Model of Antiviral Immune Response III. Influenza A Virus Infection. *Journal of Theoretical Biology*, 167(4):323–360, 1994. 20, 34, 49, 55

[17] A. Boianelli et al. Modeling Influenza Virus Infection: A roadmap for influenza research. *Viruses*, 7(10):5274–5304, 2015. 6, 19, 22, 32, 53, 68

[18] W. M. Bolstad. *Understanding Computational Bayesian Statistics*. Wiley Series in Computational Statistics, 2010. 11

[19] B.J. Bosch et al. Recombinant soluble, multimeric HA and NA exhibit distinctive types of protection against pandemic swine-origin 2009 A(H1N1) influenza virus infection in ferrets. *J. Virol.*, (19):10366 – 74, 2010. 6

[20] T. Broeke, R. Wubbolts, and W. Stoorvogel. MHC class II antigen presentation by dendritic cells regulated through endosomal sorting. *Cold Spring Harb. Perspect Biol.*, 5(12):1–21, 2013. 7

[21] K. Burham and D. Anderson. *Model selection and multimodel inference*. Springer, New York, NY., 2002. 11, 18

[22] B. Calderhead. *Differential Geometric MCMC Methods and Applications*. PhD thesis, University of Glasgow, Department of Computing Science, 2011. 9, 10, 11, 14, 37, 69

[23] P. Cao et al. Innate immunity and the inter-exposure interval determine the dynamics of secondary influenza virus infection and explain observed viral hierarchies. *Plos Computational Biology*, 11(8), 2015. 21, 34, 72

[24] P. Cao et al. On the role of CD8+ T cells in determining recovery time from influenza virus infection. *Front Immunol.*, 7:611, 2016. 21, 34, 72

[25] F. Carrat and A. Flahault. Influenza vaccine: the challenge of antigenic drift. *Vaccine*, 25:6852–6862, 2007. 6

[26] D. B. Chang and C.S. Young. Simple scaling laws for influenza A rise time, duration, and severity. *J. Theoretical Biology*, pages 621–635, 2007. 21

[27] X. Chen et al. Host immune response to influenza A virus infection. *Front Immunol.*, 9(320), 2018. 6

[28] J. M. Conway and A. S. Perelson. Post-treatment control of HIV infection. *PNAS*, 112(17):5467 – 5472, 2015. 68

[29] D. Cousineau and T. A. Allan. Likelihood and its use in parameter estimation and model comparison. *Mesure et evaluation en education*, 37(3):63–98, 2015. 11

[30] H. M. Dobrovolnyand et al. Assessing mathematical models of influenza infections using features of the immune response. *PLoS One.*, 8(2), 2013. 22, 68

[31] M. Donepudi et al. Insights into the regulatory mechanism for caspase-8 activation. *Mol. Cell*, 11(2):543– 549, 2003. 5

[32] B. V. Dons'koi, V.P. Chernyshov, and D.V. Osypchuk. Measurement of NK activity in whole blood by the CD69 up-regulation after co-incubation with K562, comparison with NK cytotoxicity assays and CD107a degranulation assay. *J Immunol Methods*, 372(1-2):187–195, 2011. 26

[33] X. Duan et al. NK-cells are involved in thymic atrophy induced by influenza A virus infection. *J. Gen. Virol.*, 96(11):3223–3235, 2015. 72, 73

[34] A. L. Edinger and C.B. Thompson. Death by design: apoptosis, necrosis and autophagy. *Curr. Opin. Cell Biol.*, 16(6):663 – 669, 2004. 5

[35] S.L. Epstein et al. Mechanism of protective immunity against influenza virus infection in mice without antibodies. *J. Immunol.*, 160(1):322–7, 1998. 73

[36] S. L. Fink and B. T. Cookson. Eukaryotic cells minireview apoptosis , pyroptosis , and necrosis : Mechanistic description of dead and dying eukaryotic cells. *Infect Immun.*, 73(4):1907 – 1916, 2005. 4

[37] Y. Fuchs and H. Steller. Live to die another way: modes of programmed cell death and the signals emanating from dying cells. *Nat. Rev. Mol. Cell Biol.*, 16(6):329–344, 2015. 4, 5

[38] H. Fujisawa. Inhibitory role of neutrophils on influenza virus multiplication in the lungs of mice. *Microbiol. Immunol.*, 45(10):679–688, 2001. 7

[39] P. A. Gagniuc. *Markov Chains: From Theory to Implementation and Experimentation.* Wiley, 2017. 13

[40] L. Galin and Others. *Handbook of Markov Chain Monte Carlo.* Chapman and Hall, 2011. 15

[41] S. Ganesan, A. T. Comstock, and U.S. Sajjan. Barrier function of airway tract epithelium. *Tissue Barriers*, 1(14), 2013. 7

[42] N. Gershenfeld. *The nature of mathematical modeling.* Cambridge University Press, 1999. 9

[43] W. Gilks, S. Richardson, and D. Spiegelhalter. *Markov Chain Monte Carlo in Practice*. Wiley, 1996. 13

[44] M. Girolami and B. Calderhead. Riemann manifold langevin and hamiltonian monte carlo methods. *J.R.Statist.Soc.*, 73(2):123–214, 2011. 17

[45] M.B. Graham and T.J. Braciale. Resistance to and recovery from lethal influenza virus infection in B lymphocyte-deficient mice. *J. Exp. Med.*, 186(12):2063–8, 1997. 8, 73

[46] D. R. Green, T. Ferguson, L. Zitvogel, and G. Kroemer. Immunogenic and tolerogenic cell death. *Nat. Rev. Immunol.*, 9:353–363, 2009. 1, 4, 5

[47] H. Guo et al. The functional impairment of natural killer cells during influenza virus infection. *Immunol Cell Biol.*, 87(8):579 – 89, 2009. 34

[48] E. Hairer, S. P. Nørsett, and G. Wanner. *Solving Ordinary Differential Equations I.* Springer Series in Computational Mathematics, 2003. 10, 12, 16

[49] E. Hairer and G. Wanner. *Solving Ordinary Differential Equations II: Stiff and Differential-Algebraic Problems.* volume 14 of Springer Series in Computational Mathematics, Springer-Verlag, Berlin„ 2010. 36

[50] W. Hamilton. On a general method in dynamics. *Philosophical Transactions of the Royal Society*, pages 274 – 308, 1834. 15

[51] B. Hancioglua, D. Swigona, and G. Clermontb. A dynamical model of human immune response to influenza A virus infection. *Journal of Theoretical Biology*, 246(1):70–86, 2007. 21, 34

[52] W. Hastings. Monte carlo sampling methods using markov chains and their applications. *Biometrika*, 57(1):97 – 109, 1970. 14

[53] E. A. Hernandez-Vargas and M. Meyer-Hermann. Innate immune system dynamics to influenza virus. *IFAC Proceedings Volumes*, 45(18):260–265, 2012. 21, 68, 72

[54] E.A. Hernandez-Vargas et al. Effects of aging on influenza virus infection dynamics. *J Virol.*, 88(8):4123–31, 2014. 21, 68, 72, 73

[55] B. P. Holder et al. Assessing the in vitro fitness of an oseltamivir-resistant seasonal A/H1N1 influenza strain using a mathematical model. *PLoS Comput Biol.*, 6(3), 2011. 5, 22

[56] F.L. Jr. Horsfall. On the reproduction of influenza virus; quantitative studies with procedures which enumerate infective and hemagglutinating virus particles. *J. Exp. Med.*, 100(2):135–161, 1954. 6

[57] D. C. S. Huang et al. Activation of Fas by Fasl induces apoptosis by a mechanism that cannot be blocked by Bcl-2 or Bcl-x(L). *Proc. Natl. Acad. Sci. U.S.A*, 96(26):14871 – 14876, 1999. 1, 5

[58] M. M. Hufford et al. Influenza-infected neutrophils within the infected lungs act as antigen presenting cells for anti-viral CD8+ T cells. *PLoS One*, 7(10), 2012. 7

[59] A. Iwasaki and P.S. Pillai. Innate immunity to influenza virus infection. *Nat. Rev. Immunol.*, 14(5):315–328, 2014. 7

[60] J. McGill J., N. Van Rooijen, and K.L. Legge. Protective influenza-specific CD8 T cell responses require interactions with dendritic cells in the lungs. *J Exp Med.*, 205(7):1635 – 1646, 2008. 7, 55

[61] O.P. Joffre et al. Cross-presentation by dendritic cells. *Nat Rev Immunol*, 12(8):557– 569, 2012. 7

[62] B. E. Johansson, D. J. Bucher, and E. D. Kilbourne. Purified influenza virus hemagglutinin and neuraminidase are equivalent in stimulation of antibody response but induce contrasting types of immunity to infection. *J. Virol.*, 63(3):1239–1246, 1989. 8

[63] S.M. Kaech and R. Ahmed. Immunology. CD8 T cells remember with a little help. *Science*, 300(5617):263–265, 2003. 8

[64] J. Kaipio and E. Somersalo. *Statistical and Computational Inverse Problems*. Springer - Applied Mathematical Sciences, 2005. 12

[65] A. Kasia et al. Modeling Within-Host Dynamics of Influenza Virus Infection Including Immune Responses. *PLOS Computational Biology*, 8(6), 2012. 32, 34

[66] J.F. Kerr, A.H. Wyllie, and A.R. Currie. Apoptosis: a basic biological phenomenon with wide-ranging implications in tissue kinetics. *Br. J. Cancer*, 26:239–57, 1972. 1

[67] G. Kroemer et al. Classification of cell death: recommendations of the nomenclature committee on cell death 2009. *Cell Death Differ*, 16(1):3 – 11, 2008. 4

[68] I. Kuzmanovska. Markov Chain Monte Carlo methods in biological mechanistic models, 2012. 37

[69] P.O. Lang et al. Effectiveness of influenza vaccine in aging and older adults: Comprehensive analysis of the evidence. *Clin. Interv. Interv. Aging*, 7:55–64, 2012. 6

[70] L.L. Lanier. Up on the tightrope: natural killer cell activation and inhibition. *Nat. Immunol.*, 9(5):495 – 502, 2008. 8

[71] E. W. Larson et al. Influenza virus population dynamics in the respiratory tract of experimentally infected mice. *Infect Immun.*, 13(2):438 – 447, 1976. 19

[72] H.Y. Lee et al. Simulation and prediction of the adaptive immune response to influenza a virus infection. *J. Virol.*, 83(14):7151–7165, 2009. 6

[73] K.L. Legge and T.J. Braciale. Accelerated migration of respiratory dendritic cells to the regional lymph nodes is limited to the early phase of pulmonary infection. *Immunity*, 18(2):265–277, 2003. 7, 8

[74] D.J.C. MacKay. *Information Theory, Inference and Learning Algorithms*. Cambridge University Press, 2003. 12, 14, 15

[75] A. Mandal and C. Viswanathan. Natural killer cells: In health and disease. *Hematol Oncol Stem Cell Ther*, 8(2):47–55, 2015. 8

[76] H. Mao et al. Influenza virus directly infects human natural killer cells and induces cell apoptosis. *J. Virol.*, 83(18):9215–9222, 2009. 68

[77] H. Mao et al. Inhibition of human natural killer cell activity by influenza virions and hemagglutinin. *J Virol*, 84(9):4148–4157, 2010. 31

[78] J. McGill, J. W. Heusel, and K. L. Legge. Innate immune control and regulation of influenza virus infections. *J. Leukoc. Biol*, 86:803–812, 2009. 7

[79] D. R. McIlwain, T. Berger, and T. W. Mak. Caspase functions in cell death and disease. *Cold Spring Harb. Perspect. Biol*, 5(4), 2013. 4

[80] N. Metropolis et al. Equation of state calculations by fast computing machines. *Journal of Chemical Physics*, 21(6):1087 – 1092, 1953. 14

[81] H. Miao et al. Quantifying the early immune response and adaptive immune response kinetics in mice infected with influenza A virus. *J Virol*, 84(13):6687 – 6698, 2010. 22, 34

[82] D.J. Mock et al. Macrophages are required for influenza virus infection of human lymphocytes. *J Clin Invest.*, 79:620–624, 1987. 27

[83] L. Möhler et al. Mathematical model of influenza a virus production in large-scale microcarrier culture. *Biotechnol Bioeng.*, 90(1), 2005. 20

[84] K.M. Neuzil et al. Burden of interpandemic influenza in children younger than 5 years: a 25-year prospective study. *J Infect Dis*, 185(2):147–152, 2002. 6

[85] V. Nikoletopoulou et al. Crosstalk between apoptosis, necrosis and autophagy. *Biochim. Biophys*, Acta 1833:3448–3459, 2013. 4

[86] T.H. Oguin et al. Phospholipase d facilitates efficient entry of influenza virus, allowing escape from innate immune inhibition. *J. Biol. Chem.*, 289(37):25405–25417, 2014. 6

[87] S. Orrenius, P. Nicotera, and B. Zhivotovsky. Cell death mechanisms and their implications in toxicology. *Toxicol. Sci.*, 119:3 – 19, 2011. 1, 5

[88] O. Pajonk et al. A deterministic filter for non-gaussian bayesian estimation. *Physica D: Nonlinear Phenomena*, 241:775 – 788, 2011. 10, 69

[89] K. Pallmer and A. Oxenius. Recognition and regulation of T cells by NK cells. *Front Immunol.*, 7, 2016. 74

[90] K.A. Pawelek et al. Modeling within-host dynamics of influenza virus infection including immune responses. *PLoS Comput Biol.*, 8(6), 2012. 21, 72

[91] J. Malik Peiris, M. de Jong, and Y. Guan. Avian influenza virus (H5N1): a threat to human health. *Clin Microbiol*, 20(2):243–267, 2007. 2, 5

[92] A. S. Perelson and J.E. Guedj. Modelling hepatitis C therapyâpredicting effects of treatment. *Nat Rev Gastroenterol Hepatol.*, 12(8):437–445, 2015. 68

[93] M. E. Peter et al. The role of CD95 and CD95 ligand in cancer. *Cell Death Differ.*, 22(4):549–559, 2015. 5

[94] C.W. Potter. A history of influenza. *J. Appl. Microbiol.*, 91:572–579, 2001. 6

[95] B. Pulendran and M. S. Maddur. Innate immune sensing and response to influenza. *Curr. Top. Microbiol. Immunol*, 386:23–71, 2015. 7

[96] A. Raue et al. Structural and practical identifiability analysis of partially observed dynamical models by exploiting the profile likelihood. *Bioinformatics*, 25(15):1923– 1929, 2009. 11

[97] P. Robert and G. Casella. *Monte Carlo Statistical Methods*. Springer, 2004. 12

[98] T. Samji. Influenza a: Understanding the viral life cycle. *Yale J. Biol. Med.*, 82(4):153 – 159., 2009. 5

[99] C. J. Sanders, P. C. Doherty, and P. G. Thomas. Respiratory epithelial cells in innate immunity to influenza virus infection. *Cell Tissue Res.*, 343:13–21, 2011. 7

[100] C. Scaffidi et al. The role of c-FLIP in modulation of CD95-induced apoptosis. *J. Biol. Chem.*, 274(3):1541 – 1548, 1999. 1, 5

[101] P. Schirmer and M. Holodniy. Oseltamivir for treatment and prophylaxis of influenza infection. *Expert Opinion on Drug Safety*, 8(3):357 – 371, 2009. 2, 5

[102] S. Schultz-Cherry. Role of NK cells in influenza infection. *Curr Top Microbial Immunol.*, 386:109 – 120, 2015. 6

[103] L.M. Schwartz et al. Do all programmed cell deaths occur via apoptosis? *PNAS*, 90(3):980–984, 2008. 4

[104] A. M. Smith. Host-pathogen kinetics during influenza infection and coinfection: insights from predictive modeling. *Immunol Rev.*, 285(1):97 – 112, 2018. 22

[105] J. Stein-Streilein and J. Guffee. In vivo treatment of mice and hamsters with antibodies to asialo gm1 increases morbidity and mortality to pulmonary influenza infection. *J. Immunol.*, 136(4):1435–1441, 1986. 72

[106] K.C. Stone et al. Allometric relationships of cell numbers and size in the mammalian lung. *J Respir Cell Mol Biol.*, 6(2):235–43, 1992. 40, 41, 44, 46

[107] N. Tafrishi. *The role of c-FLIP in anti-viral immunity.* PhD thesis, Technischen Universität Carolo-Wilhelmina zu Braunschweig, Fakultät für Lebenswissenschaften, 2016. xii, xiii, 1, 2, 4, 5, 6, 7, 8, 22, 23, 24, 25, 26, 27, 28, 29, 30, 31, 34, 56, 57, 59, 68, 70, 71, 72, 74

[108] N. Tafrishi. private communication, 2018. xiii, 29, 30, 74

[109] T. Takahashi, M. Takaguchi, T. Kawakami, and T. Suzuki. Sulfatide regulates caspase-3-independent apoptosis of influenza A virus through viral PB1-F2 protein. *PLoS One*, 8(4), 2013. 70

[110] S.I. Tamura and T. Kurata. Defense mechanisms against influenza virus infection in the respiratory tract mucosa. *Jpn J Infect Dis*, 57(6):236 – 47, 2004. 53

[111] A. Tarantola. *Inverse Problem Theory and Methods for Model Parameter Estimation.* SIAM, 2004. 11, 12, 14

[112] J. K. Taubenberger and D.M. Morens. The pathology of influenza virus infections. *Annu. Rev. Pathol.*, 3:499 – 522, 2008. 6

[113] J.K. Taubenberger and J.C. Kash. Influenza virus evolution, host adaptation, and pandemic formation. *Cell Host Microbe*, 7(6):440–451, 2010. 6

[114] R.C. Taylor, S. P. Cullen, and S. J. Martin. Apoptosis: controlled demolition at the cellular level. *Nat Rev Mol Cell Biol*, 9:231–241, 2008. 1, 4

[115] T. Telieps et al. Cellular-FLIP, raji isoform (c-FLIP R) modulates cell death induction upon T-cell activation and infection. *Eur. J. Immunol.*, 43(6):1499–14510, 2013. 1, 5, 23, 70

[116] D. J. Topham, R. A. Tripp, and P. C. Doherty. CD8+ T cells clear influenza virus by perforin or Fas-dependent processes. *J. Immunol.*, 159(11):5197–5200, 1997. 73

[117] G.B. Triana-Baltze et al. Inhibition of neuraminidase inhibitor-resistant influenza virus by DAS181, a novel sialidase fusion protein. *PLoS ONE*, 4(11), 2009. 2, 5

[118] S. Tripathi, M. R. White, and K. L. Hartshorn. The amazing innate immune response to influenza a virus infection. *Innate Immun.*, 21:73–98, 2015. 7

[119] R.A. Tripp, S.R. Sarawar, and P.C. Doherty. Characteristics of the influenza virus-specific CD8+ T cell response in mice homozygous for disruption of the H-2lAb gene. *J. Immunol.*, 155(6):2955–2959, 1995. 8

[120] T. M. Tumpey et al. Pathogenicity of influenza viruses with genes from the 1918 pandemic virus: functional roles of alveolar macrophages and neutrophils in limiting virus replication and mortality in mice. *J. Virol.*, 79(23):14933–44., 2005. 5, 7

[121] G. I. Valderrama-Bahamondez and H. Fröhlich. MCMC techniques for parameter estimation of ODE based models in systems biology. *Front. Appl. Math. Stat*, 2019. 36, 69

[122] S.N. Waggoner et al. Natural killer cells act as rheostats modulating antiviral T cells. *Nature*, 481(7381):394–398, 2012. 72, 73, 74

[123] J. Walter et al. Caspase 3 activation is essential for efficient influenza virus propagation. *EMBO J.*, 22(11):2003, 2717-2728. 31, 56, 58

[124] X. Wang et al. Novel pandemic influenza A (H1N1) virus infection modulates apoptotic pathways that impact its replication in A549 cells. *Microbes Infect.*, 16(3):178–86, 2014. 1, 7, 31, 56, 58

[125] C. Wierling et al. *Systems Biology.* Wiley-VCH, 2009. 11, 12

[126] I. A. Wilson and N. J. Cox. Structural basis of immune recognition of influenza virus hemagglutinin. *Annu. Rev. Immunol*, 8:737–771, 1990. 8

[127] W. J. Wurzer et al. Caspase 3 activation is essential for efficient influenza virus propagation. *EMBO J.*, 22:2717–2728, 2003. 1, 5, 7, 31, 58, 70

[128] Y. Zhang et al. In vivo kinetics of human natural killer cells: the effects of ageing and acute and chronic viral infection. *Immunology*, 121(2), 2007. 40

[129] Xiao-Qiang Zhao. *Dynamical systems in population biology.* Springer, 2003. 9

[130] O.P. Zhirnov and H.D. Klenk. Control of apoptosis in influenza virus-infected cells by up-regulation of Akt and p53 signaling. *Apoptosis*, 12(8):1419 – 1432, 2007. 1, 7, 31, 58

[131] G. Zhou et al. NK cells exacerbate the pathology of influenza virus infection in mice. *European Journal of Immunology*, pages 929–938, 2013. 72, 73

[132] K. Zhou et al. Swift and strong NK cell responses protect 129 mice against high-dose influenza virus infection. *J. Immunol*, 196(4):1842–1854, 2016. 72, 73

[133] J. Zimmer, E. Andres, and F. Hentges. NK cell subsets and CD107a mobilization assay. *Leuk. Off. J. Leuk. Soc. Am. Leuk. Res. Fund*, 19:1849–1851, 2005. 26